

EFFECT OF GAS FLOW RATE AND DEPOSITION
PRESSURE TOWARD THE CRYSTALLOGRAPHIC AND
SURFACE MORPHOLOGY OF SEMI-POLAR (11 $\bar{2}$ 2)
GALLIUM NITRIDE GROWN BY MOCVD

OOI CHONG SENG

DEPARTMENT OF PHYSICS
FACULTY OF SCIENCE
UNIVERSITI MALAYA
KUALA LUMPUR

2022

**EFFECT OF GAS FLOW RATE AND
DEPOSITION PRESSURE TOWARD THE
CRYSTALLOGRAPHIC AND SURFACE
MORPHOLOGY OF SEMI-POLAR (11 $\bar{2}$ 2)
GALLIUM NITRIDE GROWN BY MOCVD**

OOI CHONG SENG

**DISSERTATION SUBMITTED IN PARTIAL
FULFILMENT OF THE REQUIREMENTS FOR
THE DEGREE OF MASTER OF SCIENCE**

**DEPARTMENT OF PHYSICS
FACULTY OF SCIENCE
UNIVERSITI MALAYA
KUALA LUMPUR**

2022

UNIVERSITI MALAYA

ORIGINAL LITERARY WORK DECLARATION

Name of Candidate: **OOI CHONG SENG**

Matric No: **17127000/2**

Name of Degree: **MASTER OF SCIENCE**

Title of Dissertation (“this Work”):

EFFECT OF GAS FLOW RATE AND DEPOSITION PRESSURE TOWARD THE CRYSTALLOGRAPHIC AND SURFACE MORPHOLOGY OF SEMI-POLAR (11 $\bar{2}$ 2) GALLIUM NITRIDE GROWN BY MOCVD

Field of Study:

PHYSICS

I do solemnly and sincerely declare that:

- (1) I am the sole author/writer of this Work;
- (2) This Work is original;
- (3) Any use of any work in which copyright exists was done by way of fair dealing and for permitted purposes and any excerpt or extract from, or reference to or reproduction of any copyright work has been disclosed expressly and sufficiently and the title of the Work and its authorship have been acknowledged in this Work;
- (4) I do not have any actual knowledge nor do I ought reasonably to know that the making of this work constitutes an infringement of any copyright work;
- (5) I hereby assign all and every rights in the copyright to this Work to the University of Malaya (“UM”), who henceforth shall be owner of the copyright in this Work and that any reproduction or use in any form or by any means whatsoever is prohibited without the written consent of UM having been first had and obtained;
- (6) I am fully aware that if in the course of making this Work I have infringed any copyright whether intentionally or otherwise, I may be subject to legal action or any other action as may be determined by UM.

Candidate’s Signature

Date: 14/8/2022

Subscribed and solemnly declared before,

Witness’s Signature

Date: 12/9/2022

Name:

Designation:

**EFFECT OF GAS FLOW RATE AND DEPOSITION PRESSURE TOWARD
THE CRYSTALLOGRAPHIC AND SURFACE MORPHOLOGY OF SEMI-
POLAR (11 $\bar{2}2$) GALLIUM NITRIDE GROWN BY MOCVD**

ABSTRACT

V/III ratio and pressure is frequently varied to study the metalorganic chemical vapor deposition (MOCVD) growth parameters effect on semi-polar (11 $\bar{2}2$) gallium nitride epitaxy (GaN) growth on *m*-plane (10 $\bar{1}0$) sapphire substrate. In the first study, V/III ratio is fixed at 118 while varying the Trimethylgallium (TMG) (33.6, 59, 84.3 and 100 sccm) and ammonia (NH₃) (0.4, 0.7, 1.0 and 1.3 SLM) flow rate, respectively. Varying gas flow rate implies different growth rate is induced. Different GaN film with different surface morphologies was produced and their crystal quality was determined. High-resolution X-ray diffraction (HR-XRD) analysis shows that low gas flow enhanced the GaN crystal quality with lowest FWHM values of 576 and 1656 arcsecs at [$\bar{1}\bar{1}23$] and [$1\bar{1}00$], respectively. Field-emission scanning electron microscope (FESEM) also verified that 2D GaN morphology is produced. Whereas high gas flow exhibits low crystal quality together with the distribution of 3D islands on the surface. Atomic force microscopy (AFM) micrographs show different arrowhead elongation length produced at a different flow rate. The presented results suggest that low gas flow rate with low growth rate is necessary to obtain a flat semi-polar (11 $\bar{2}2$) GaN layer. In the second study, the first experiment is repeated by growing on AlN nucleation layer at fixed V/III ratio of 1300 with lower TMA and NH₃ flow rate. There was not much difference in the HR-XRD analysis between the first and second series. The phase and the X-ray rocking curve (XRC) analysis consistently show that the crystal quality improved when TMG and NH₃ gas flow rate is lowered. However, the FESEM results showed that there were less 3D islands formed compared to the first series when GaN grown on aluminum nitride (AlN) nucleation layer with lower gas flow rate. In contrast, the AFM analysis showed quite

similar surface roughness with the first series when compared with each TMG gas flow rate, respectively. The third study involved the variation of reactor pressure (40, 70 and 100 kPa) on GaN epitaxial layer. It has been found out that highest reactor pressure of 100 kPa effectively reduced the dislocations and stacking faults with lowest FWHM value of 416 and 857 arcsecs at $[\bar{1}\bar{1}23]$ and $[1\bar{1}00]$, respectively. However, higher growth pressure resulted in very rough surface morphology and larger surface grain size which led to 3D growth mode. The surface roughening mechanism for both gas flow rate and pressure variation are also explained using the adatom surface diffusion relation $L \sim \sqrt{D\tau}$.

Keywords: GaN, AlN, V/III ratio, Gas flow rate, Pressure

Universiti Malaysia

**KESAN KADAR ALIRAN GAS DAN PEMENDAPAN TEKANAN KEATAS
KRISTALOGRAFI DAN MORFOLOGI PERMUKAAN GALLIUM NITRIDA
SEPARUH KUTUB ($11\bar{2}2$) DITUMBUH DENGAN MENGGUNAKAN MOCVD**

ABSTRAK

Nisbah V/III dan tekanan biasanya diubah untuk mengkaji kesan pertumbuhan parameter dalam pertumbuhan epitaxy gallium nitrida (GaN) separuh kutub pada substrat nilam bersatah-M ($10\bar{1}0$). Dalam kajian pertama, nisbah V/III telah ditetapkan pada nilai 118 sementara kadar aliran trimethylgallium (TMG) (33.6, 59, 84.3 and 100 sccm) dan ammonia (NH_3) (0.4, 0.7, 1.0 and 1.3 SLM) diubahkan. Kadar aliran gas yang berbeza menyebabkan kadar pertumbuhan yang berbeza. Filem GaN yang berbeza dengan morfologi permukaan yang berbeza dihasilkan dan kualiti hablurnya telah ditentukan. Analisis belauan sinar-x resolusi tinggi (HR-XRD) menunjukkan bahawa kadar aliran gas terendah meningkatkan kualiti hablur epitaksi GaN dengan nilai FWHM terendah 576 dan 1656 arka saat masing-masing pada satah $[\bar{1}\bar{1}23]$ dan $[1\bar{1}00]$. Permukaan 2D terhasil juga diimbas oleh mikroskop elektron pengimbas lepasan lapangan (FESEM). Manakala kadar aliran gas yang tinggi menunjukkan kualiti hablur yang rendah bersamaan dengan pengagihan pulau-pulau 3D di permukaannya. Mikrograf daya atom (AFM) menunjukkan pemanjangan anak panah yang berbeza yang dihasilkan pada kadar aliran yang berbeza. Hasil ini mencadangkan bahawa kadar aliran gas rendah dengan kadar pertumbuhan rendah diperlukan untuk menghasilkan lapisan GaN separuh kutub ($11\bar{2}2$) yang rata. Dalam kajian kedua, eksperimen pertama diulangi dengan pertumbuhan pada lapisan nukleasi aluminium nitrida (AlN) pada nisbah V/III yang tetap bernilai 1300 dengan kadar aliran trimethylaluminium (TMA) dan NH_3 yang lebih rendah. Analisis HR-XRD antara siri pertama dan kedua tidak menunjukkan perbezaan yang ketara. Analisis fasa dan keluk goyang sinar-X (XRC) secara konsistennya menunjukkan bahawa kualiti hablur bertambah baik apabila kadar aliran gas TMG dan NH_3 diturunkan. Walau

bagaimanapun, hasil FESEM menunjukkan bahawa tidak banyak pulau 3D terhasil bila dibandingkan dengan siri pertama ketika GaN menumbuh di lapisan nukleasi AlN dengan kadar aliran gas yang lebih rendah. Sebaliknya, analisis AFM menunjukkan kekasaran permukaan yang hampir sama dengan siri pertama jika dibandingkan dengan kadar aliran gas TMG masing-masing. Kajian ketiga melibatkan perubahan tekanan reaktor (30, 70 dan 100 kPa) pada lapisan epitaksial GaN. Telah didapati bahawa pertumbuhan di tekanan yang tertinggi berkesan dalam mengurangkan kehelan dan kesalahan susun dengan nilai FWHM terendah 416 dan 857 arka saat masing-masing pada $[\bar{1}\bar{1}23]$ dan $[1\bar{1}00]$. Walau bagaimanapun, pertumbuhan di tekanan yang lebih tinggi menghasilkan morfologi permukaan yang sangat kasar dan ukuran butiran permukaan yang lebih besar dan menyebabkan pertumbuhan mod 3D. Mekanisme permukaan menjadi kasar untuk kedua-dua variasi kadar aliran gas dan tekanan juga dijelaskan menggunakan hubungan resapan permukaan adatom $L \sim \sqrt{D\tau}$.

Kata kunci: GaN, Nisbah V/III, Kadar aliran gas, Tekanan, AlN

ACKNOWLEDGEMENTS

First of all, I would like to express my gratitude to both of my supervisors, Associate Professor Dr. Ahmad Shuhaimi Abu Bakar and Professor Dr. Wan Haliza Abd Majid for the golden opportunity given to let me carry out my research and guidance provided during the whole master program.

Next, I would like to thank all my lab members, Gary Tan, Hilmi, Hakim, Afiq, Haaziq, Omar, Nazry, Adreen, Anas, Rakif, Isma, Diyana, Dr. Azrina, Najwa, Najiha and Liyana for their precious help, supports and encouragement during good and bad times. Thanks for all the lessons taught and make me a more knowledgeable person.

Additionally, thanks to Crest and Universiti Malaya for all the grants provided and making sure all the research go well.

Last but not least, thanks to those who have directly or indirectly lend me a helping hand during my whole master program.

TABLE OF CONTENTS

ORIGINAL LITERARY WORK DECLARATION.....	ii
ABSTRACT.....	iii
ABSTRAK.....	v
ACKNOWLEDGEMENTS.....	7
TABLE OF CONTENTS.....	8
LIST OF FIGURES.....	11
LIST OF TABLES.....	16
LIST OF SYMBOLS AND ABBREVIATIONS.....	17
CHAPTER 1: INTRODUCTION.....	20
1.1 Introduction.....	20
1.2 Research Problem.....	20
1.3 Research Motivation.....	20
1.4 Research Objective and Research Scope.....	21
1.5 Thesis Summary.....	22
CHAPTER 2: LITERATURE REVIEW.....	23
2.1 Gallium Nitride.....	23
2.2 GaN Growth	26
2.2.1 Reaction Kinetics of Metalorganic Compound.....	26
2.2.2 Growth mode and atomistic processes.....	31
2.3 Polarity of GaN.....	34
2.4 Defects in Semi-polar GaN.....	41
2.4.1 Origin of defects.....	41
2.4.2 Defects in semi-polar (11 $\bar{2}$ 2) GaN.....	43
2.5 Arrowhead	48
2.6 Growth of GaN on AlN and GaN nucleation layer.....	50
2.6 Summary.....	51
CHAPTER 3: METHODOLOGY.....	52
3.1 Introduction.....	52

3.2	Experiment Methods.....	52
3.3	Metalorganic Chemical Vapor Deposition (MOCVD).....	53
3.4	Equipment for characterization.....	55
3.4.1	Atomic Force Microscopy (AFM).....	55
3.4.2	Field Emission Scanning Electron Microscope (FESEM).....	57
3.4.3	High Resolution X-ray Diffraction (HR-XRD).....	58
3.5	Summary.....	62
3.6	Overview of research flow.....	63

CHAPTER 4: THE EFFECT OF GAS FLOW RATE ON SEMI-POLAR (11 $\bar{2}$ 2) GAN EPITAXIAL LAYER.....64

4.1	Variation of TMG gas flow on AlN growth with TMA flow of 98.5 sccm at fixed V/III.....	65
4.1.1	Phase Analysis.....	65
4.1.2	On- and Off-axis XRC.....	66
4.1.3	Reciprocal Space Maps (RSM).....	68
4.1.4	Field Effect Scanning Electron Microscopy (FESEM).....	69
4.1.5	Atomic force microscope (AFM).....	72
4.2	Variation of TMG gas flow on AlN growth with TMA flow of 50 sccm at fixed V/III.....	74
4.2.1	Phase Analysis.....	74
4.2.2	On- and Off-axis XRC.....	75
4.2.3	Reciprocal Space Maps (RSM).....	77
4.2.4	FESEM.....	78
4.2.5	Atomic force microscope (AFM).....	80
4.3	Discussion.....	82
4.4	Summary.....	88

CHAPTER 5: THE EFFECT OF PRESSURE ON SEMI-POLAR (11 $\bar{2}$ 2) GAN EPITAXIAL LAYER.....89

5.1	Phase Analysis.....	90
5.2	On- and Off-axis XRC.....	91
5.3	Reciprocal Space Maps (RSM).....	93
5.4	Atomic force microscope (AFM).....	94
5.5	Summary.....	95

CHAPTER 6: CONCLUSION.....	96
REFERENCES.....	98
LIST OF PUBLICATIONS AND PAPERS PRESENTED.....	108

Universiti Malaya

LIST OF FIGURES

Figure 2.1	: Schematic diagram for two different GaN phases. The green and red ball represents gallium and nitrogen atom respectively..	24
Figure 2.2	: Energy bandgap of III-V group as a function of lattice parameter.....	25
Figure 2.3	: (a) Decomposition rate of TMG in He/toluene mixture, toluene, He, N ₂ , D ₂ , and H ₂ . (b) Decomposed product of TMG in H ₂	28
Figure 2.4	: Phase diagram of GaN and InN for various mole fraction of decomposed ammonia, α with V/III ratio versus vapor pressure of initial metal-organic precursor.....	30
Figure 2.5	: Schematic diagram for (a) FM growth mode, (b) SK growth mode and (c) VW growth mode.....	32
Figure 2.6	: Schematic diagram of TSK model for atomistic process occurred in epitaxial growth.....	33
Figure 2.7	: Schematic illustration of two mobility concept	34
Figure 2.8	: Schematic energy band diagram of QW under influence of QCSE.....	35
Figure 2.9	: Internal quantum efficiency (IQE) and current droop as a function of current density for polar GaN/InGaN LED.....	36
Figure 2.10	: Schematic of various commonly grown semi- and non-polar GaN.....	38
Figure 2.11	: InGaN polarization with various indium composition as a function of angle between surface normal and <i>c</i> -axis.....	39
Figure 2.12	: Schematic of crystal structure on the surface of (a) Polar, (b) Semi-polar (11 $\bar{2}$ 2) and (c) Non-polar GaN.....	40

Figure 2.13	: Schematic of cross-sectional plane for [0001] AlN grown on [0001] sapphire substrate.....	42
Figure 2.14	: Heteroepitaxial layer with (a) strain and (b) misfit dislocation...	43
Figure 2.15	: Image of edge dislocation.....	44
Figure 2.16	: Illustration of Frank-Shockley partial dislocation by removal of a plane.....	45
Figure 2.17	: Illustration of Shockley partial dislocation by a slip of vector....	46
Figure 2.18	: Illustration of stacking sequence for (a)BSF I ₁ and (b)BSF I ₂	47
Figure 2.19	: Atomic models of PSF in wurtzite GaN. Black and white circles both representing Gallium atoms.....	48
Figure 2.20	: Special surface feature of non- and semi-polar GaN appear in literature as (a) arrowhead, (b) chevron and (c) hillock.....	49
Figure 3.1	: GaN with AlN nucleation layer grown on the <i>m</i> -plane sapphire substrate.....	53
Figure 3.2	: Schematic diagram of MOCVD reactor.....	54
Figure 3.3	: Susceptor, wafer holder and 2” wafer used in this experiment...	54
Figure 3.4	: Taiyo Nippon Sanso SR-2000.....	54
Figure 3.5	: Schematic diagram for working principle of AFM.....	56
Figure 3.6	: Park System NX-10 AFM.....	56
Figure 3.7	: FESEM Hitachi SU8220.....	58
Figure 3.8	: Constructive and destructive interference occurs during interaction of x-ray and atoms.....	59
Figure 3.9	: Schematic diagram of Bragg diffraction.....	60
Figure 3.10	: Rigaku high-resolution x-ray diffraction (HR-XRD).....	60
Figure 3.11	: Schematic diagram of HRXRD stage mobility.....	61

Figure 4.1	: Schematic diagram of experiment series (a)first and (b)second where the gas variation is kept at fixed V/III ratio.....	64
Figure 4.2	: HR-XRD 2θ - ω scans of GaN grown on <i>m</i> -plane sapphire with AlN nucleation layer growth with TMA flow of 98.5 sccm from a higher flow rate (S1) to the lowest flow rate (S4).....	65
Figure 4.3	: (a) On-axis XRC FWHM of GaN ω -scan as a function of azimuthal angle for sample S1, S2, S3 and S4. The off-axis XRC FWHM of sample S1, S2, S3 and S4, (b) $(10\bar{1}1)$ and $(11\bar{2}0)$ diffraction planes, (c) $(n0\bar{n}0)$ and (d) $(000n)$ diffraction planes.....	66
Figure 4.4	: X-ray reciprocal space maps (RSM) of semi-polar $(11\bar{2}2)$ GaN on <i>m</i> -plane sapphire along $[\bar{1}\bar{1}23]$ for (a) S1, (b) S2, (c) S3 and (d) S4.....	69
Figure 4.5	: FESEM images of (a) S1, (b) S2, (c) S3 and (d) S4.....	70
Figure 4.6	: Cross-section fesem images of sample (a)S1 and (b) S4.....	71
Figure 4.7	: $(5 \times 5) \mu\text{m}$ AFM and FESEM micrograph of the flat surface area of (a) S2, (b) S3 and (c) S4.....	72
Figure 4.8	: HR-XRD 2θ - ω scans of GaN grown on <i>m</i> -plane sapphire with AlN nucleation layer growth with TMA flow of 50 sccm from a higher flow rate (SA1) to the lowest flow rate (SA4).....	74
Figure 4.9	: (a) On-axis XRC FWHM of GaN ω -scan as a function of azimuthal angle for sample SA1, SA2, SA3 and SA4. The off-axis XRC FWHM of sample SA1, SA2, SA3 and SA4, (b) $(10\bar{1}1)$ and $(11\bar{2}0)$ diffraction planes, (c) $(n0\bar{n}0)$ and (d) $(000n)$ diffraction planes.....	75

Figure 4.10	: X-ray reciprocal space maps (RSM) of semi-polar (11 $\bar{2}$ 2) GaN on <i>m</i> -plane sapphire along [$\bar{1}\bar{1}$ 23] for (a) SA1, (b) SA2, (c) SA3 and (d) SA4.....	77
Figure 4.11	: FESEM images of (a) SA1, (b) SA2, (c) SA3 and (d) SA4.....	79
Figure 4.12	: Cross-section FESEM images of sample (a)SA1 and (b) SA4...	80
Figure 4.13	: (5 x 5) μm AFM and FESEM micrograph of the flat surface area of (a) SA1, (b) SA2, (c) SA3 and (d) SA4.....	81
Figure 4.14	: (a) On-axis XRC FWHM of GaN ω -scan as a function of azimuthal angle for all samples. The off-axis XRC FWHM of all samples, (b) (10 $\bar{1}$ 1) and (11 $\bar{2}$ 0) diffraction planes, (c) ($n0\bar{n}$ 0) and (d) (000 n) diffraction planes.....	82
Figure 4.15	: FESEM images of (11 $\bar{2}$ 2) semi-polar GaN islands growth at TMG flow of 100 sccm for (a) S1 and (b) SA1.....	83
Figure 4.16	: FESEM image of 3D islands on the sample (a) S1, (b) S2 and (c) S3.....	85
Figure 4.17	: Illustration of semi-polar GaN surface coalescence towards the formation of an arrowhead.....	86
Figure 5.1	: Schematic diagram for this experiment.....	89
Figure 5.2	: HR-XRD 2θ - ω scans of GaN grown on <i>m</i> -plane sapphire with AlN nucleation layer growth with pressure from 13.3 kPa (P1) to 100 kPa (P4).....	90
Figure 5.3	: (a) On-axis XRC FWHM of GaN ω -scan as a function of azimuthal angle for sample P1, P2, P3 and P4. The off-axis XRC FWHM of sample P1, P2, P3 and P4, (b) (10 $\bar{1}$ 1) and	

	(11 $\bar{2}$ 0) diffraction planes, (c) ($n0\bar{n}0$) and (d) (000 n) diffraction planes.....	91
Figure 5.4	: Growth mechanism proposed by Wu et al.....	92
Figure 5.5	: X-ray reciprocal space maps (RSM) of semi-polar (11 $\bar{2}$ 2) GaN on m -plane sapphire along [$\bar{1}\bar{1}23$] for (a) P1, (b) P2, (c) P3 and (d) P4	93
Figure 5.6	: 25 x 25 μm AFM images of the flat surface area of (a) P1, (b) P2, (c) P3 and (d) P4.....	94

Universiti Malaysia

LIST OF TABLES

Table 3.1	: FWHM broadening factor for each off-axis plane.....	62
Table 4.1	: Growth parameters variation adapted in this work.....	64
Table 4.2	: Diffuse scattering (DS) streaks and tilt value of sample S1 to S4 based on x-ray RSM.....	68
Table 4.3	: Diffuse scattering (DS) streaks and tilt value of sample SA1 to SA4 based on x-ray RSM.....	78
Table 4.4	: Growth rate for experimental series 1 and 2.....	86
Table 4.5	: Flat surface roughness (RMS value) for experimental series 1 and 2.....	87
Table 5.1	: Pressure adapted in this experiment.....	89
Table 5.2	: Diffuse scattering (DS) streaks and tilt value of sample SA1 to SA4 based on x-ray RSM.....	94

LIST OF SYMBOLS AND ABBREVIATIONS

a	:	Activities / crystal lattice
E_m	:	Adatom migration activation energy
θ	:	Angle
φ / ϕ	:	Azimuthal angle
b	:	Burgers vector
D	:	Diffusion rate
K	:	Equilibrium constants
ω	:	Incident angle
f	:	Lattice mismatch
P_{xx}	:	Partial pressure of xx gaseous molecule
P_{sp}	:	Spontaneous polarization
E_s	:	Step edge barrier
P_{pz}	:	Strain affected piezoelectric polarization
γ	:	Surface free energy
d_{nn}	:	Surface nearest neighbor distance
T	:	Temperature
E_D	:	Terrace diffusion barrier
χ	:	Tilt angle
ΔP_{tot}	:	Total polarization difference
ν_o	:	Vibrational frequency of adatom in initial state
λ	:	Wavelength / adatoms mobility
R	:	Alkyl group
Al	:	Aluminum
NH ₃	:	Ammonia

As	:	Arsenide
AFM	:	Atomic force microscopy
BSF	:	Basal stacking faults
D ₂	:	Deuterium
FESEM	:	Field-emission scanning electron microscope
FM	:	Frank-van deer Merwe
Ga	:	Gallium
He	:	Helium
HEMT	:	High electron mobility transistor
HR-XRD	:	High-resolution x-ray diffraction
HVPE	:	Hydride vapor-phase epitaxy
CH	:	Hydrocarbon
H ₂	:	Hydrogen
In	:	Indium
LED	:	Light emitting diode
MOVPE	:	Metal-organic vapor-phase epitaxy
N	:	Nitride
PD	:	Partial dislocations
PSF	:	Prismatic stacking faults
QCSE	:	Quantum Confinement Stark Effect
QW	:	Quantum well
RMS	:	Root mean square
SF	:	Stacking faults
SK	:	Stranski-Karastanov
TSK	:	Terrace Step Kink
TD	:	Threading dislocations

TMA	:	Trimethylaluminum
TMG	:	Trimethylgallium
TMI	:	Trimethylindium
VW	:	Volmer-Weber
XRC	:	X-ray rocking curve
ZB	:	Zinc blende

Universiti Malaya

CHAPTER 1: INTRODUCTION

1.1 Introduction

III-nitride based optoelectronic devices have been of great interest as an alternative to conventional light bulbs due to their high emission efficiency and wide band gap ranging from 0.67 to 3.4 eV, which covers the full visible spectrum (Akasaki & Amano, 1997; Nakamura et al., 2000; Zhang et al., 2019). The most popularly used material for LED is gallium nitride (GaN) which typically grows on *c*-plane (Nakamura et al., 1994, 1996).

1.2 Research Problem

However, LED grown on *c*-plane suffers a large quantum-confined stark effect (QCSE) due to the existence of piezoelectric and spontaneous polarization in the quantum well region (Zhu et al., 2017). This phenomenon cause the separation of the electron-hole wave functions and increase the recombination time thus reduce the efficiency of the device (Kioupakis et al., 2011; Ling et al., 2010; Zhu et al., 2017). Moreover, the impact become larger in longer wavelength LED as higher indium incorporation induce more lattice mismatch in the multi quantum wells (Song et al., 2012).

1.3 Research Motivation

In order to overcome this problem, GaN based LED is grown on non- and semi-polar crystal orientation (Speck & Chichibu, 2009). Devices grown along these orientations have been proved to have higher internal and external quantum efficiency (Waltereit et al., 2000). For longer wavelength devices, semi-polar orientation is preferred as non-polar has less indium incorporation efficiency (Sato et al., 2008; Wernicke et al., 2012). On the flip side, semi-polar (11 $\bar{2}$ 2) GaN for example, suffers from high defect density in which 98% is contributed by partial dislocations and basal stacking faults, and 2% caused by *a*-type perfect dislocations (Dasilva et al., 2010; Ruterana et al., 2010). Numerous efforts such as epitaxial lateral overgrowth (ELOG) (Zhu et al., 2010), AlN/GaN multilayer,

silicon nitride (SiN_x) interlayer (Xing et al., 2019), double AlN or GaN nucleation layers (Zhao et al., 2016), patterned sapphire substrates (Tendille et al., 2014) and graded superlattices (Xu et al., 2012) have been explored to solve this problem to enhance crystal quality and surface morphology. Growth parameters such as temperature (Wang et al., 2018), V/III ratio (Grinys et al., 2017; Omar et al., 2018) and reactor pressure (Liu et al., 2015; Sun et al., 2009) have been widely discussed to understand their influence on the growth process. To achieve good GaN layer, researchers will normally combine the growth parameters utilizing two-step process to achieve 3D layers first using lower V/III ratio and temperature and then higher V/III ratio and temperature for surface smoothing

1.4 Research Objectives and Research Scope

There is no research yet reported on growth parameter for the effect of gas flow rate at fixed V/III ratio on semi-polar GaN growth. Thus, it will be very interesting to study the effect of this parameter on the GaN growth process. In this study, the effect of gas flow rate at fixed V/III ratio on both TMG and TMA sources on crystallinity and surface of semi-polar ($11\bar{2}2$) GaN growth is presented. The V/III ratio value chosen for GaN growth are 118 while for AlN growth are 1300 as optimized by my senior Omar (Omar, 2019). Furthermore, the study of pressure as one step growth process for semi-polar ($11\bar{2}2$) GaN on *m*-plane sapphire substrate is also presented.

The objectives of this work are:

- 1) To optimize the TMG and ammonia flow rate at fixed V/III ratio of 118 on semi-polar ($11\bar{2}2$) GaN on *m*-plane sapphire substrate.
- 2) To investigate the effect of AlN nucleation layer grown at two different flow rates but kept at fixed V/III ratio of 1300 toward ($11\bar{2}2$) GaN epitaxial layer
- 3) To determine the effect of pressure on semi-polar ($11\bar{2}2$) GaN on *m*-plane sapphire substrate.

1.5 Thesis Layout

This dissertation is organized into 6 chapters. Chapter 1 is the introduction where importance and challenges in semi-polar GaN is briefly discuss and the aim of this study is outlined. Chapter 2 is the literature review where detailed information regarding Gallium Nitride, GaN growth, polarity of GaN, defects, and arrowhead is included. Chapter 3 is the Methodology where experimental procedure and equipment used are discussed. Chapter 4 reports the results and discussions for gas flow rate variation series and Chapter 5 reports the results and discussion for pressure variation series. Finally, the last chapter concludes the outcome of this work and future work that can be done.

Universiti Malaysia

CHAPTER 2: LITERATURE REVIEW

2.1 Gallium Nitride

Gallium nitride has been a hot topic since the late 1990s due to its distinct properties which can be applied in optoelectronics, high power and high frequency devices. However, GaN epitaxial growth has a longer history than was perceived (only 10 years later than Gallium Arsenide GaAs) even though its development in epitaxial growth and device structure only came about 30 years later. Development of GaN can be divided into several phases including early development of GaN powder, GaN thin film and device based GaN.

The synthesis of GaN can be traced back to 1930s where Johnson et al.(Johnson et al., 1932) presented the formation of GaN material by flowing ammonia over liquid gallium at 800°C in hydrogen ambient following the route:



Later, the first GaN film was successfully prepared by Pasternak et al.(Pastrňák & Součková, 1963) via gas discharge on quartz plate. In 1969-1971, Maruska et al.(Maruska & Tietjen, 1969) produced thin GaN layer on sapphire substrates using hydride vapor-phase epitaxy (HVPE) and this has first confirmed its wide bandgap properties of 3.39eV. The following year, Manasevit et al.(Manasevit, 1972; Manasevit et al., 1971). demonstrated the first GaN epitaxial layer grown by metal-organic vapor-phase epitaxy (MOVPE). This method has become the most popular method nowadays in nitride growth. However, the layers are still rough and not transparent due to large lattice mismatch. The breakthrough from Amano et al.(Amano et al., 1986) in 1986 produced GaN with good crystallographic by introducing a low temperature AlN nucleation layer. In 1991-1992, Shuji Nakamura(Nakamura et al., 1991, 1992) optimized the growth conditions of GaN on sapphire and this technology has been widely used by most laboratories and companies

for fabricating LED and other devices. In 1992, Nichia started offer blue GaN LED and at presents, such LED are widely used. In 1993, Asif Khan et al.(Khan et al., 1991) produced the first AlGaN/GaN heterojunction using MOVPE and this was regarded as the start of nitride high electron mobility transistor (HEMT) technology. These works concluded the early significant development of GaN film. At present, the research on GaN is carried out worldwide and many applications are produced using GaN.

Gallium Nitride has a molar mass of 83.730 g/mol and density of 6.1 g/cm³. It is considered hard (around 12GPa) and has a melting point of over 1600°C. It is also insoluble in water. It can exist in 2 structure: zinc blende and wurtzite. However, zinc blende phase is undesirable due to its thermodynamics metastability. Normally, GaN exists in wurtzite phase as shown in Figure 2.1.

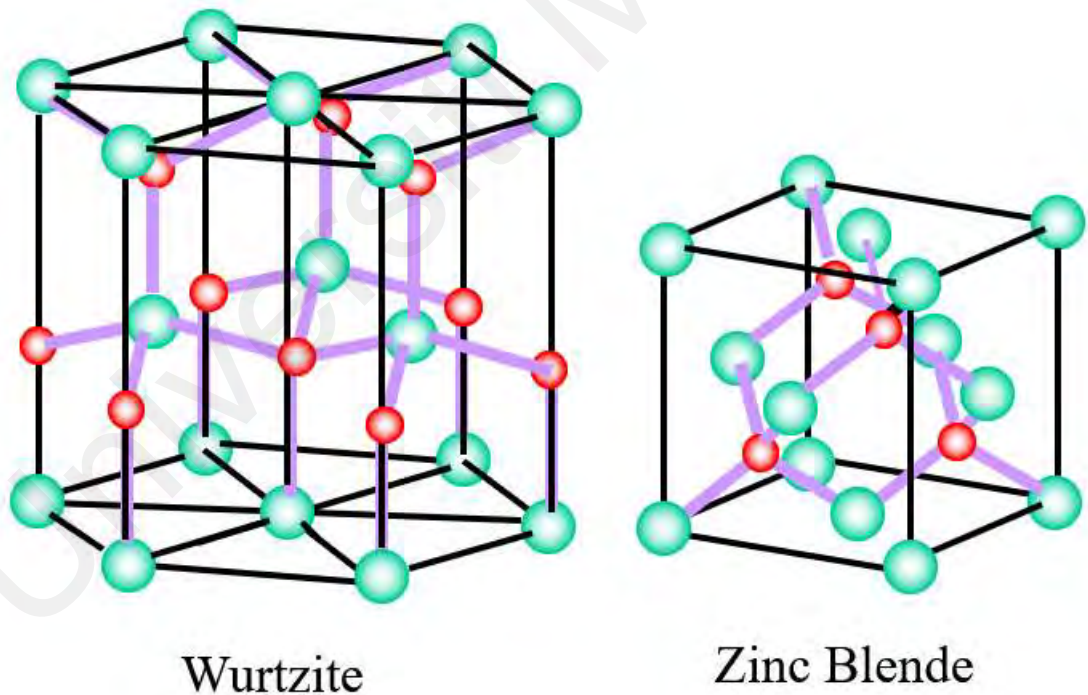


Figure 2.1: Schematic diagram for two different GaN phases. The green and red ball represents gallium and nitrogen atom, respectively.

GaN has a thermal conductivity of 1.3W/(cm.K) at room temperature, smaller than silicon but its electron mobility reaches 2000 cm²/Vs, 30% higher than silicon(Mion,

2006; Strydom et al., 2015). When compare GaN FET to normal MOSFET, GaN has a 40% power loss reduction and running at 10°C cooler which implies GaN devices can withstand higher voltage and temperature. The most important characteristics GaN has is its wide energy bandgap. GaN has a bandgap of 3.4 eV and considering the elements in III-N group, Aluminum (Al) and Indium (In) provide a tunability large bandgap of 6 eV to 0.65 eV. For the application of LED, its bandgap covers the whole visibility spectrum. Figure 2.2 shows the energy bandgap of III-V group as a function of lattice parameter.

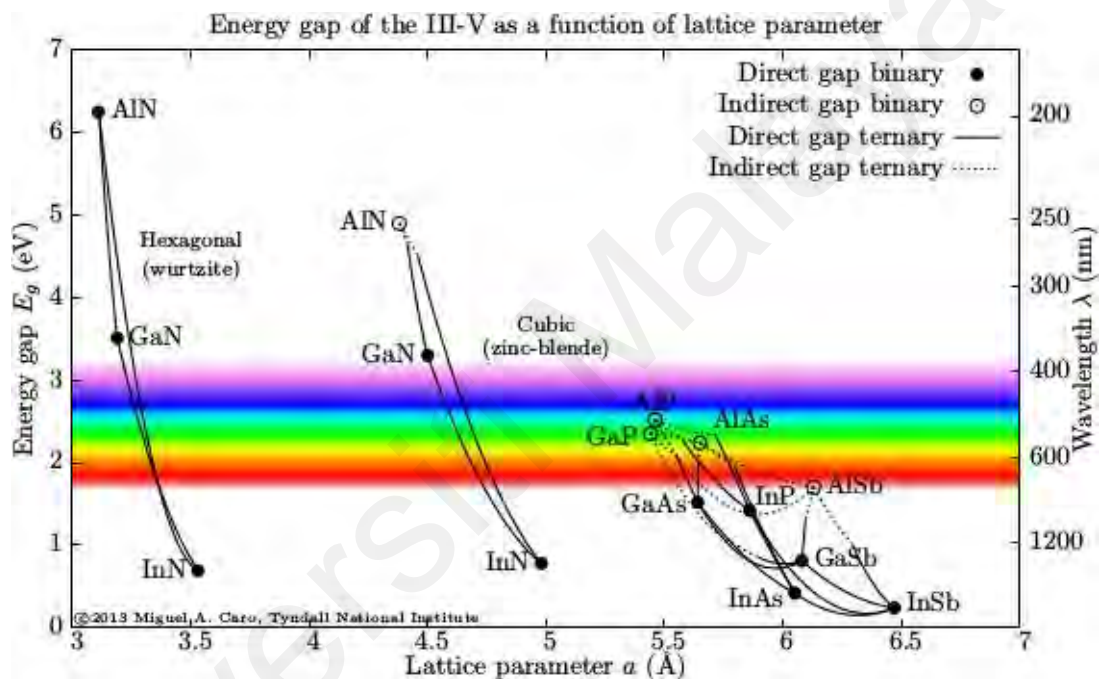


Figure 2.2: Energy bandgap of III-V group as a function of lattice parameter (Vurgaftman et al., 2001; Vurgaftman & Meyer, 2003), obtained from Journal of Applied Physics.

It can be observed that bandgap of GaN is much wider than other elements in the same III-V group. Although the study of GaAs is more matured, it still has difficulties on going towards blue region compared to GaN. Nowadays, most of the blue region LED is manufactured using GaN materials. However, GaN LED suffered from problems such as QCSE, high dislocation density and low indium incorporation (for longer wavelength emission). Hence, semi- and non- polar oriented GaN is introduced and all these will be discussed in the next few sections.

2.2 GaN Growth

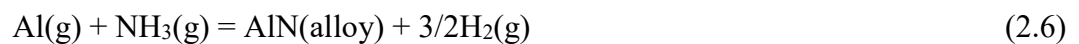
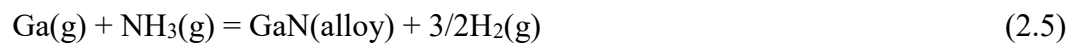
2.2.1 Reaction Kinetics of Metalorganic Compound

The GaN growth can be understood via thermodynamics model developed by Koukitu et al. (Koukitu et al., 1996) in 1996. Although the model was intended to understand the growth of InGaN as it is the top priority in 1990s, his model can also give an insight to group III-based nitride growth by MOCVD. It is well known that the growth normally occurred at mass transport region, which means the rate is controlled by the rate of arrival of the metal-organic adatoms at vapor-solid interface. It can also be assumed that the chemical reaction for nitride alloys formation is higher compared to the rate of arrival and the formation depends on the Gibbs free energy of the surface and reactant which are affected by the constituent compounds and the V/III ratio. At vapor-solid interface, the following reactions occurred:



R=Alkyl group, for example CH₃- or C₂H₅-, H₂=hydrogen gas, Ga=Gallium, Al=Aluminum, In=Indium

The decomposition of metal-organic sources is irreversible according to the homogeneous reaction above. At the substrate surface, the reactions involved are:



Where GaN, AlN and InN are the constituent compounds in the alloy. The equilibrium constants are:

$$K_1 = \frac{a_{GaN} \cdot P_{H_2}^{3/2}}{P_{Ga} \cdot P_{NH_3}} \quad (2.8)$$

$$K_2 = \frac{a_{AlN} \cdot P_{H_2}^{3/2}}{P_{Al} \cdot P_{NH_3}} \quad (2.9)$$

$$K_3 = \frac{a_{InN} \cdot P_{H_2}^{3/2}}{P_{In} \cdot P_{NH_3}} \quad (2.10)$$

Where a_{GaN} , a_{AlN} and a_{InN} are the activities of the constituent alloy compounds which can be obtained using delta lattice parameter (DLP) model (Stringfellow, 1974) and P_{xx} are the partial pressure of xx gaseous molecule. The total pressure of the system is:

$$\sum P_i = P_{Ga} + P_{Al} + P_{In} + P_{NH_3} + P_{H_2} + P_{RH} + P_{IG} \quad (2.11)$$

Where IG is inert gas. However, the equilibrium constants are in the order of $K_3 \ll K_1 < K_2$ which means that the formation of InN are very unstable and easily affected by the presence of H_2 which will reverse the Equation (2.6) from right side to the left side and this lead to the discussion on carrier gas used in MOCVD during growth.

The earliest pyrolysis of TMG was studied by Jacko (Jacko & Price, 1963). It was found that the $(CH_3)_3Ga$ decompose through homolytic cleavage of methyl at elevated temperature:



At certain concentration, the monomethyl gallium will polymerize, and methyl radicals will form ethane. The decomposition mechanism of TMG with different gas carrier were further studied by Larsen et al. (Larsen et al., 1990) in 1989. Figure 2.3 shows (a) the decomposition rate of TMG in He/toluene mixture, toluene, helium, nitrogen, deuterium and hydrogen and (b) decomposed products of TMG in H₂.

From Figure 2.3(a), it can be concluded that H₂ helps in the decomposition of TMG while (b) showed that H₂ plays an important role in scavenging the methyl radicals in the

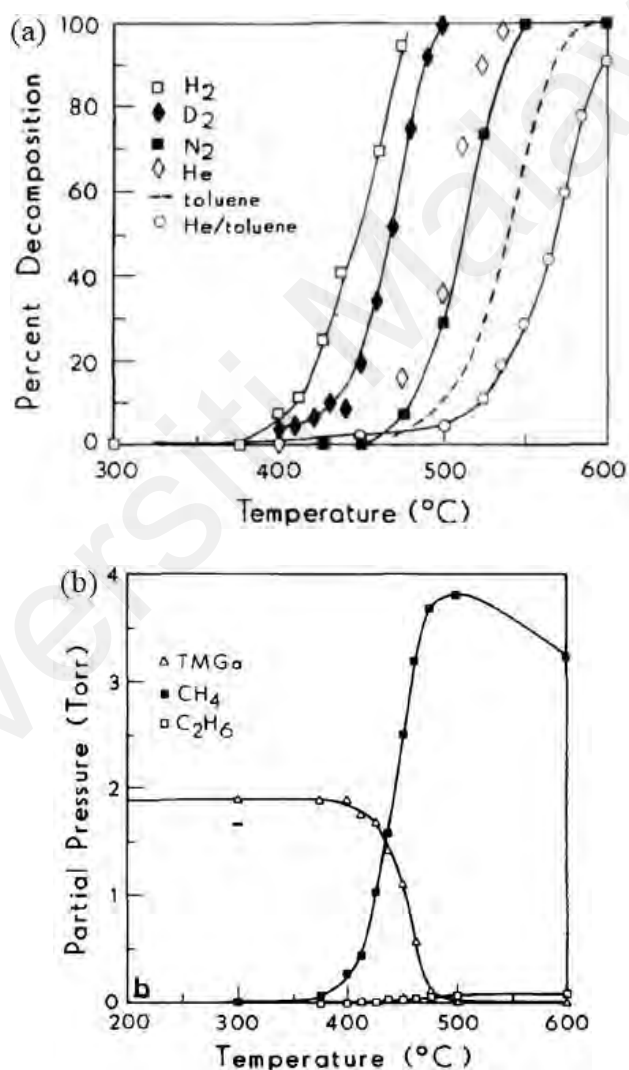


Figure 2.3: (a) decomposition rate of TMG in He/toluene mixture, toluene, He, N₂, D₂, and H₂. (b) Decomposed product of TMG in H₂. (Larsen et al., 1990), obtained from Journal of Crystal Growth.

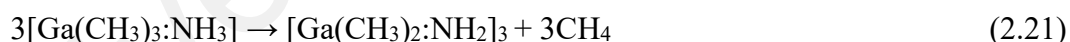
decomposition process. Methane formed instantaneously as TMG decomposes while minimum methyl radicals are forming ethane. The reaction is described by:



It is also found that H₂ helps in reducing the parasitic reaction between TMG and NH₃ in vapor(Thon & Kuech, 1996). Because TMG and NH₃ are III-V Lewis acid-Lewis base combinations, they can form intermediate compounds at low temperature. The electron acceptor TMG (Lewis acid) and electron donor NH₃ (Lewis base) can form trimethylgalliummonamine (TMG:NH₃) and the reaction is described as:



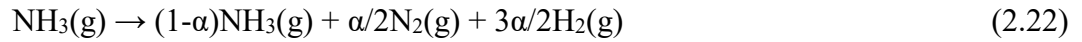
The compound then released one methane per Ga atom to form a six members ring, Cyclo(trimimidohexamethyltrigallium)(Almond et al., 1992):



This adduct compound is said to have impact on the growth rate and uniformity as more energy are needed to decompose it. With the presence of H₂, elimination of methane from TMG can even take place in the absence of NH₃(Nakamura et al., 2000) by forming Ga(CH₃)₂H. Hence in MOCVD system, TMG was supplied with hydrogen as carrier gas to ensure pyrolysis of TMG and prevent formation of adduct compound.

The decomposition of TMA follows similar mechanism as TMG through homolytic cleavage with methyl radicals. However, for the case of TMI, hydrogen cannot be used as gas carrier. TMI has lower decomposition temperature than Ga and Al compounds due

to weaker In-C bond. At temperature more than 300°C, ammonia decomposed thermodynamically into nitrogen and hydrogen. However, only a fraction of it decomposed and α is denoted as the mole fraction of decomposed ammonia. The equation is given by:



From equation (2.21), every decomposition of α ammonia will produce $3\alpha/2\text{H}_2$ and only $\alpha/2\text{N}_2$. Since the decomposition of ammonia will produce more hydrogen and it is unwanted as it will shift the right side of equation (2.6) to left side, flowing hydrogen during InN growth will cause etching. To slow down the decomposition of ammonia and reduce etching, nitrogen flow is preferred and the growth temperature of InN is lower compared to AlN and GaN to slow down the breakdown process of ammonia.

Koukitu et al.(Koukitu et al., 1997) presented a thermodynamics study on epitaxial growth of group III nitrides in 1997 and his results is shown in Figure 2.4. From

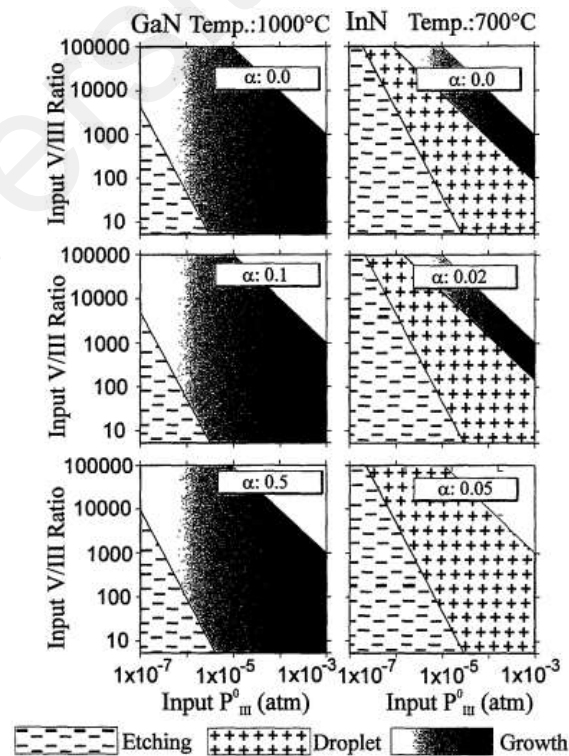


Figure 2.4: Phase diagram of GaN and InN for various mole fraction of decomposed ammonia, α with V/III ratio versus vapor pressure of initial metal-organic precursor (Koukitu et al., 1997), obtained from Japanese Journal of Applied Physics.

Figure 2.4, etching means the depletion of epitaxy layer, droplet means formation of precursor metal and growth means formation of epitaxy layer. It can be observed that InN growth is hugely affected by the decomposition of ammonia whereas GaN is not affected. Hence, parameter for InN growth should be selected cautiously compared to GaN and AlN.

2.2.2 Growth mode and atomistic processes

Besides reaction equation aspect, the GaN epitaxy growth can also be understood from the thermodynamic and kinetic aspects. Epitaxy is a type of growth where a new crystalline layer is deposited on crystalline substrate. The deposited crystalline film is referred to epitaxial film or epitaxial layer. Epitaxial layer can be deposited from gaseous or liquid precursors. The deposited film will take the characteristics of the substrate in term of lattice structure and orientation up to a certain critical thickness, after which it revert to its own characteristics and thus results in dislocation. Epitaxy can be divided into two categories:

- a) Homoepitaxy: which the crystalline layers are grown on the substrate of similar composition.
- b) Heteroepitaxy: which the crystalline layers are grown on the substrate of different composition.

From thermodynamic aspect, growth mode involves in the initial stages of GaN epitaxy growth which is affected by surface free energy and wetting properties of the components involved. There were three growth modes that are most frequently observed in epitaxy growth and each of the growth mode involves the surface free energy of substrate, $\gamma_{\text{substrate}}$, film, γ_{film} and between film and substrate, $\gamma_{\text{interface}}$. They are:

- a) Frank-van der Merwe mode (FM): layer by layer growth (2D)

$$\gamma_{\text{substrate}} \geq \gamma_{\text{film}} + \gamma_{\text{interface}}$$

This is the case where the epitaxial layer is wetter than the substrate.

b) Volmer-Weber Mode (VW): island growth (3D)

$$\gamma_{\text{substrate}} < \gamma_{\text{film}} + \gamma_{\text{interface}}$$

This is the case where epitaxial layer is drier than the substrate.

c) Stranski-Karastanov mode (SK): Layer by layer then island growth (2D to 3D)

$$\text{Initially, } \gamma_{\text{substrate}} \geq \gamma_{\text{film}} + \gamma_{\text{interface}}$$

$$\text{Then, } \gamma_{\text{substrate}} < \gamma_{\text{film}} + \gamma_{\text{interface}}$$

The substrate surface has larger wet area at first but as the layer grows, strain accumulates and $\gamma_{\text{interface}}$ increases causing transition of flat surface to island.

All the growth mode is depicted in Figure 2.5 for illustration purpose.

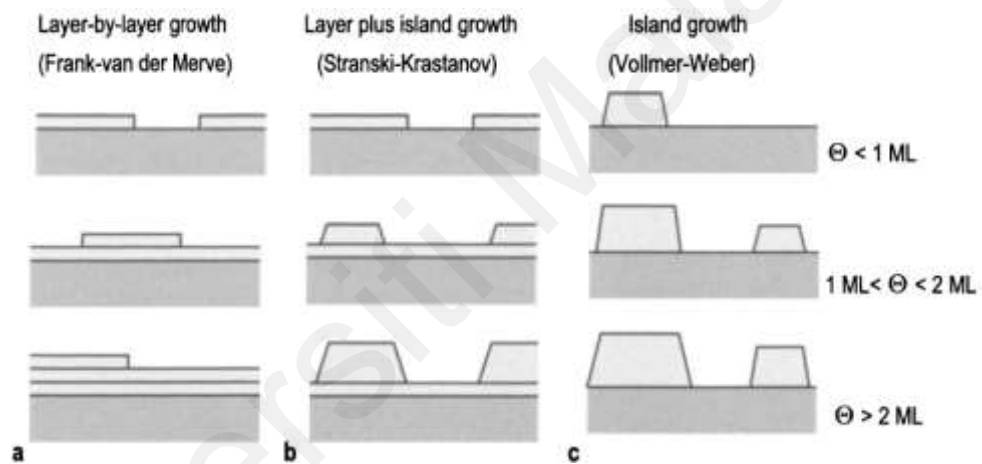


Figure 2.5: Schematic diagram for (a) FM growth mode, (b) SK growth mode and (c) VW growth mode (Oura et al., 2003), obtained from Growth of Thin Films.

However, growth modes are only applicable to growth conditions that are close to thermodynamics equilibrium which are at low supersaturation. At high supersaturation, the morphology is not affected by thermodynamics but by kinetics. Since kinetics involves the mobilities of adatom and it mostly affects the surface, hence it is regarded as growth morphologies. The most significant factor in growth morphologies is to control growth in term of adatoms kinetics. The atomistic process occurred in epitaxial growth is shown in Figure 2.6 where Terrace Step Kink (TSK) model is introduced.

The basic process involved are adsorption, surface diffusion, desorption and insertion or incorporation. Their diffusion rate D over the surface is given by:

$$D = \frac{d_{nn}^2 v_o}{4} e^{-E_m/kT} \quad (2.23)$$

From equation (2.22), E_m is the adatom migration activation energy, T is the substrate temperature, d_{nn} is the surface nearest neighbor distance and v_o is the vibrational frequency of adatom in initial state. To achieve 2D surface, the diffusion length of the adatom must be longer than terrace length and descend to the lower layer until it is filled up before the growth starts at the next layer.

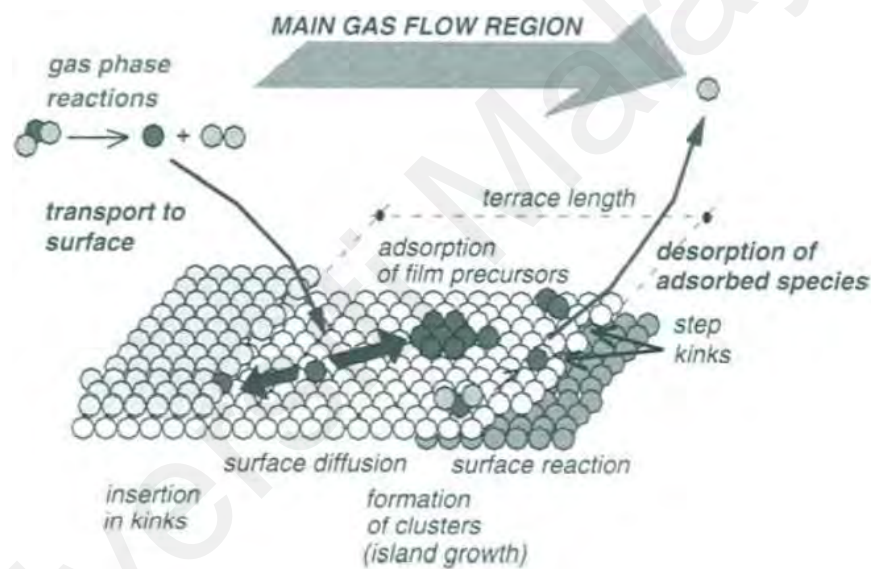


Figure 2.6: Schematic diagram of TSK model for atomistic process occurred in epitaxial growth(Masi & Kommu, 2001), obtained from Semiconductors and Semimetals.

An interesting model was presented by Rosenfeld et al.(Rosenfeld et al., 1995) where he first uses parameter of lower diffusion length during nucleation and changes to parameter of higher diffusion length to obtained 2D flat surface. This model is called two mobility and is illustrated in Figure 2.7.

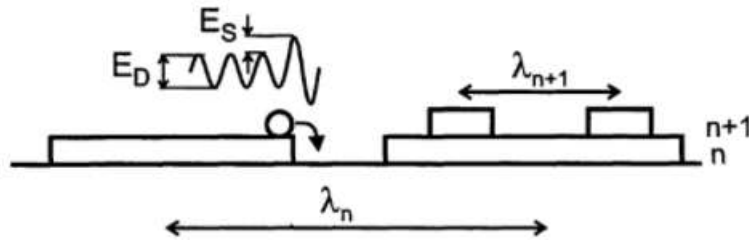


Figure 2.7: Schematic illustration of two mobility concept(Rosenfeld et al., 1999), obtained from Journal of Crystal Growth.

Total barrier for the adatoms are the terrace diffusion barrier E_D and step edge barrier E_s (also called as Ehrlich-Schwoebel barrier)(Ehrlich & Hudda, 1966; Schwoebel & Shipsey, 1966). To achieve 2D surface, adatoms mobility, λ_{n+1} must be greater than λ_n . However, two mobility method is not necessary as most of the substrate nowadays have a miscut of 0.1° to create TSK which is easier for growth and is proven to avoid screw dislocation(Lowndes et al., 1992).

2.3 Polarity of GaN

The polarity of GaN becomes of great interest when it comes to optoelectronic devices working in longer wavelength region. This is because polar GaN exhibit Quantum Confinement Stark Effect (QCSE) on the LED which deteriorate its efficiency(Deguchi et al., 1999). QCSE is the effect on light absorption or emission spectrum of a quantum well (QW) due to external electric field. Normally, electron and hole only occupy discrete energy level. However, when an external electric field is applied, conduction band shift to lower energy bandgap while the valence band shift to higher energy bandgap. This affects absorption or emission spectrum, causing redshift and non-radiative recombination. Moreover, the electric field shifts the electron and hole wave function to the opposite site and cause spatial separation. This reduces the overlap integral and thus increases the recombination lifetime and reduces its efficiency. Figure 2.8 shows energy band diagram of QW under influence of QCSE.

With electric field

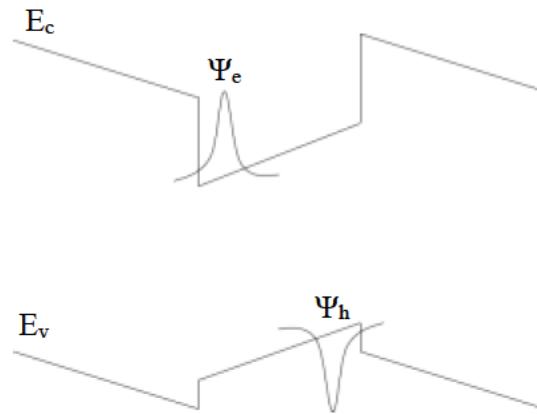


Figure 2.8: Schematic diagram for energy band of QW under influence of QCSE.

QCSE is caused by polarization effects arise from spontaneous polarization field and piezoelectric effect (Bernardini et al., 1997). Since Gallium and Nitrogen differ in electronegativity, Ga (1.81) and N (3.02), the N bond will have higher share of electrons and become slightly negative. This create a dipole moment and a polar bond is formed. If GaN can be grown in crystal structure of zinc blende (ZB) phase, then the spontaneous polarization will be cancel off due to intrinsic symmetry bonding of its geometrical structure. However, due to the lack of suitable substrate and thermal metastability of this phase, it must be done in wurtzite phase (*Group III Nitride Semiconductor Compounds - Bernard Gil - Oxford University Press, n.d.*). Unfortunately, wurtzite structure has the highest symmetry compatible with spontaneous polarization (Posternak et al., 1990) where the bond length along c -axis and perpendicular to c axis is different, the cancellation is incomplete resulting in a net moment along c -axis. On the other hand, piezoelectric effect is mostly contributed by lattice mismatch in the QW between InGa_xN_{1-x} and GaN and minorly between substrate and GaN (Martin et al., 1995). Since lattice constant of InN is bigger than GaN by 11%, the strain from tensile induced external electric field via piezoelectric effect. The matter become worse when dealing with LED for longer wavelength emission as higher indium (In) incorporation is needed.

Another limit on polar LED is the efficiency droop which happened in all InGaN based LED grown on polar GaN. Efficiency droop is the reduction of efficiency when the current density or operating temperature increases where it is called current droop and thermal droop, respectively. Normally, current droop is specifically discussed in InGaN/GaN based LED. Figure 2.9 shows the effect of efficiency droop on internal quantum efficiency when current increases.

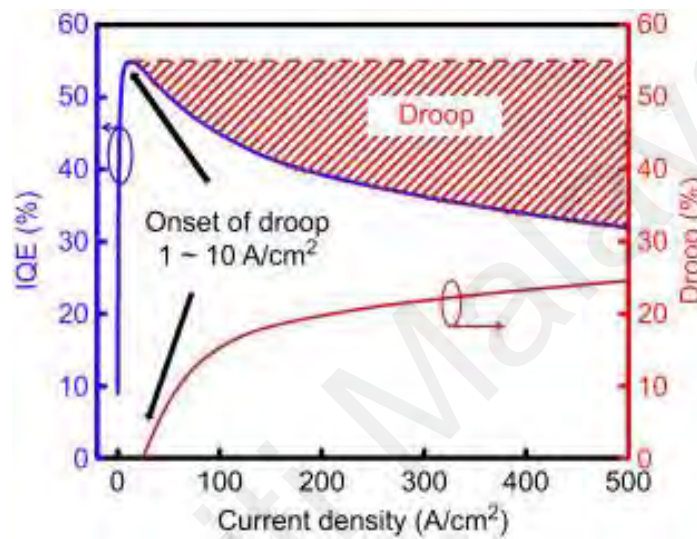


Figure 2.9: Internal quantum efficiency (IQE) and current droop as a function of current density for polar GaN/InGaN LED(Meyaard et al., 2013), obtained from Nitride Semiconductor Light-Emitting Diodes (LEDs): Materials, Technologies and Applications.

The origins of current droop is a topic most studied and most debatable in the research of *c*-plane GaN/InGaN LED. Many mechanisms such as Auger Recombination(Shen et al., 2007), carrier leakage(Kim et al., 2007), QCSE(Fiorentini et al., 1999) and so on were proposed in order to explain the phenomena. Nevertheless, the best solution for current droop is to reduce the current density by increasing the thickness of QW. *C*-plane GaN/InGaN LED normally have a quantum well thickness of only 3nm to mitigate the separation of electrons and holes due to QCSE. In order to increase the thickness of QW more than 3nm, semi- and non-polar GaN have been proposed to be the most possible solution.

Theoretical studies have showed that internal polarization fields can be reduced or completely avoided by redirecting them to other planes than the generally used c -plane (Romanov et al., 2006; Takeuchi et al., 2000) by rotating the growth orientation of GaN. Most importantly, Waltereit et al. have showed that growth of non-polar GaN is possible and the structures are free of electrostatic fields, resulted in efficiency improvement (Waltereit et al., 2000).

Figure 2.10 shows schematic of some typical semi- or non-polar GaN. Semi-polar is where the GaN grew slanted from c -plane, whereas non-polar GaN is grown perpendicular to the c -plane. The polarization can be calculated by the equation proposed by Romanov et al. (Romanov et al., 2006) where for a plane tilted from c -plane by angle θ , the polarization along vertical axis at GaN/InGaN is expressed as:

$$\Delta P_{tot} = P_{pz}^{InGaN} + (P_{sp}^{InGaN} - P_{sp}^{GaN}) \cos \theta \quad (2.24)$$

Where ΔP_{tot} is the total polarization difference between InGaN and GaN layer and P_{sp}^{InGaN} and P_{sp}^{GaN} are spontaneous polarization of InGaN layer and GaN layer respectively. P_{pz}^{InGaN} is the strain affected piezoelectric polarization in InGaN layer which also varies with angle θ .

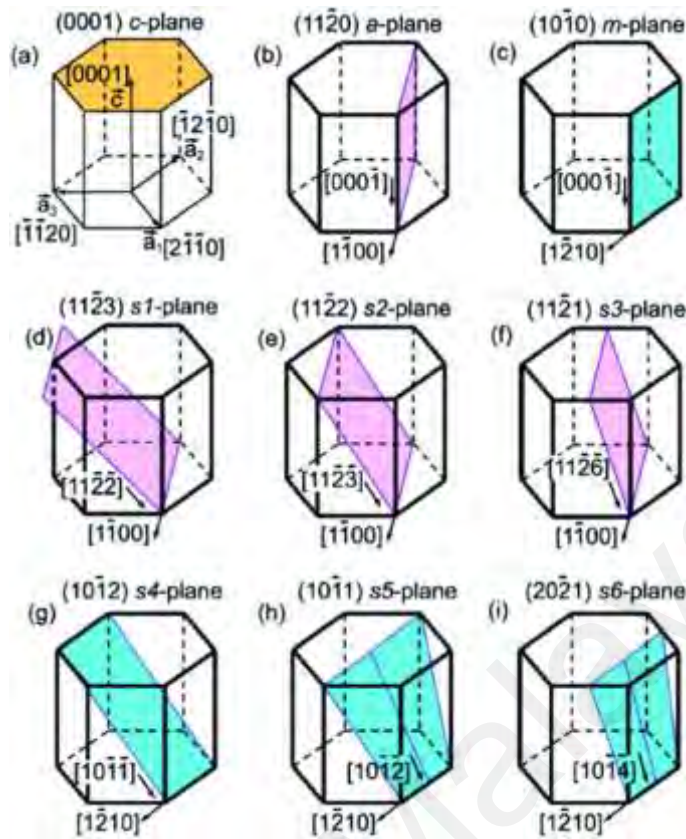


Figure 2.10: Schematic of various commonly grown semi- and non-polar GaN(Romanov et al., 2011), obtained from Journal of Applied Physics.

Figure 2.11 illustrates InGaN polarization with various indium composition as a function of slanted angle from c -axis. As observed, the polarization changes with the angle θ . Negative polarization after 55° is attribute to higher slanting angle where the resolved polarization on the horizontal axis is higher than the vertical axis. 0° represent the c -plane or polar GaN which shows the highest polarization. Angle between 0° and 90° are the planes of semi-polar GaN which shows a decrease in polarization whereas 90° is the a - or m -planes of non-polar GaN where no polarization are found.

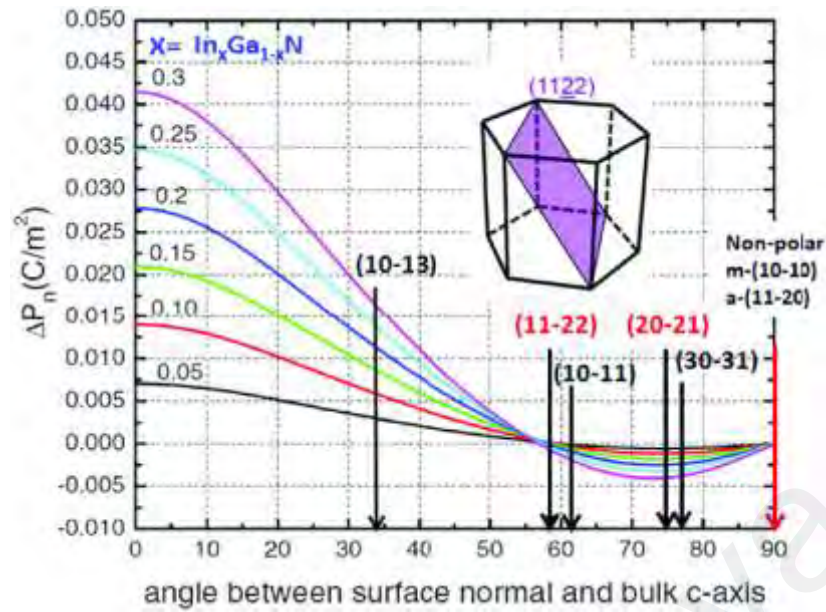


Figure 2.11: InGaN polarization with various indium composition as a function of angle between surface normal and c -axis (T. Wang, 2016), obtained from Semiconductor Science and Technology.

In the same year of 2006, Okamoto et al. (Okamoto et al., 2006) showed that non-polar GaN LED suffers little effect from current droop, while Funato et al. also showed similar effect for semi-polar GaN LED. These discoveries have increased the interest in semi- and non-polar GaN growth. To fabricate longer wavelength LED, more indiums are required. Although non-polar GaN is shown to be more promising in solving the problem of QCSE, but semi-polar GaN is proven to have better indium incorporation especially $(11\bar{2}2)$ GaN which is a better choice for long wavelength emitter. Northrup showed that for the same indium chemical potential, indium incorporation depends on the surface structure (Northrup, 2009). Lower strain repulsive interaction is found between In and the semi-polar $(11\bar{2}2)$ GaN surface compared to those non-polar or polar GaN surface. This can be understood through Figure 2.12.

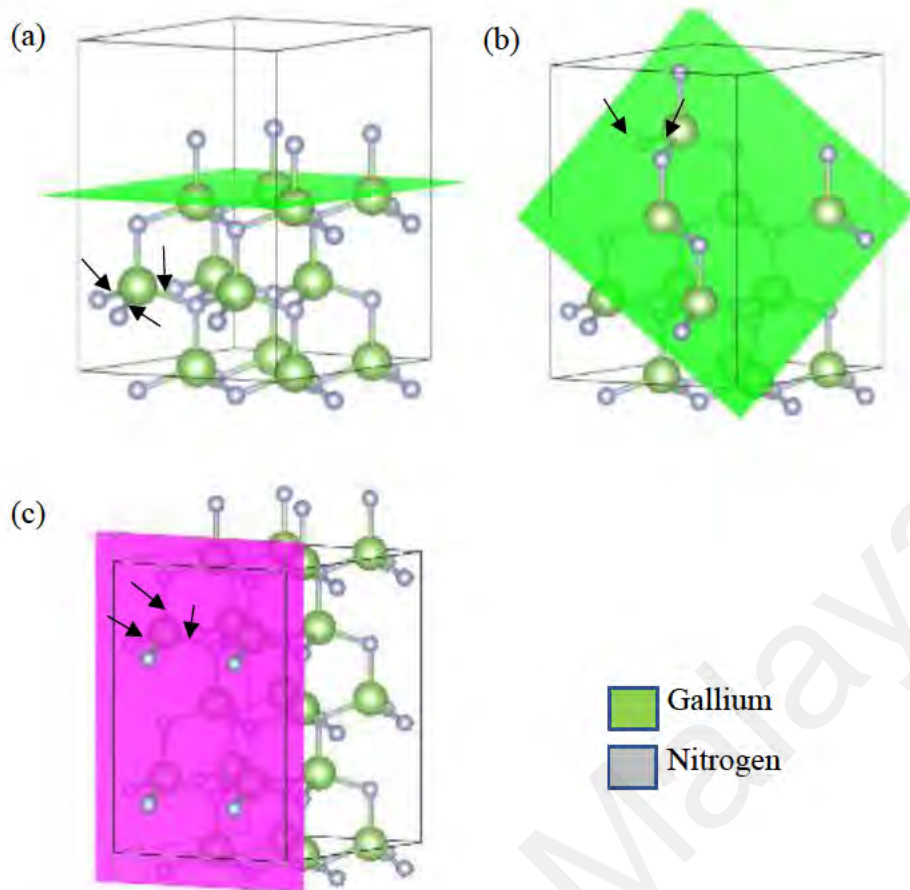


Figure 2.12: Schematic of crystal structure on the surface of (a) Polar, (b) Semi-polar ($11\bar{2}$) and (c) Non-polar GaN.

Figure 2.12 shows the crystal bond structure of different GaN surface. The arrows drawn are intended to show the bonds which are readily to react on the particular surface. In the case of polar GaN surface, it can be observed that In atom needed to form bond with the 3 nitrogen atoms. However, InN is 11% longer than GaN bond; incorporation of In will cause a strain repulsive interaction with the surface bonds. Similar case is found in non-polar GaN where there are 3 bonds (arrows shown beneath the pink surface plane) ready to attach with incoming atoms. For the case of semi-polar GaN, only 2 nitrogen bonds (beneath the green surface plane) are available. This gives In atoms more degree of freedom to adjust themselves and thus, there is a lower strain repulsive interaction and lower chemical potential are needed. A better indium incorporation at semi-polar GaN also implies that InGaN can be grown at higher temperature (explanation of InGaN

needed to grow at lower temperature are discussed in the section of reaction kinetics) which also helps in improving its crystal quality. Among the semi-polar GaN, study also shown that (11 $\bar{2}2$) GaN has the highest indium incorporation(Zhao et al., 2012).

Hence, it can be concluded that semi-polar GaN is most suitable for longer wavelength LED. (11 $\bar{2}2$) GaN is worth the study, as it has the lowest polarization effect and highest indium incorporation. However, semi-polar GaN suffers from high defects and dislocation density where its crystal quality cannot be compared with polar GaN. Next section will be discussing its defects and ways to overcome the problems.

2.4 Defects

2.4.1 Origin of defects.

Defects in epitaxy means dislocations where atoms are not arranged in an orderly manner. Defects normally associated with heteroepitaxy which revolves around in-plane lattice mismatch between the substrate and epitaxial film. The in-plane lattice mismatch is defined by the surface which substrate and epitaxial film will form bond. Lattice mismatch f is defined:

$$f = \frac{a_{sub} - a_{epi}}{a_{sub}} \quad (2.25)$$

where a_{epi} and a_{sub} is crystal lattice of epitaxial layer and substrate, respectively. Figure 2.13 illustrates the schematic of in-plane matching of c -plane AlN and c -plane substrate. As can be observed, not all bonds are formed with every atoms on the surface due to lattice mismatch.

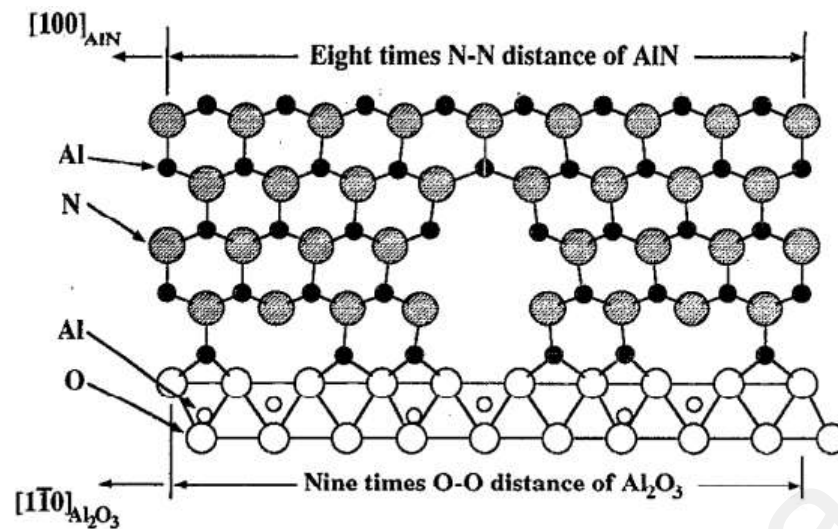


Figure 2.13: Schematic of cross-sectional plane for [0001] AlN grown on [0001] sapphire substrate(Sun et al., 1994), obtained from Journal of Applied Physics.

Epitaxial layer grown with lattice mismatch up to certain thickness will cause strain built up large enough that plastic deformation occurred and result in introduction of dislocations. Such dislocations are normally called misfit dislocation and serve to relieve the bulk and interfacial stress. Presence of stress will change the lattice of atoms and change the electronic states of epitaxial layer. The shift in electronics state will introduce the unwanted shallow defect energy level in the band gap. The situation became worst when dislocations break the symmetry of crystal structure and changes the energy level locally. The atoms at the edge of dislocation will be considered as dangling bonds and it sits between the valance and conduction states, introducing deep defect energy level(Holt & Yacobi, 2007). These will also act as a trap to attract impurities which further affects the energy band gap. Figure 2.14 shows the heteroepitaxial layer with (a) strain and (b) misfit dislocations. As observed, epitaxial film grown normally will follow the lattice constant of the substrate which are typically called pseudomorphic growth. However, when the growth continues until a certain thickness, it will follow its own bulk characteristic and island will form which agrees with SK growth mode. In the dislocated island, strain is relieved by formation of misfit dislocations.

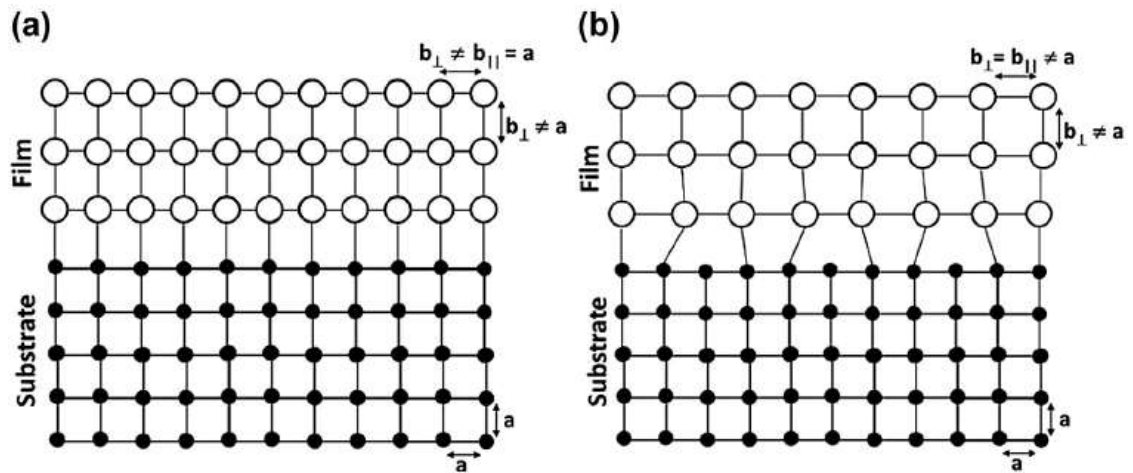


Figure 2.14: Heteroepitaxial layer with (a) strain and (b) misfit dislocation (Newman & Vahidi, 2015), obtained from Handbook of Crystal Growth: Thin Films and Epitaxy: Second Edition.

The thickness where strain built up large enough to form misfit dislocations are called critical thickness which was first proposed by Van der Merwe (Van Der Merwe, 1963). Critical thickness is highly dependent on the lattice mismatch of film and substrate where less mismatch led to thicker critical thickness. Here, this concludes the origins of dislocation and next section will discuss more about defects in semi-polar $(11\bar{2}2)$ GaN.

2.4.2 Defects in semi-polar $(11\bar{2}2)$ GaN.

A thorough study about defects structure in semi-polar $(11\bar{2}2)$ GaN has been conducted by Dasilya et al. (Dasilva et al., 2010) in 2010. It was found that the defects in $(11\bar{2}2)$ GaN is built up of 90% of Frank-Shockley partial dislocation, 8% of Shockley partial dislocation and 2% of a -type perfect dislocation (also called edge dislocation). This is in agreement with the study conducted by Tyagi et al., where the misfit dislocation generated at heterointerface in $(Al,In)GaN$ grown on $(11\bar{2}2)$ GaN substrate are mostly pure edge dislocation with Burgers vector of $b = 1/3 \langle 11\bar{2}0 \rangle$ (Tyagi et al., 2009). Edge dislocations are generated through the insertion or removal of half-plane crystal in the crystal structure. The dislocation line which describes the core of dislocation are orthogonal to the slip of Burgers vector b . Figure 2.15 shows the example of edge

dislocation which provide further insight of the dislocation itself. The black arrow indicates the direction of Burgers vector. Edge dislocations are the most prevalent as they have the lowest formation energy compared to c (screw) and a+c (mixed) type dislocation.

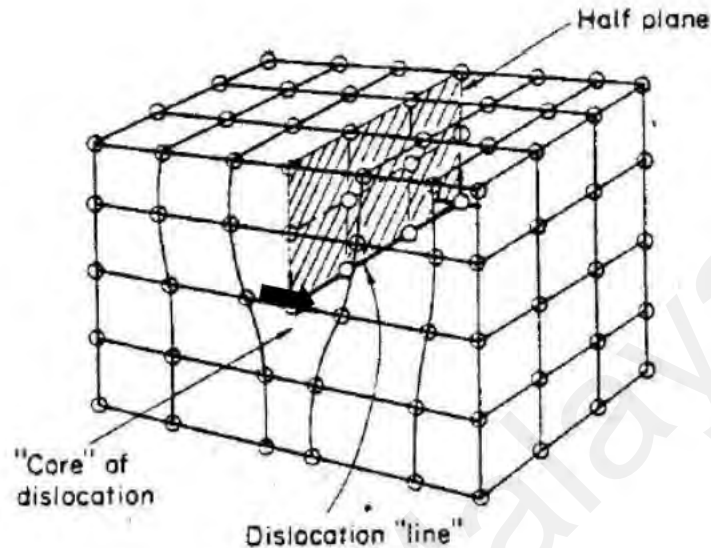


Figure 2.15: Image of edge dislocation, obtained from https://notes.engineeringonline.ncsu.edu/courses/ne/NE509/NE509_s09_14-2.pdf.

Sometimes, residual strain that is not compensated by misfit dislocation will be relaxed by threading dislocations (TD). Threading dislocations are the one that goes through the layer and extends to the surface. Pre-existing TDs from the substrate can penetrate and bend at the interface into misfit dislocations. After misfit strain is completely relaxed, misfit dislocation can be turn back into TDs again and it continues to penetrate through the film. TDs can be developed from imperfect in growth and existed in form of edge, screw and mixed dislocations. However, none of c and a+c type dislocations are observed in the case study of $(11\bar{2}2)$ GaN by Dasilva et al.(Dasilva et al., 2010).

To release the strain further, any perfect dislocations can be dissociated into two partial dislocations. They can be dissociated to Frank-Shockley or Shockley partial dislocations, depending on the type, orientation and interactions of the stacking faults (SF) formed(Dasilva et al., 2008; Komninou et al., 2005). Formation of partial dislocations is always accompanied by stacking faults which will affect the properties of optoelectronics

devices. When the Burgers vector is in plane with stacking fault, the dislocation is Shockley Partial and if the Burgers vector is perpendicular to stacking fault plane, it is Frank-Shockley partial dislocation. Frank-Shockley partial dislocation is a sessile dislocation (immobile

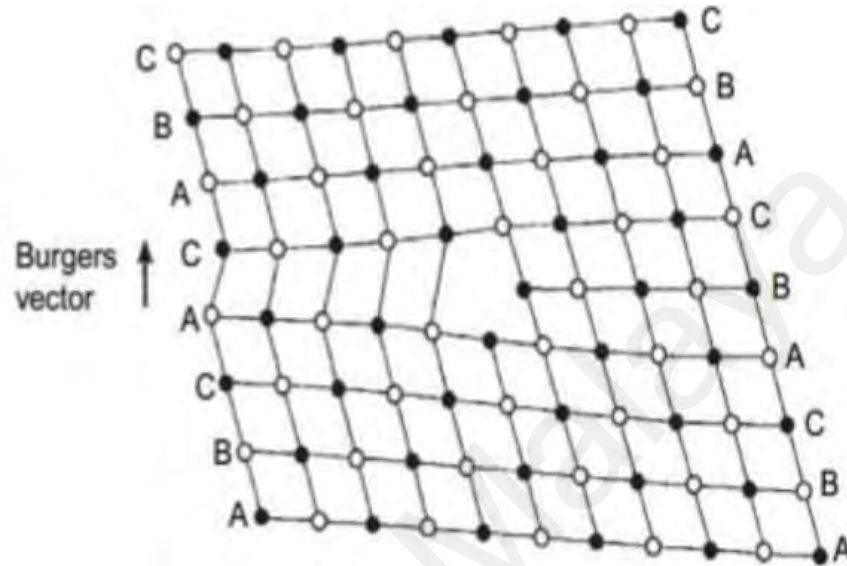


Figure 2.16: Illustration of Frank-Shockley partial dislocation by removal of a plane, obtained from https://notes.engineeringonline.ncsu.edu/courses/ne/NE509/NE509_s09_14-2.pdf.

dislocation) where it cannot glide under application of stress but it can be moved by a climb. This is formed by inserting or partly removing a plane and has a Burgers vector of $b = \frac{1}{6}\langle 2\bar{0}\bar{2}3 \rangle$. The formation of Frank-Shockley partial dislocation is illustrated in Figure 2.16. On the other hand, Shockley partial dislocation is a glissile dislocation (mobile dislocation) which can glide within its own glide plane and is formed by dissociation of a perfect dislocation into two parts. It has a Burgers vector of $b = \frac{1}{3}\langle 1\bar{1}00 \rangle$. Example of Shockley partial dislocation is illustrated in Figure 2.17.

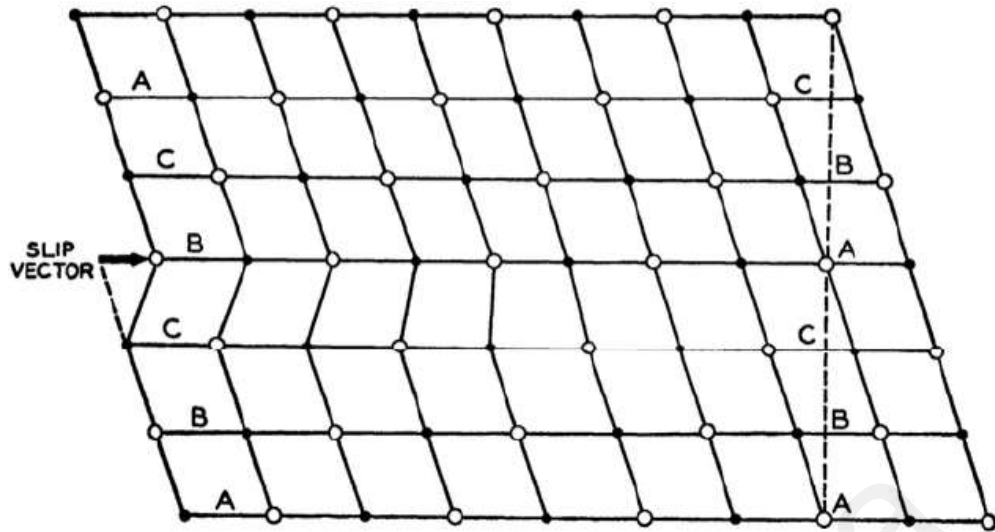


Figure 2.17: Illustration of Shockley partial dislocation by a slip of vector, obtained from https://notes.engineeringonline.ncsu.edu/courses/ne/NE509/NE509_s09_14-2.pdf.

It should also be also noted that majority of the defects in semi-polar $(11\bar{2}2)$ GaN are Stacking Faults (SF) as they are bound by partial dislocations. Stacking faults energy provide a force to pull the dislocations back together. The formation of SFs is caused by deposition errors or deviation from thermal equilibrium (supersaturation) during growth (Ernst & Pirouz, 1989; Vennéguès et al., 2007). Most of the stacking faults found are Basal Stacking Fault (BSF) I_1 which is bound by Frank-Shockley partial dislocation. BSF I_1 is formed by either removal or insertion of a plane with a slip of Burgers Vector $\frac{1}{3}\langle 1\bar{1}00 \rangle$ on one part of the crystal to decrease the fault energy. It changes the perfect atomic sequence of ...ABABAB... to ...ABABCBCBCB... as shown in Figure 2.18 (a) with a displacement vector $\vec{R} = \frac{1}{6}\langle 20\bar{2}3 \rangle$. The second stacking faults found are Basal Stacking Fault I_2 which is bound by Shockley partial dislocation. BSF I_2 is formed by a direct $\frac{1}{3}\langle 1\bar{1}00 \rangle$ shear of

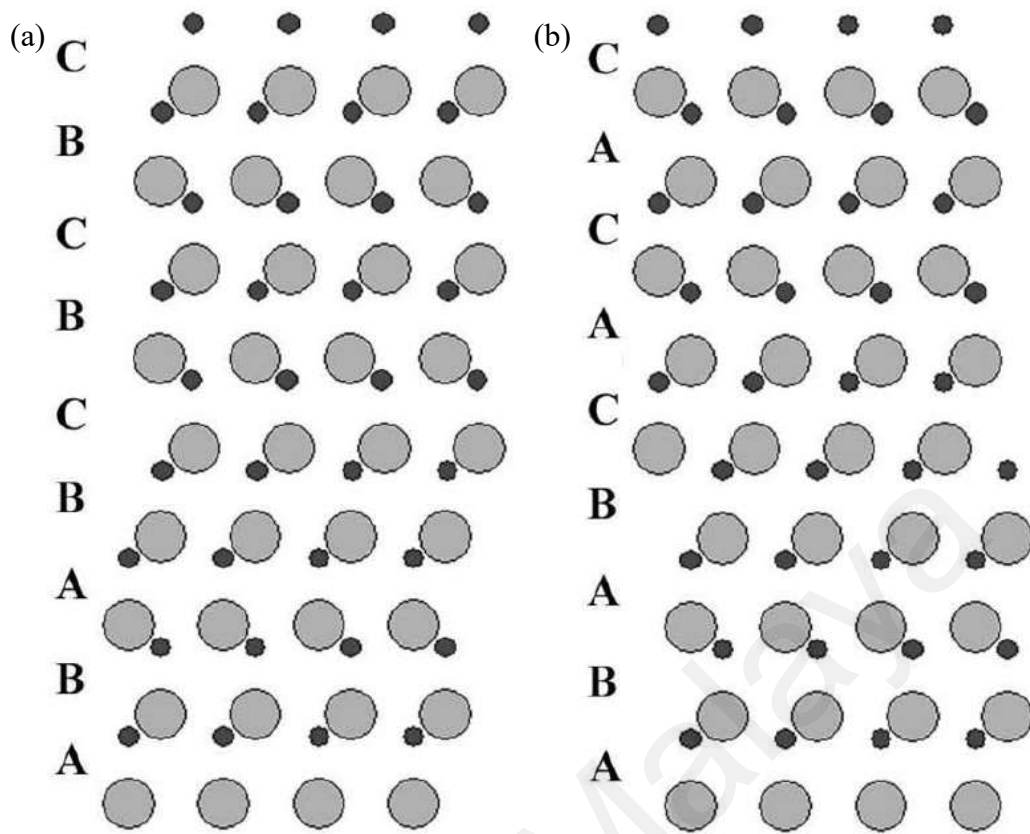


Figure 2.18: Illustration of stacking sequence for (a)BSF I₁ and (b)BSF I₂ (Dasilva et al., 2010), obtained from Gallium Nitride Materials and Devices V.

crystal with respect to the other or dissociation of perfect dislocation into two Shockley partials. The atomic sequence is changed to ...ABABACACA... (Figure 2.18 (b)) under its influence with a displacement vector $\vec{R} = \frac{1}{3}\langle 1\bar{1}00 \rangle$. BSF I₁ is more numerous as it has the lowest formation energy which is then followed by BSF I₂. BSF I₁ is likely to be formed during growth, while BSF I₂ is caused by deformation from stress during or after growth. The stress from after growth is attributed to difference in thermal expansion coefficient of heteroepitaxy during cooling. TDs and PDs will also appear during cooling process. BSF I₃ and E will not be discussed here as they require higher formation energy and are not visible in semi-polar (11 $\bar{2}2$) GaN.

Normally, BSF is either ended by partial dislocation or being folded from one plane to another with the formation of Prismatic Stacking Fault (PSF)(Dasilva et al., 2010). PSFs

in $(11\bar{2}2)$ GaN normally act on $(11\bar{2}0)$ plane with displacement vector of $\vec{R} = 1/2\langle 1\bar{1}01 \rangle$.

Figure 2.19 shows the effect of PSF on atomic arrangement of GaN.

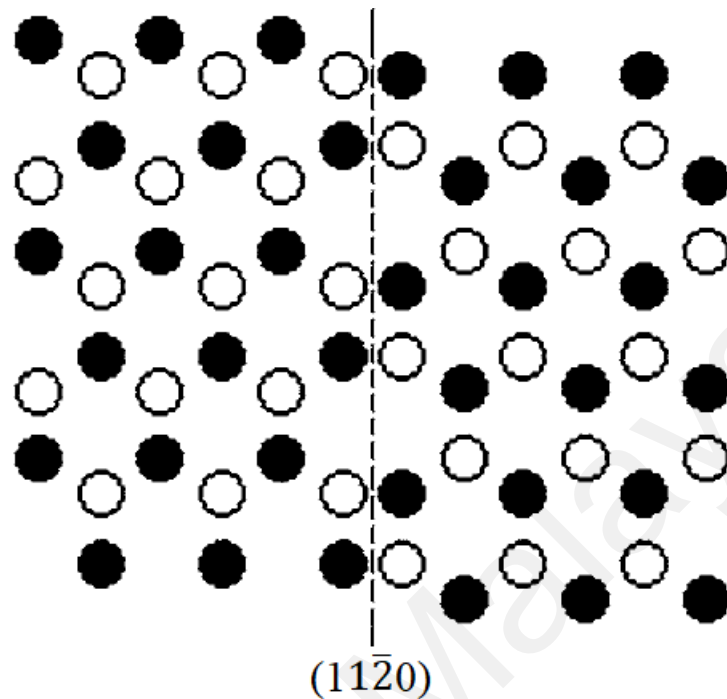


Figure 2.19: Atomic models of PSF in wurtzite GaN. Black and white circles both representing Gallium atoms (Dasilva et al., 2010), obtained from Gallium Nitride Materials and Devices V.

In $(11\bar{2}2)$ GaN, presence of PSFs may help compensate the geometrical shift along growth axis due to their out-of-plane component. However due to geometrical reasons, their extension towards the growth direction is limited, forcing more formation of BSF I₁ thus contributing to their density.

2.5 Arrowhead

Arrowhead has always been a prominent surface feature for semi- and non-polar GaN. Some may consider it as a defect and it has been described in many publications with different names, sometimes as hillock (Masui et al., 2010) and sometimes as chevron (Brasser et al., 2018). Figure 2.20 below shows an example of arrowhead as appeared in literatures with different names.

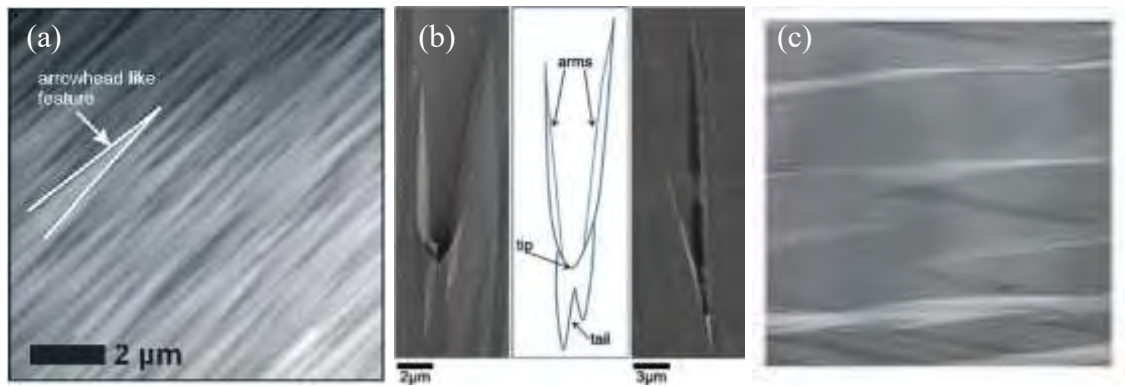


Figure 2.20: Special surface feature of non- and semi-polar GaN appear in literature as (a) arrowhead(Wernicke et al., 2008), obtained from *Physica Status Solidi (C) Current Topics in Solid State Physics*, (b) chevron(Brasser et al., 2018), obtained from *Journal of Applied Physics* and (c) hillock(Kneissl & Wernicke, 2014), obtained from *III-Nitride Semiconductors and their Modern Devices*.

The arrowhead disrupts the production of flat surface with low roughness. Moreover, it causes uniformity problems in InN incorporation in terms of the quantum well(Holland et al., 2016) where more indiums are incorporated on the arrowhead or the tip to tail region of the chevron. Studies even show that more non-radiative recombination occurs at the arrowhead region results from disruption of its structure(Brasser et al., 2018). To mitigate these problems, some studies have been carried out and explanations on its origin has been proposed.

Tim et al. at first proposed that the surface structure resulted from the tilt between sapphire and GaN as it fits well with the inclination angle of the arrowheads(Wernicke et al., 2008). Then, he further proposed that these were cause by threading dislocations(Wernicke et al., 2011). Other researcher such as Farrell et al. proposed that it is a result of screw dislocation intersecting the surface when spiral growth occurred(Farrell et al., 2010). Yisong et al. found a link between arrowhead, region of inversion domain and nucleation of GaN particles carrying bundle of dislocations originating from coalescence region(Han et al., 2015). While Zhao et al. speculated that it is due to crystallographic difference of semi-polar GaN and sapphire due to distinct adatom diffusion length and incorporation chances(Zhao et al., 2016).

However, the most likely mechanism for arrowhead formation can be obtained from Ploch et al. (Ploch et al., 2012). Ploch et al. deduced that the arrowheads are produced from interference due to different adatoms diffusion length at different direction. For the case of semi-polar (11 $\bar{2}$ 2) GaN, the activation energy for $[\bar{1}\bar{1}23]$ and $[1\bar{1}00]$ are 0.8 and 1.3 eV, respectively, due to the surface atomic atom spacing of 3.04 Å along $[\bar{1}\bar{1}23]$ and 5.52 Å along $[1\bar{1}00]$. Whereas, for the case of non-polar *a*-plane GaN, the activation energy for $[1\bar{1}00]$ and $[0001]$ are 0.63 and 0.32 eV, respectively, while for *m*-plane GaN, the activation energy for $[11\bar{2}0]$ and $[0001]$ are 0.21 and 0.93 eV, respectively. The atomic spacing for both *m*- and *a*-plane GaN along $[0001]$ direction are 3.25 Å in contrast to higher diffusion path of 5.29 Å and 5.63 Å along $[11\bar{2}0]$ and $[1\bar{1}00]$ for *m*- and *a*-plane GaN, respectively(Lymperakis & Neugebauer, 2009).

2.6 Growth of GaN on AlN and GaN nucleation layer

To obtain a good GaN layer, a low temperature buffer layer (LTBL) was normally grown as nucleation layer before growing the main layer. This method is unarguably good and easy until Zhao et al.(Zhao et al., 2016) reported better semi-polar (11 $\bar{2}$ 2) GaN crystal quality by utilizing double AlN nucleation layer method. By using this method, only mixed-type dislocation with either edge-components or screw-components are presented in the initial stages of GaN growth. As more GaN deposited, the pairs of screw or edge dislocations with opposite burger vector will annihilate each other and help relax the strain in GaN film. This indicates that the mixed-type dislocations with multislip systems is better than pure edge type dislocation in eliminating dislocations by cross slip. In 2018, Omar et al.(Omar et al., 2018) reported an even better crystal quality just by growing GaN with lower NH₃ flux (lower V/III ratio) on single AlN nucleation layer. The improvement due to the migration of Ga atom on the surface are facilitated upon using low NH₃ flux since there are few active N atoms.

Different method also been reported which helps to improve the crystal quality of semi-polar $(11\bar{2}2)$ GaN particularly two step growth of $(11\bar{2}2)$ GaN by varying pressure. Sun et al.(Sun et al., 2009) reported that islanding growth of $(11\bar{2}2)$ GaN under high pressure followed by islands coalescence under low pressure was very effective in reducing the stacking faults and dislocations. Under high pressure growth, the GaN grown will be very rough and effective in dislocation bending at inclined growth fronts and annihilate with each other in later phase. While under low pressure growth, the surface will be collated, and a smooth surface is formed.

2.7 Summary

This chapter has discussed in detailed the physics behind GaN epitaxy growth and advantages of growing GaN in semi-polar $(11\bar{2}2)$ plane. Moreover, the problems and characteristics of semi-polar $(11\bar{2}2)$ GaN have also been included. Next, research methodology and all the equipment used during the research will be discussed.

CHAPTER 3: METHODOLOGY

3.1 Introduction

The first section discusses on the experimental procedure for growing semi-polar (11 $\bar{2}2$) GaN epitaxial layer. The second section will discuss the Metal Oxide Chemical Vapor Deposition (MOCVD) used for deposition of crystal layer. The equipment used to characterize the grown samples are described in section 3.4.

3.2 Experiment Methods

Semi-polar (11 $\bar{2}2$) GaN epi-layers were grown on *m*-plane (10 $\bar{1}0$) sapphire substrate via MOCVD SR-2000, Taiyo Nippon Sanso, Japan. The precursors used were trimethylaluminum (TMA) for aluminum, trimethylgallium (TMG) for gallium and ammonia (NH₃) for nitrogen. The *m*-plane sapphire underwent a hydrogen cleaning for 10 mins at a temperature of 1125 °C. Then, nitridation was carried out in a flow of ammonia at 5 SLM for 30mins. After nitridation, AlN nucleation layer of 100 nm was grown with TMA flow of 98.5 sccm and NH₃ flow of 2.3 SLM at the temperature of 1050 °C before the growth of the GaN layer. Next, GaN was grown at fixed V/III ratio of 118 at a temperature of 1050 °C for 30 minutes and the reactor pressure was set to 13.3 kPa. The TMG and NH₃ flow rate for GaN epi-layer growth were varied sequentially during the fixed 30 minutes epitaxy growth. The 30 minutes GaN growth is then repeated with 100nm AlN nucleation layer grown by lowering TMA flow to 50 sccm and NH₃ flow to 1.2 SLM at a fixed V/III ratio of 1300. Figure 3.1 illustrates the epitaxy structure grown in this experiment. Hydrogen (H₂) was used as a gas carrier throughout the growth. After several series of gas flow rate variation, the best sample was selected and the process was repeated under different reactor pressure of 40 kPa, 70 kPa and 100kPa to investigate the effect of pressure on the epitaxial GaN layer.

The structural properties of GaN epi-layers were characterized by Rigaku high-resolution x-ray diffraction (HR-XRD) while surface morphology was examined by Park System NX-10 atomic force microscopy (AFM) via non-contact mode and by Hitachi SU8220 field-emission scanning electron microscope (FESEM).

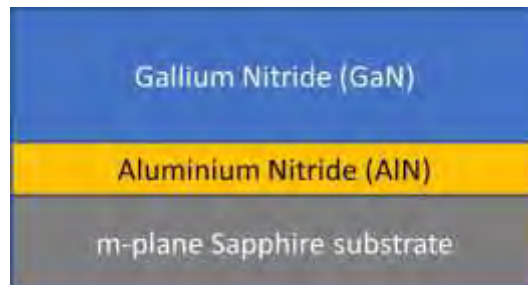


Figure 3.1: GaN with AlN nucleation layer grown on the *m*-plane sapphire substrate.

3.3 Metal-organic Chemical Vapor Deposition (MOCVD)

Metal-organic Chemical Vapor Deposition is a machine used to produce crystalline thin films via chemical vapor deposition. It is preferred for its advantage in overcoming the difficulty in the formation of thin films from thermodynamically metastable alloys. It was first invented by Harold M. Manasevit in 1968. The precursor gases are injected into the reactor with carrier gas and deposition occurs via the control of gas flow, pressure and temperature. The metal-organic precursors normally used for group III elements are: Trimethylgallium (TMG), Trimethylaluminum (TMA) and Trimethylindium (TMI) which are the source for Ga, Al and In, respectively, while group V element can be derived from ammonia (NH₃) which is the source for N. The carrier gas is either hydrogen (H₂) or nitrogen (N₂). The gas flow for group III elements is controlled in the unit of standard cubic centimeters per minute (sccm), while group V elements is controlled in the unit of standard liter per minute (slm). The temperature is controlled by the heater on the substrate tray. The model of MOCVD used in this work is Taiyo Nippon Sanso SR-2000 and its temperature can be heated up to 1180°C. The system is controlled by gas

circuit as electronics signal are avoided because electrons might affect the growth in the reactor. Figure 3.2 shows the schematic diagram of the MOCVD reactor.

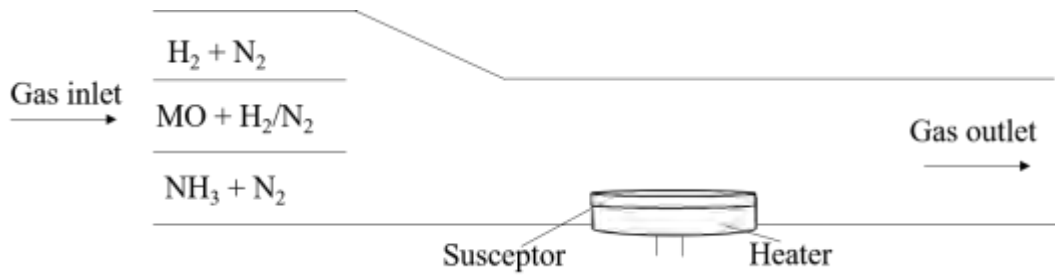


Figure 3.2: Schematic diagram of MOCVD reactor.



Figure 3.3: Susceptor, wafer holder and 2" wafer used in this experiment.



Figure 3.4: Taiyo Nippon Sanso SR-2000

3.4 Equipment for characterization

The surface morphology is analyzed using atomic force microscopy (AFM) and field-emission scanning electron microscope (FESEM), while the structural properties is examined by using high-resolution x-ray diffraction (HRXRD).

3.4.1 Atomic force microscopy (AFM)

Atomic force microscopy (AFM) is used for quantitative measurement to determine the roughness of the film surface. It provides a measurement scale of few micrometers (μm) down to 200nanometers (nm). It is a non-optical surface interrogation method which uses a physical probe to measure the morphology and topology of the surface. The working principle of AFM lies on the nanoscale tip that is attached to a cantilever. The tip is used to scan across the surface line by line in a horizontal or vertical direction depending on the user and the topology of the surface. When the tip is scanning across the surface, the atomic force between the surface and tip forces the cantilever to bend and the cantilever act as a spring which obey Hooke's law. At the same time, a laser beam is pointed at the back of the cantilever and is reflected to a split photodetector. The bending indicates the tip-sample interaction and the reflection of the laser to the photodetector measures and transfers the information to the computer for further analysis. The simple working principle of AFM is shown in Figure 3.5. There are 3 modes available: contact mode, tapping mode and non-contact mode. In contact mode, the tip is pressed to the surface and scan across the surface. Tapping and non-contact mode is design to protect the tip and the sample. In this mode, cantilever vibrates at near its resonance frequency. The tip moves up and down in a sinusoidal motion and the motion is reduced by interaction force of the sample surface. The only difference is that tapping mode will still make contact with the sample while non-contact mode relies on the van der Waals interaction of the tip and the surface. The model of AFM used is Park System NX-10 as

shown in Figure 3.6 and non-contact mode with $5 \times 5 \mu\text{m}$ and $25 \times 25 \mu\text{m}$ is used throughout this work.

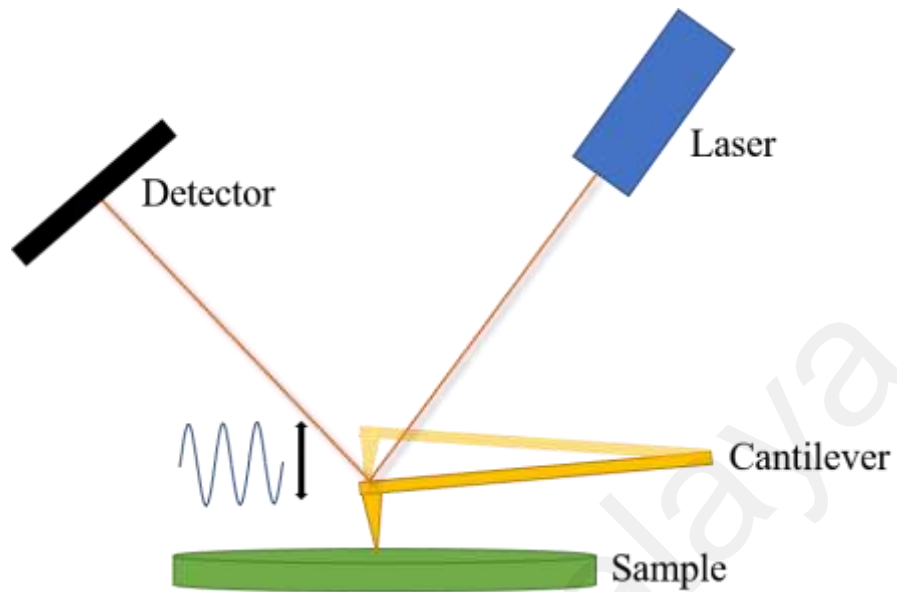


Figure 3.5: Schematic diagram for working principle of AFM.



Figure 3.6: Park System NX-10 AFM.

3.4.2 Field-emission scanning electron microscope (FESEM)

FESEM is an instrument which provide wide information from the sample surface by scanning electron beam over the surface while displaying the information based on detectors available. FESEM works just like SEM but with higher resolution. SEM uses focused electron beam that interact with the sample to produce topological image. Upon contact, focused electron beam will produce secondary electrons (SE), backscattered electrons and characteristic X-ray which can be detected with various detectors based on user needs and display the analysis on a monitor. The main components involve electron source, electromagnetic lenses, detectors, chamber and computer.

SEM image is formed from signals detect from interaction between electron signals and scanned sample surface. Normally, two interactions can occur, elastic and inelastic interactions. During inelastic interaction, low-energy SE are released from the sample after bombardment of the primary electron beam. On the other hand, elastic interaction is due to deflection of primary electron beam upon collisions with sample nucleus or electrons. The deflection of scattered electrons at angle more than 90° are called back scattered electrons (BSE). SE mode will be discussed further as it is utilized during characterization.

SE mode is the most common type used in SEM/FESEM image processing. The incident electrons have lower energy thus signals can only be detected few nanometers from the sample surface. Hence, SE is most effective to produce topological image of the sample. SE that reaches the detector will produce image while obstructed SE will produce dark contrast. Furthermore, low voltage of primary electron beam will mostly produce SE from the utmost surface of the sample thus accurately depict the detailed topological structure of the sample.

The only difference between FESEM and SEM is that FESEM uses field emission gun that relies on potential gradient to emit electron beams rather than thermionic electron source. The field emission gun (FEG) of FESEM is a single pointed sharp tip which allow formation of electron probes of 0.5 nm and with low acceleration voltage, high resolution of surface topological images up to 2-3 nm resolution. The principle of operation involves two anodes. The first anode is used to control and extract electron beams and act as electrostatic lens and the second anode to accelerate them. All the samples from the experiment will be analyzed by FESEM at SE mode with 1, 2, 3 and 10k resolution.



Figure 3.7: FESEM Hitachi SU8220.

3.4.3 High-resolution x-ray diffraction (HRXRD)

The HRXRD utilize the working principle of Bragg diffraction to operate and help to determine the structure, orientation and mismatch of a crystal. In this work, it is used to study the crystal orientation, crystalline and defects of semi-polar (11 $\bar{2}$ 2) GaN epitaxial

layer. This technique is non-destructive which did not involve cutting or damaging the sample.

In HRXRD, the incident x-ray is directed onto the crystal causing the electron to excite to higher energy state. When the electrons relaxes down to its initial energy state, they will re-emit circular wave which have similar wavelength with the x-ray. These waves will interfere with each other and cause constructive and destructive interference as shown in Fig 3.8. The condition for constructive interference is called Bragg diffraction.

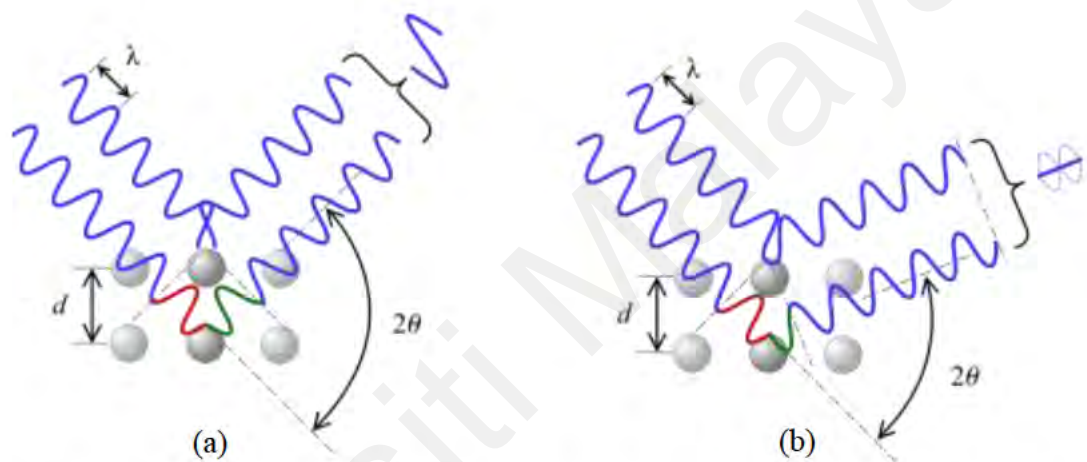


Fig 3.8: (a) Constructive and (b) destructive interference occurs during interaction of x-ray and atoms, obtained from https://en.wikipedia.org/wiki/Bragg%27s_law.

Bragg diffraction occurs when radiation with similar wavelength to atomic lattice is scattered by the atoms of a crystal and undergoes constructive interference. When the wave scattered from lattice plane with a distance d interfered constructively, the waves are still in phase since the pathlength difference is equal to an integer multiple of the wavelength. The pathlength difference between two waves for maximum intensity of constructive interference due to cumulative effect of reflection in successive crystalline plane is given by

$$2d \sin \theta = n\lambda \quad (3.1)$$

where θ is the incident angle for maximum intensity, d is the lattice spacing, n is a positive integer and λ is the wavelength of incident wave (wavelength of x-ray in this case). The schematic diagram for Bragg diffraction is shown in Figure 3.9.

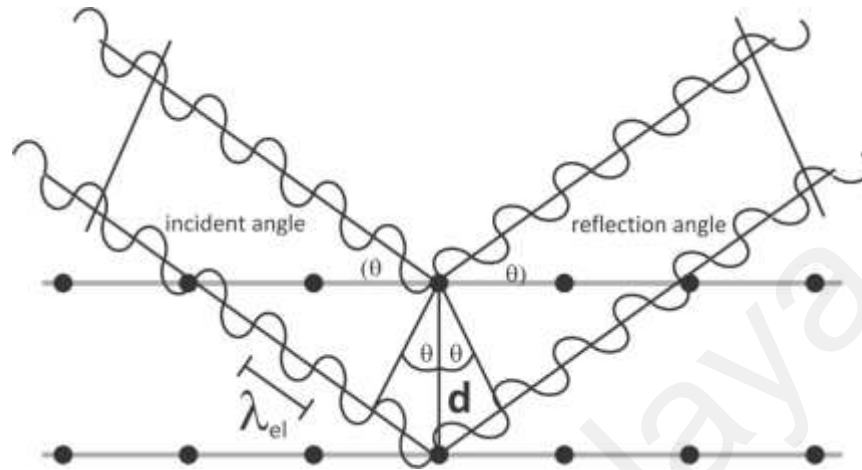


Figure 3.9: Schematic diagram of Bragg diffraction, obtained from <https://letstalkacademy.com/x-ray-diffraction/>.

For a highly ordered crystal, the XRD pattern produced from constructive interference is very sharp and thus have low full width at half maximum (FWHM) value while for a crystal with many defects, it will have a higher FWHM value. Hence, the crystal quality of GaN films can be evaluated by comparing its FWHM values obtained from HRXRD.



Figure 3.10: Rigaku high-resolution x-ray diffraction (HR-XRD).

There are few scans that can be made by HRXRD which give important information. They are $\omega/2\theta$, on-axis x-ray rocking curve (XRC) measurement and off-axis XRC measurement. These measurements are determined by the movement involve in HRXRD as depicted in Figure 3.11.

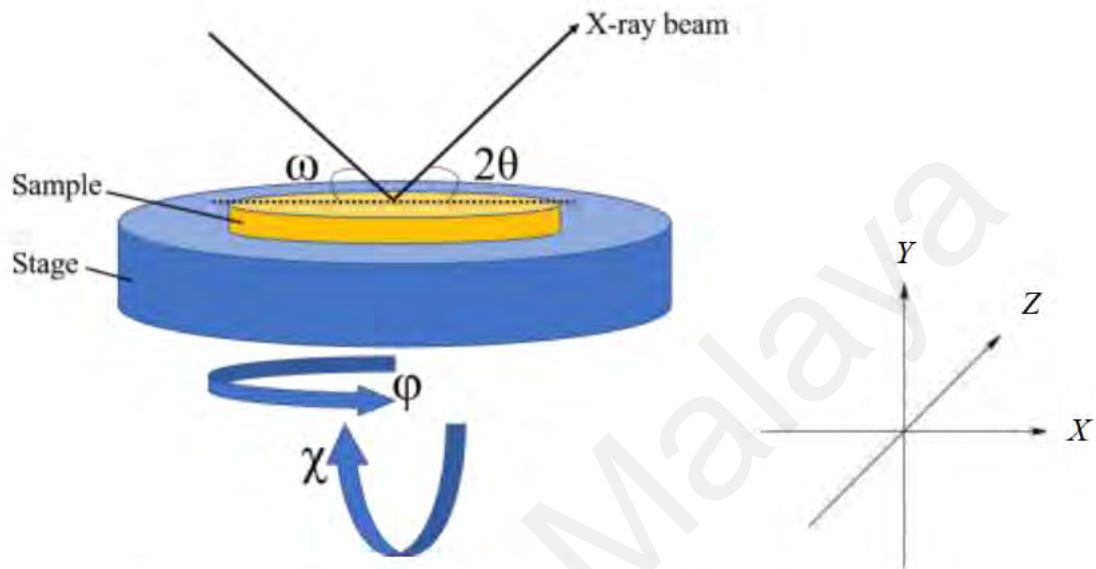


Figure 3.11: Schematic diagram of HR-XRD stage mobility.

The $\omega/2\theta$ scan allows the study on phase analysis where the elements and orientation of film can be determine. During this scan, a movement of x-ray source by ω is followed by a movement of detector by 2θ and this $\omega/2\theta$ scan occurs with the rotation around the z-axis.

The x-ray rocking curve measurement is used to measure the x-ray intensity along the reciprocal lattice point to determine the crystal quality of the film. In on-axis XRC measurement, the sample is rotated 360° along ϕ (rotation around the Y-axis) with each measurement taken at an interval of 30° . The 0° and 90° was set at $[\bar{1}1\bar{2}3]$ and $[1\bar{1}00]$ of the crystal direction, respectively. For the case of semi-polar $(11\bar{2}2)$ GaN, a M-shaped azimuthal FWHM values will be obtained from this scan.

For the off-axis XRC measurement, only certain planes which correspond to certain dislocation factor are measured. The sample will be aligned to their respective φ with a tilt angle of χ (rotation along x-axis). The list of FWHM broadening factor for each off-axis plane is listed in Table 3.1. The error for FWHM of all planes is 0.6% (from standard deviation of 10 scan samples) which is negligible, hence will not be shown in the Chapter 4 and 5. During the experiment, the XRD will be operate with 2-bounce (220) Ge monochromator (with incident and receiving slits set at 1 mm) without analyzer crystal at the receiving optics.

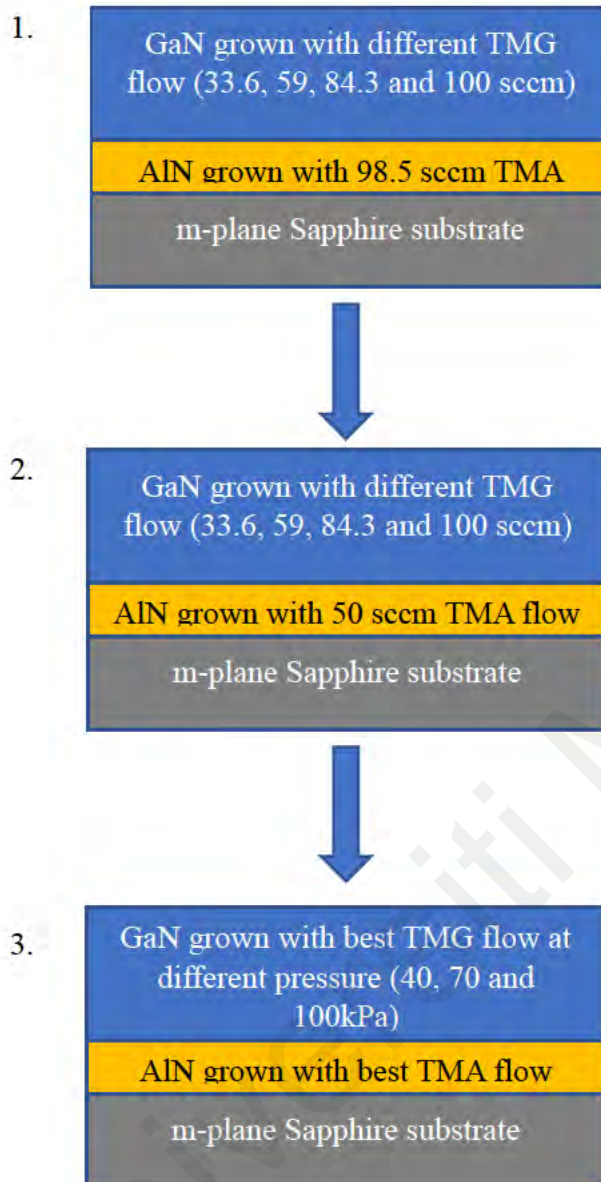
Table 3.1: FWHM broadening factor for each off-axis plane.

Off-axis plane	FWHM broadening factor
$(10\bar{1}0)$ and $(20\bar{2}0)$	BSF I_1 and I_2
$(000n)$	partial dislocations and/or perfect dislocations
$(10\bar{1}1)$	Perfect dislocations
$(11\bar{2}0)$	Prismatic stacking faults (PSF)

3.5 Summary

The design or methodology of this research has been discussed in this chapter. In addition, the fundamental principle of all the equipment used in this research which includes AFM, FESEM and HR-XRD have also been included. Finally, overview of the research flow will be shown in next page.

3.6 Overview of research flow



CHAPTER 4: THE EFFECT OF GAS FLOW RATE ON SEMI-POLAR (112̄2)
GaN EPITAXIAL LAYER

In this work, the effect of gas flow rate variation at fixed V/III ratio on the crystalline quality and surface morphology of semi-polar (112̄2) gallium nitride epitaxial layer is studied. The first experiment series comprises the study of GaN grown for 30 minutes at a fixed V/III ratio of 118 with different TMG gas flow rate on AlN. The second experiment series is repeated with AlN nucleation layer grown at a lower TMA gas flow rate (from 98.5 to 50 sccm) but also kept at a fixed V/III ratio of 1300 to study the effect of TMA gas flow rate variation at AlN nucleation layer towards GaN. All the samples are characterized by HRXRD, FESEM and AFM and their respective results are discussed. The name of the samples with their respective parameters is shown in the Table 4.1 below and the schematic diagram for this experiment series is shown in Figure 4.1.

Table 4.1: Growth parameters variation adapted in this work.

TMA gas flow (sccm)	TMG gas flow (sccm)	NH ₃ gas flow (SLM)	Sample
98.5 (NH ₃ at 2.3 SLM)	33.6	0.4	S4
	59	0.7	S3
	84.3	1.0	S2
	100	1.2	S1
50 (NH ₃ at 1.2 SLM)	33.6	0.4	SA4
	59	0.7	SA3
	84.3	1.0	SA2
	100	1.2	SA1

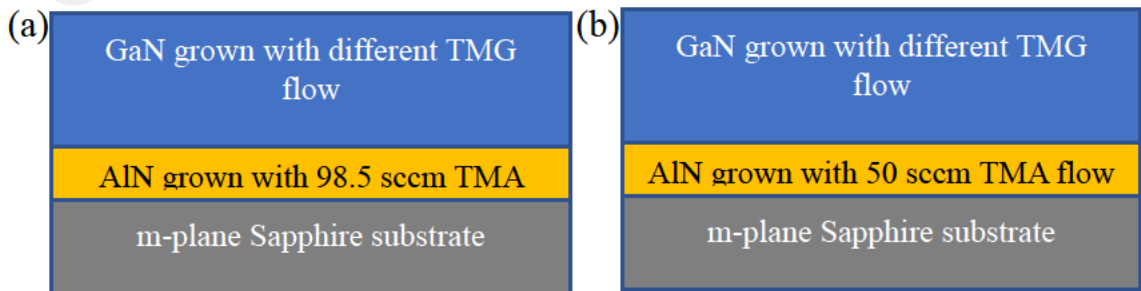


Figure 4.1: Schematic diagram of experiment series (a) first and (b) second where the TMG and TMA gas flow rate variation is kept at fixed V/III ratio.

4.1 Variation of TMG gas flow on AlN growth with TMA flow of 98.5sccm at fixed V/III

4.1.1 Phase Analysis

In order to investigate the effect of the gas flow on the crystal quality of grown GaN epilayer, XRD measurement was carried out. Figure 4.2 shows the HR-XRD 2θ - ω scans for GaN grown on the AlN nucleation layer at TMG flow rate of 100 sccm (S1), 84.3 sccm (S2), 59 sccm (S3) and 33.6 sccm (S4). All samples exhibit three main peaks located at 68.2° , 69° and 71.4° which correspond to crystal diffraction of m -plane $(30\bar{3}0)$ sapphire substrate, $(11\bar{2}2)$ GaN and $(11\bar{2}2)$ AlN, respectively. Additional peak at 67.8° which affiliates with $(20\bar{2}0)$ GaN plane is observed for high TMG flow rate samples of 100 sccm and 84.3 (S1 and S2).

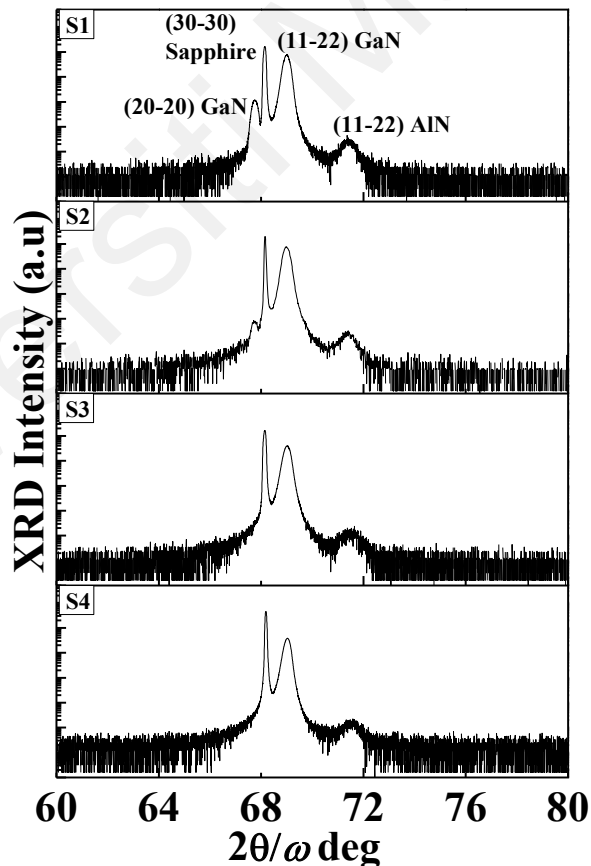


Figure 4.2: HR-XRD 2θ - ω scans of GaN grown on m -plane sapphire with AlN nucleation layer growth with TMA flow of 98.5 sccm from a higher flow rate (S1) to the lowest flow rate (S4).

The present of this additional peak implies that high flow rate produced a mixed phase of non-polar (20 $\bar{2}$ 0) and semi-polar (11 $\bar{2}$ 2) GaN. By lowering the flow rate, fully semi-polar (11 $\bar{2}$ 2) was obtained. This primary result denotes that the changes of flow rate significantly affect the crystallographic formation of the semi-polar GaN epitaxy. To further evaluate the crystal quality of the as-grown samples, on-axis and off-axis ω -scans were carried out.

4.1.2 On- and Off-axis XRC

Figure 4.3(a) shows the crystal quality of semi-polar (11 $\bar{2}$ 2) GaN evaluation performed via on-axis x-ray rocking curve (XRC) as a function of azimuthal angle (φ). The analysis was done over 360° range with an interval of 30° where 0° and 90° correspond to directions [$\bar{1}$ 123] and [1 $\bar{1}$ 00], respectively. *M*-shaped azimuthal FWHM values over 360°

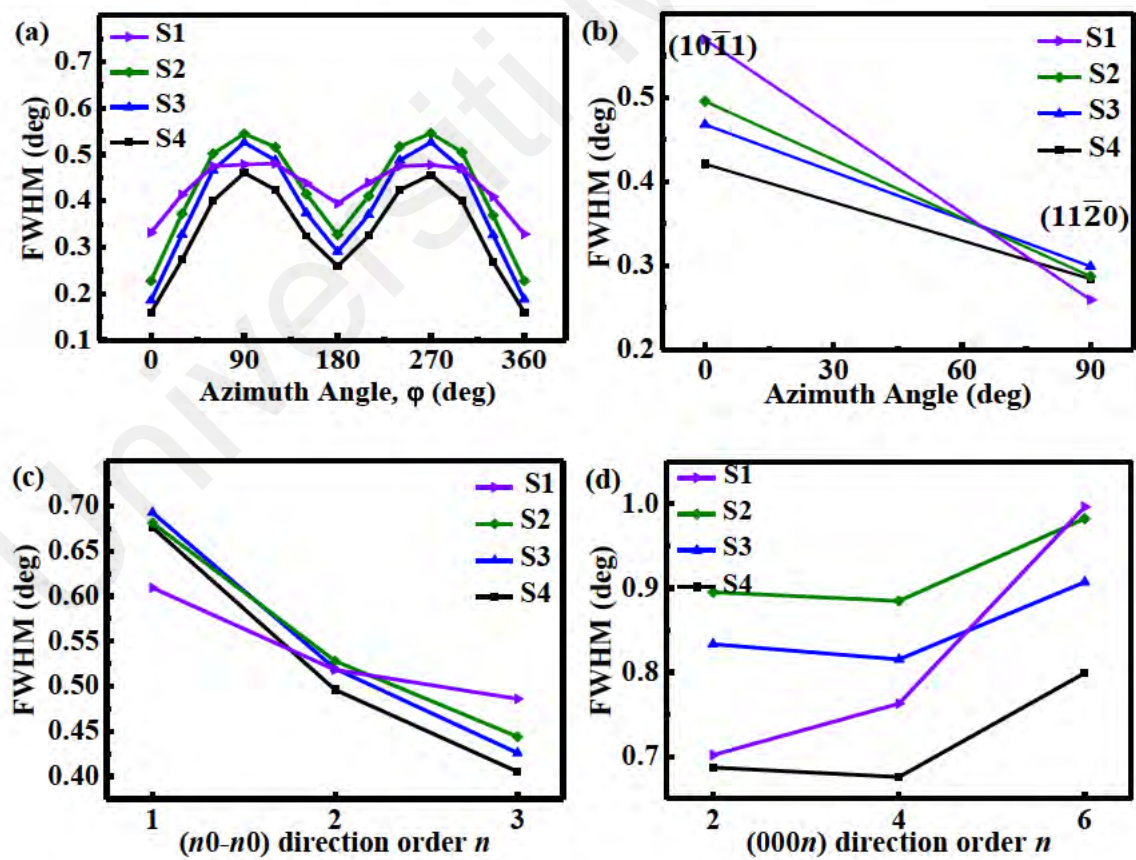


Figure 4.3: (a) On-axis XRC FWHM of GaN ω -scan as a function of azimuthal angle (φ) for sample S1, S2, S3 and S4. The off-axis XRC FWHM of all samples, (b) (10 $\bar{1}$ 1) and (11 $\bar{2}$ 0) diffraction planes, (c) ($n0\bar{n}0$) and (d) (000 n) diffraction planes.

angle are similar to the reported observations on (11 $\bar{2}2$) GaN (Jung et al., 2013; Kriouche et al., 2010; Omar et al., 2018; Zhao et al., 2016). It should be noted that the XRC FWHM for all samples along [1 $\bar{1}00$] is broader than [$\bar{1}\bar{1}23$] due to the strain arising from the different growth rates in *a*- and *c*-direction and lattice mismatch between (11 $\bar{2}2$) GaN and sapphire (Li et al., 2017). It is also due to the larger mosaic tilt and/or a reduced coherent length (smaller size of the mosaic blocks) (Kriouche et al., 2010). It is seen that a decrease in gas flow rate helps in improving the crystal quality hence narrowing the FWHMs of each azimuthal angle. For example, FWHM of sample S2 along [$\bar{1}\bar{1}23$] direction is 0.23° and [1 $\bar{1}00$] direction is 0.55° whereas for sample S4, FWHM along [$\bar{1}\bar{1}23$] direction is 0.16° and [1 $\bar{1}00$] direction is 0.46°. A reduction of 30.4% along [$\bar{1}\bar{1}23$] and 16.4% along [1 $\bar{1}00$], implies a reduction in dislocation densities and stacking faults. However, the results of sample S1 is anomalous and is neglected due to a very rough surface morphology as seen in FESEM Figure 4.5(a).

Off-axis XRC is implemented with different diffraction planes to further evaluate the crystal quality of (11 $\bar{2}2$) GaN. This is because for basal stacking faults (BSF), partial dislocations and perfect dislocations are present in epi-layers but are not visible under (11 $\bar{2}2$) diffraction under visibility criteria (Moram et al., 2009). Based on Figure 4.3(b), sample S4 has the lowest FWHM in (10 $\bar{1}1$) and (11 $\bar{2}0$) diffraction planes. These imply that there is a reduction in density of perfect dislocation with Burgers vector of $b = 1/3 \langle 11\bar{2}0 \rangle$ and prismatic stacking faults (PSFs) with displacement vector $R = \frac{1}{2}[10\bar{1}1]$, respectively as the flow rate was lowered (Vennéguès et al., 2007). A reduction in BSFs is expected since they can be terminated with partial dislocations or folded with the formation of PSF (Dasilva et al., 2010). Studies show that ($n0\bar{n}0$) planes at (10 $\bar{1}0$) and (20 $\bar{2}0$) are affected by BSF I_1 and I_2 , while (30 $\bar{3}0$) is not affected by either of the BSFs (McLaurin et al., 2008; Moram et al., 2009). BSFs I_1 is formed at the epitaxy

layer/substrate interface while I_2 originate from a slide in the basal plane by Shockley partial dislocations (Johnston et al., 2009).

On the other hand, $(000n)$ planes were responsible for partial dislocations and/or perfect dislocations with Burgers vectors having a c -axis component (Sun et al., 2009). Low FWHM values for sample S4 also indicate that the low gas flow rate can effectively enhance the crystal quality and reduced densities of BSF and dislocations, whereas for a high flow rate sample, high dislocations density was produced. To further understand the on-axis XRD in semi-polar $(11\bar{2}2)$ GaN, x-ray RSMs were carried out.

4.1.3 Reciprocal Space Maps (RSM)

Table 4.2: Diffuse scattering (DS) streaks and tilt value of sample S1 to S4 based on x-ray RSM.

<i>Sample</i>	<i>DS streak (nm^{-1})</i>	<i>Tilt (deg)</i>
<i>S1</i>	0.28	0.93
<i>S2</i>	0.32	0.70
<i>S3</i>	0.31	0.40
<i>S4</i>	0.27	0.29

Figure 4.4 illustrates the RSMs of $(11\bar{2}2)$ reflection along $[\bar{1}\bar{1}23]$ for all samples. Their corresponding diffuse scattering (DS) streaks and tilts are tabulated in Table 4.2. The presence of diffuse scattering streak in all RSM images can be correlated with the density of PSFs present in the sample (Lazarev et al., 2013). The contraction of DS streak is significantly influenced by gas flow rate, where lower gas flow rate assists in reducing PSFs except for S1. This might be due to the presence of large 3D islands, which will be explained further in the next section. The RSM results are also in line with the on-axis XRD results at $[1\bar{1}00]$ where ϕ at 90° is broadened by the existence of PSFs (Moram et al., 2009; Sun et al., 2009). Moreover, an offset in Q_x between substrate and epitaxy layer is observed in Figure 4.4, which indicates a tilt in the crystal lattice. It has been reported that epitaxial tilt is related to the formation of misfit dislocation at heterointerface for

partial strain relaxation (Tyagi et al., 2009). The tilt angle is observed to reduce as the gas flow rate was reduced, which implies that misfit dislocation in the sample was de-escalated at a low gas flow rate.

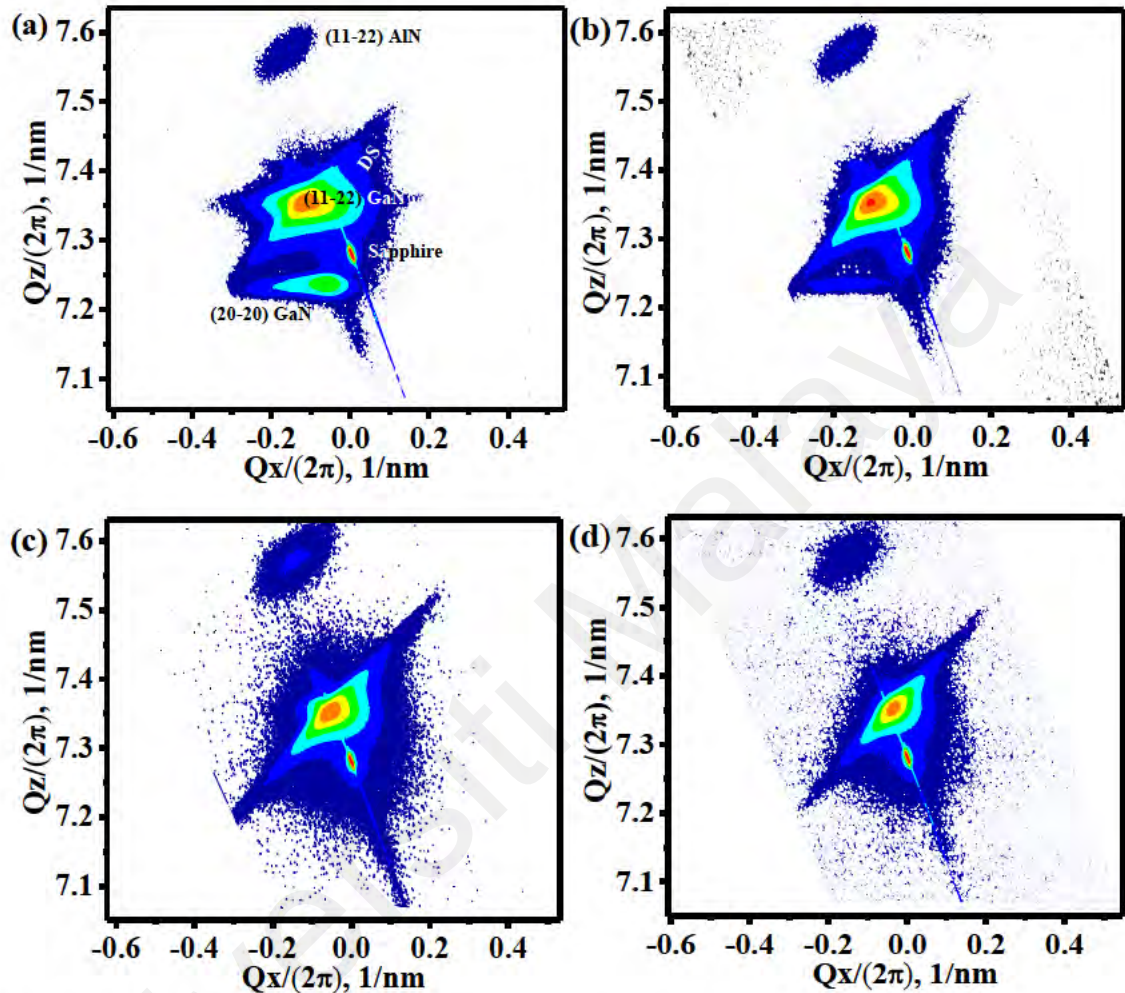


Figure 4.4: X-ray reciprocal space maps (RSM) of semi-polar $(11\bar{2}2)$ GaN on m -plane sapphire along $[11\bar{2}3]$ for (a) S1, (b) S2, (c) S3 and (d) S4.

4.1.4 FESEM

Figure 4.5 presents the surface morphology of all as-grown semi-polar GaN samples. Figure 4.5 (a) represents the highest TMG flow rate morphology, which consists of 3D islands of $(20\bar{2}0)$ (yellow circle) and $(11\bar{2}2)$ (red circle) GaN. This observation is consistent with the diffraction peaks found at 67.8° and 69° shown in Figure 4.2. On m -plane, two dominant planes are usually reported, namely $(11\bar{2}2)$ and $(10\bar{1}3)$ depending on experimental parameters adapted such as nitridation, nucleation layer, recrystallization

as well as buffer growth (Ploch et al., 2010). However, in this work, $(20\bar{2}0)$ plane is observed rather than $(10\bar{1}3)$ planes. This might be due to higher growth rate arise from higher gas flow rate causing the growth direction along $(11\bar{2}2)$ not fully suppressing the growth direction along $(20\bar{2}0)$. The formation of 3D islands can also be explained from the view of adatom mobility. The adatom mobility length gets smaller for larger growth rates, because the adatom movement is hindered by new materials arriving on the surface. The high flow rate might suppress the surface mobility, burying adatoms with new ones hence resulting in the observed 3D islands. A similar phenomenon is reported when the reactor pressure is increased as the reactor pressure has an indirect correlation with the gas flow rate (Oliver et al., 2005; Sun et al., 2009). An increase in gas flow rate may imply a change in the surface kinetics or thermodynamics and its strain.

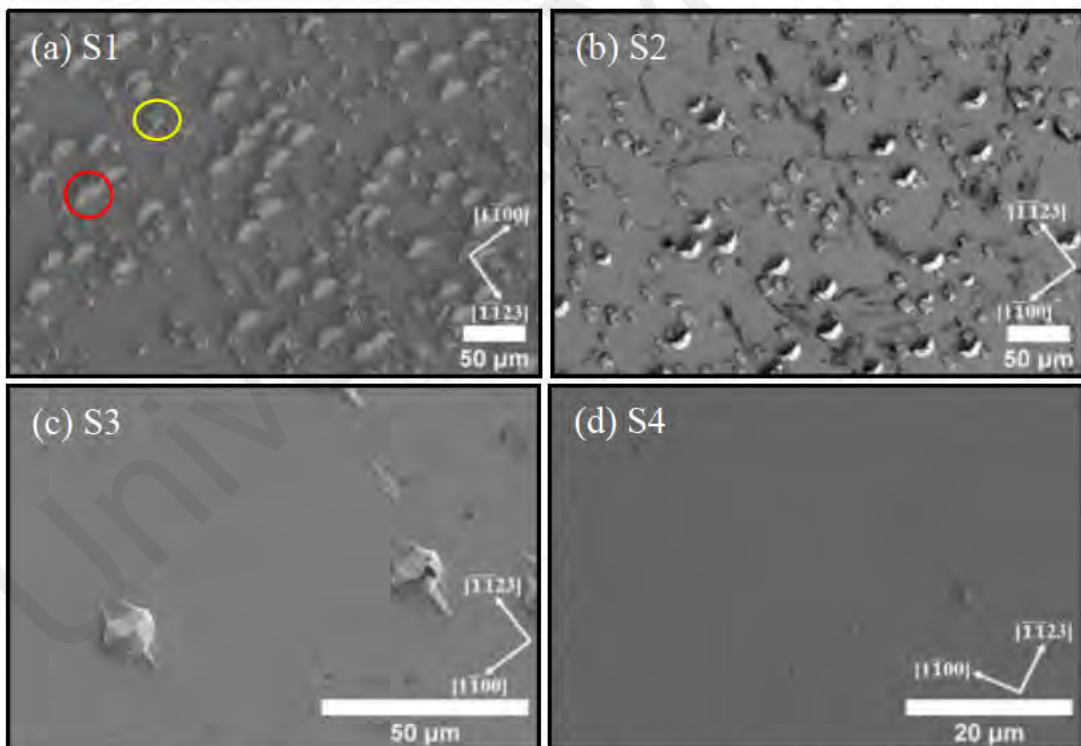


Figure 4.5: FESEM images of (a) S1, (b) S2, (c) S3 and (d) S4.

As the gas flow rate was lowered to 84.3 sccm (S2), less 3D islands were formed. Further reduction of the flow rate to 59 sccm (S3) lead to only $(11\bar{2}2)$ GaN islands. At the lowest flow rate of 33.6 sccm (S4), a flat surface with almost no 3D islands is observed.

This implies that the growth direction along $(11\bar{2}2)$ fully dominates over other directions which leads to the formation of single-crystalline GaN (Wernicke et al., 2011). The trend of the process observed in this work shows that the growth process follows a Volmer-Weber (VW) growth mode during the high gas flow rate, where the adatom interaction is much stronger than those adatoms on the surface, and as the flow rate was decreased and most of the islands have fully coalesced, the growth changes to Frank-van der Merve (FM) mode. FESEM observation thus far is consistent with the XRD results aforementioned, which can be used to explain the crystal phase formation.

Furthermore, the growth rates for the flat surface of sample S1 to S4 are 0.26 ± 0.01 , 0.22 ± 0.01 , 0.15 ± 0.006 and 0.08 ± 0.003 $\mu\text{m}/\text{min}$ respectively. The growth rate increase linearly with the increase in gas flow rate. However, the height of 3D islands measured from the flat surface for sample S1 reached 10.00 ± 0.05 μm with respect to its surface which is only 7.50 ± 0.04 μm , suggesting higher vertical growth over lateral growth which is further supported by cross-section images of sample S1 and S4 in Figure 4.6. As VW growth is expected in heteroepitaxy (Kehagias et al., 2005; Scheel, 2004), hence, islands were formed in the initial stages of epitaxy growth. Due to a higher vertical to lateral

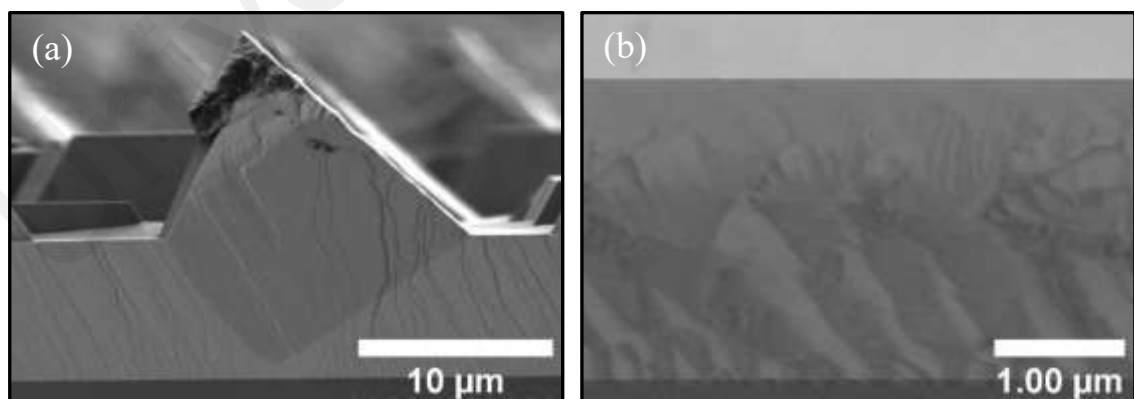


Figure 4.6: Cross-section fesem images of sample (a)S1 and (b) S4.

growth rate ratio, islands did not manage to coalesce in time and contribute to many un-coalesced 3D islands. Higher dislocation and tilt in sample S1 can also be explained as there is insufficient time for adatoms to fit themselves in an orderly arranged crystal

lattice through adsorption and desorption (Gao et al., 2009). As the flow rate decreases, adatom density also decreases, hence crystal lattice can be formed uniformly resulting in lower dislocation density and tilt. AFM measurement was carried out further to probe the effect of gas flow on the arrowhead structure.

4.1.5 Atomic force microscope (AFM)

Figure 4.7 (a)–(c) show the 5 x 5 μm AFM scan size for the different gas flow rates of sample S2 to S4. AFM scanning was done only at a flat surface to study the arrowhead

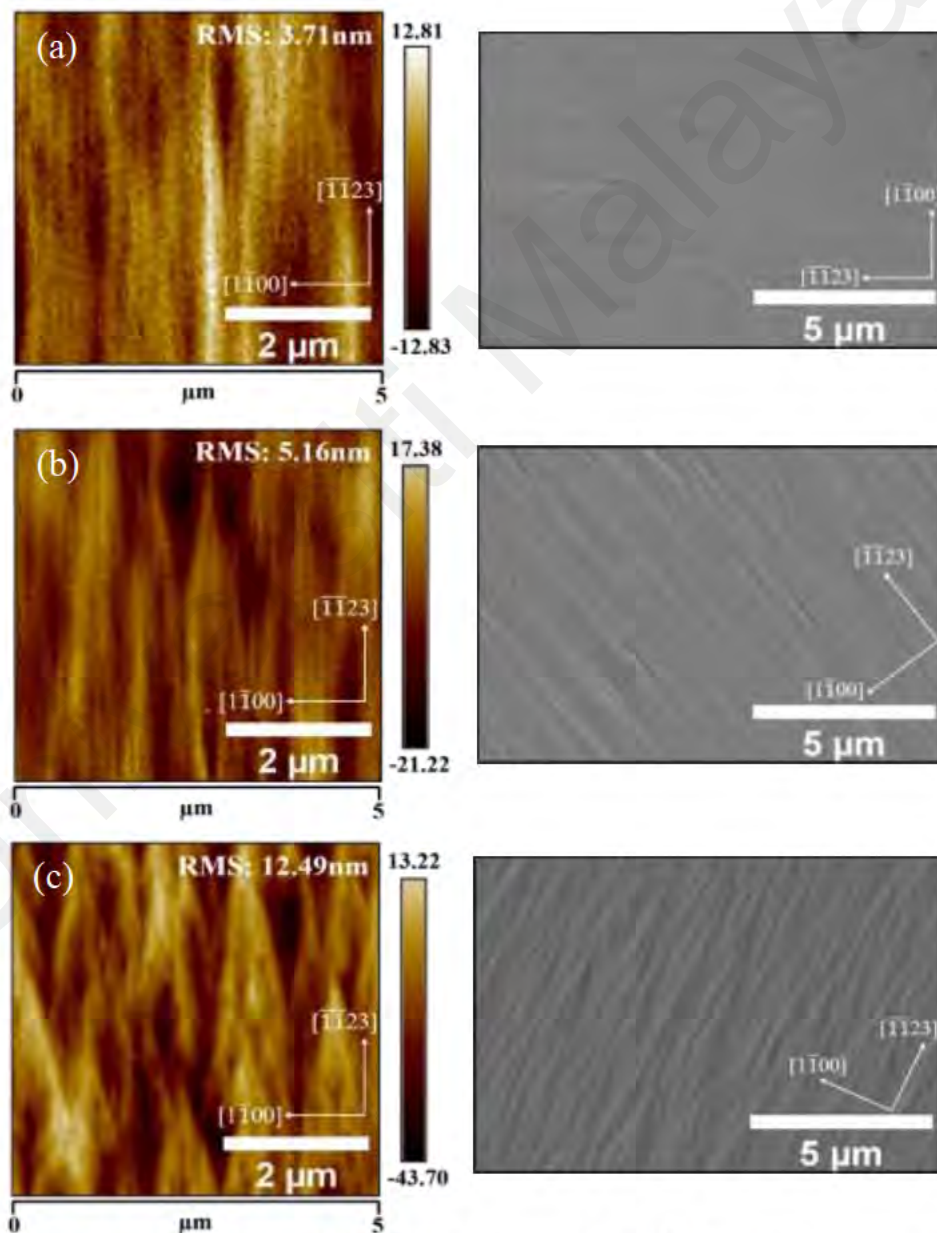


Figure 4.7: 5 x 5 μm AFM and FESEM micrograph of the flat surface area of (a) S2, (b) S3 and (c) S4.

feature of $(11\bar{2}2)$ GaN. Arrowhead like features are present on the sample surface and further support by their respective FESEM images. However, sample S1 cannot be measured due to insufficient flat surface area and the presence of big 3D islands, which may damage the cantilever. Based on the obtained results, the root mean square (RMS) roughness measured for flat surface of S2, S3, S4 is 3.71 ± 0.08 nm, 5.16 ± 0.1 nm and 12.49 ± 0.3 nm, respectively. The trend for AFM results is consistent with the FESEM images where the density/quantity of arrowhead-like feature on the sample S4 is greater than the other samples, hence a rougher surface obtained. These feature is a result of anisotropic surface diffusion which produce a less stable surface. Undulation is formed by adatom diffusion and its period is proportional to the diffusion length. For $(11\bar{2}2)$ surface, undulation with high spatial frequency is oriented along $[1\bar{1}00]$ which exhibits high diffusion barrier on $(11\bar{2}1)$ -type surface. For $(11\bar{2}2)$ surfaces, the 10-11 plane are tilted by 26° towards $[1\bar{1}00]$, therefore undulations along $[1\bar{1}00]$ are stabilized by the presence of $(10\bar{1}1)$ micro-facets (Wernicke & Kneissl, 2014).

The length of the anisotropic arrowhead-feature of the samples are found to be longer at higher gas flow rate. This condition can be correlated with higher growth rate adapted. Song *et.al* predicted that length of arrowhead surface structure can be increased by increasing the lateral growth rate, which can be achieved by reducing V/III ratio (Song et al., 2020). The lateral growth rate is normally correlated to the variation of the V/III ratio. When V/III ratio is varied, the atom kinetics at the surface is also affected. This atom kinetics is strongly influenced by the local stoichiometry at the vapor solid interface during the growth process (Gao et al., 2009). However, in this work where the V/III ratio is fixed, the variation of TMG and NH_3 flow rates appears to significantly affect the length of the arrowhead, which suggest that the lateral growth rate can be controlled by carrying of the gas flow. Higher elongation in $[\bar{1}\bar{1}23]$ direction observed in Figure 4.7 can be ascribed to the higher adatom diffusion length originated from higher growth rate at $[\bar{1}\bar{1}23]$

direction as compared to $[1\bar{1}00]$ direction (Ni et al., 2006). This is also due to a higher anisotropic diffusion barrier along the $[1\bar{1}00]$ on the semi-polar surface (Ploch et al., 2012). When growth rate is high, some of the arrowhead might be buried by new coming adatoms or coalesce with each other to form a larger arrowhead which helps explain the decrease in density/quantity of arrowhead when the gas flow rate is varied from low to high.

4.2 Variation of TMG gas flow on AlN growth with TMA flow of 50 sccm at a fixed V/III

4.2.1 Phase Analysis

Figure 4.8 shows the HR-XRD 2θ - ω scans for GaN grown on AlN nucleation layer at lower TMA flow rate with TMG flow rates of 100 sccm (SA1), 84.3 sccm (SA2), 59 sccm

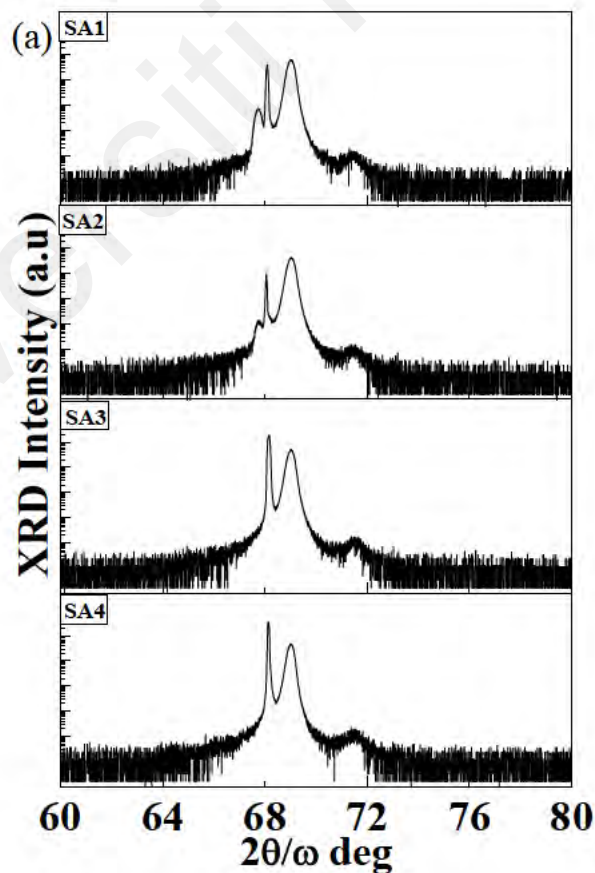


Figure 4.8: HR-XRD 2θ - ω scans of GaN grown on *m*-plane sapphire with AlN nucleation layer growth with TMA flow of 50 sccm from a higher flow rate (SA1) to the lowest flow rate (SA4).

(SA3) and 33.6 sccm (SA4). This series also shows similar diffraction peaks and pattern with the first series where the $(20\bar{2}0)$ GaN diffraction peak present in TMG flow rate of 100 sccm in SA1, the peak intensity reduces at flow rate of 84.3 sccm in SA2 and finally single crystalline semi-polar $(11\bar{2}2)$ GaN are formed at TMG flow rate of 59 sccm in SA3 and 33.6 sccm in SA4. The results are consistent with the first experimental series where the lower flow rate is preferred in producing single crystalline GaN.

4.2.2 On- and Off-axis XRC

The anisotropic properties of all the samples are characterized by performing on-axis XRC as a function of various azimuth angle (φ) as shown in Fig 4.9(a). As observed, the crystal quality improves as the gas flow rate decreases from SA1 to SA4 on the M -shaped

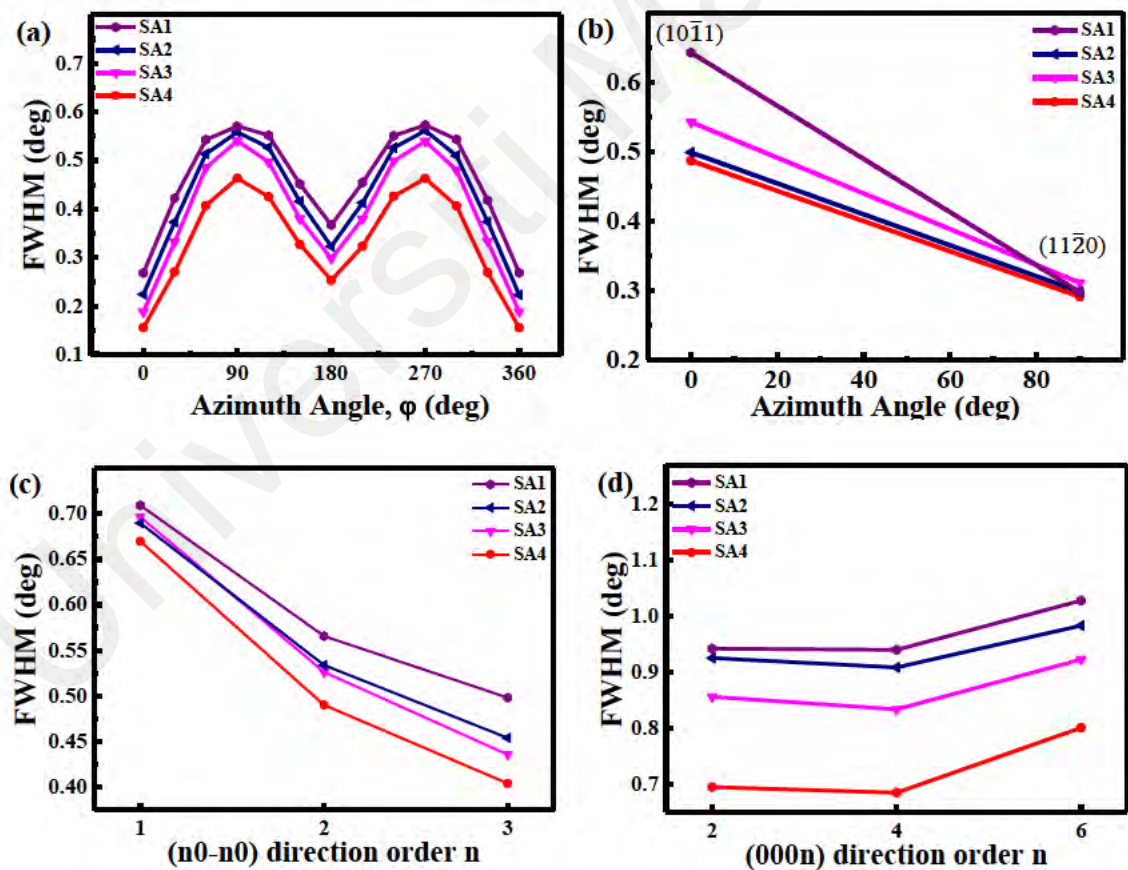


Figure 4.9: (a) On-axis XRC FWHM of GaN ω -scan as a function of azimuthal angle for sample SA1, SA2, SA3 and SA4. The off-axis XRC FWHM of sample SA1, SA2, SA3 and SA4, (b) $(10\bar{1}1)$ and $(11\bar{2}0)$ diffraction planes, (c) $(n0\bar{n}0)$ and (d) $(000n)$ diffraction planes.

FWHM azimuthal angle. The observation is consistent with the results from the first experimental series where the FWHM value on the $[1\bar{1}00]$ direction is broader than $[\bar{1}\bar{1}23]$ direction (Li et al., 2017). The decrement in FWHM values indicates the decrease of dislocation densities such as TDs, BSF and PSF. However, for the same TMG flow of 100 sccm, FWHM of sample SA1 is not anomalous and shows trend with other results in the same experimental series. At 0° , FWHM values improved by 44.4% from sample SA1 (0.27°) to SA4 (0.16°) whereas 90° shows an improvement of 19.3% for FWHM value of 0.57° (SA1) to 0.46° (SA4).

The off-axis XRC analysis is carried out on certain plane to determine their respective dislocations. Fig 4.9(b) shows that a decrease in perfect dislocation (PD) on $(10\bar{1}1)$ and PSF on $(11\bar{2}0)$ as the gas flow rate decrease. Based on the results, sample SA2 has less PD than SA3 and sample SA3 has highest PSF. This indicates that not all the BSFs are folded with the formation of PSFs for sample SA2 and SA1 or sample SA3 simply has a higher BSFs. Overall, sample SA4 has the least PD and PSF with FWHM value of 1764 arcsec and 2484 arcsec, respectively.

This is further supported by the results in Figure 4.9(c) where the $(10\bar{1}0)$ of SA3 is higher than SA2. Based on the $(n0\bar{n}0)$ results, sample SA4 is least affected by BSF with the FWHM values of 0.67° and 0.49° on $(10\bar{1}0)$ and $(20\bar{2}0)$, respectively (McLaurin et al., 2008). Figure 4.9(d) also shows that lower flow rates helped reduce partial/perfect dislocation (Sun et al., 2009). Sample SA4 shows an improvement of 23% in FWHM values compared to sample SA1 which has the highest gas flow rate in the $(000n)$ results.

In summary, all the on and off-axis analysis is in agreement with the first series where the lower gas flow rate enhance the crystal quality significantly. However for this experimental series, sample SA1 with highest TMG flow of 100 sccm did not show any

anomalous results compared with S1 in the first experimental series. This can be explained through FESEM analysis which will be shown in section 4.2.4.

4.2.3 Reciprocal Space Maps (RSM)

Figure 4.10 shows the RSM of semi-polar GaN reflected along $[\bar{1}\bar{1}23]$ direction for samples SA1 to SA4. Their respective DS streak and tilt are tabulated in Table 4.3. The reduction of DS streaks as the gas flow rate is lowered indicates lower density of PSFs

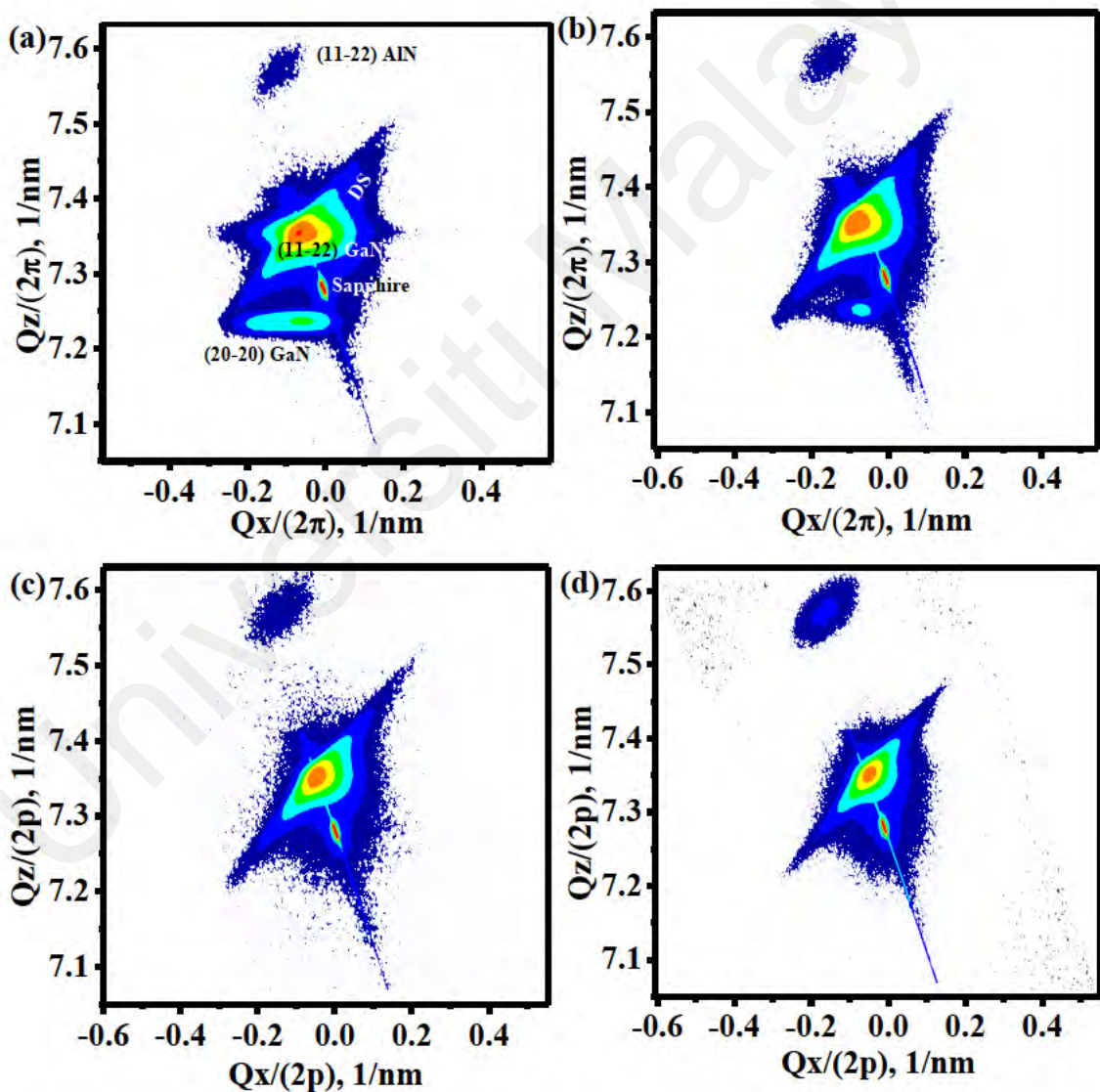


Figure 4.10: X-ray reciprocal space maps (RSM) of semi-polar (11 $\bar{2}2$) GaN on *m*-plane sapphire along $[\bar{1}\bar{1}23]$ for (a) SA1, (b) SA2, (c) SA3 and (d) SA4.

Table 4.3: Diffuse scattering (DS) streaks and tilt value of sample SA1 to SA4 based on x-ray RSM.

<i>Sample</i>	<i>DS streak (nm⁻¹)</i>	<i>Tilt (deg)</i>
SA1	0.30	0.55
SA2	0.32	0.61
SA3	0.29	0.42
SA4	0.24	0.30

generated since DS streak is correlated with PSFs. The result is also in line with the off-axis XRD result in Figure 4.9. (b) at $(11\bar{2}0)$ where the DS streak of SA1 is shorter than SA2. It is also observed that the tilt between semi-polar GaN epitaxial layer and m -plane substrate reduced when the gas flow rate is reduced, also implies that the misfit dislocation is reduced when going down the series (Makinudin et al., 2019). Smaller tilt in sample SA1 might be due to sample has been cut into smaller pieces before the measurement where the lattice stress and strain were affected.

4.2.4 FESEM

Figure 4.11 shows the FESEM images of all samples in this series. Figure 4.11(a) shows the surface of sample SA1 consists of 3D islands of $(20\bar{2}0)$ m -plane and $(11\bar{2}2)$ semi-polar GaN. The result is consistent with the phase analysis and similar to the first experimental series. This confirmed that although the growth condition for AlN nucleation layer varied, similar results are obtained. Hence, it can be concluded that effect of TMG gas flow variation at fixed V/III will brings out $(20\bar{2}0)$ m -plane GaN which are different than the usual results which produced $(10\bar{1}3)$ GaN (Omar et al., 2018). However, it can be observed that the 3D islands of sample SA1 have less 3D islands compared to sample S1 notably islands shape of $(11\bar{2}2)$ semi-polar GaN. Smoother surface may be the reason why the XRD results of sample SA1 is not anomalous as S1.

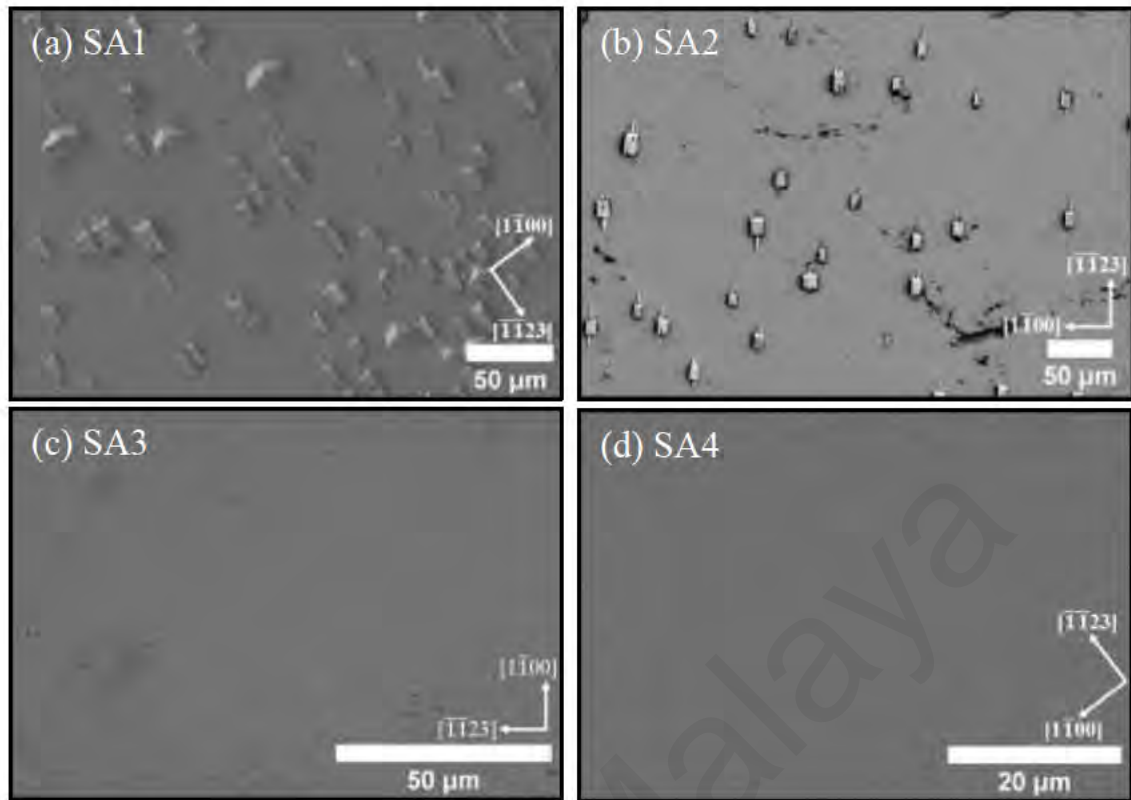


Figure 4.11: FESEM images of (a) SA1, (b) SA2, (c) SA3 and (d) SA4.

As the flow rate is reduced to 84.3 sccm, surface of SA2 show that no $(11\bar{2}2)$ semi-polar GaN islands are found, with only $(20\bar{2}0)$ *m*-plane GaN islands present. Further reduction of TMG gas flow rate to 50 and 33.6 sccm results in flat surface with no 3D island observed. The surface of SA3 also differed from S3 where no 3D $(11\bar{2}2)$ semi-polar GaN islands is observed whereas sample SA4 has similar surface morphology with sample S1. Similar transition from Volmer-Weber (VW) growth mode to Frank-van der Merve (FM) is observed when the gas flow rate is reduced from high to low. The FESEM observation thus agrees with the XRD analysis results which describe the GaN crystal plane orientation.

In addition, the growth rate for flat surface of sample SA1, SA2, SA3 and SA4 are 0.28 ± 0.01 , 0.24 ± 0.01 , 0.15 ± 0.006 and 0.06 ± 0.002 $\mu\text{m}/\text{min}$ respectively. The growth rate also increase linearly with the increase of gas flow rate. Figure 4.12(a) shows that most of the islands on sample SA1

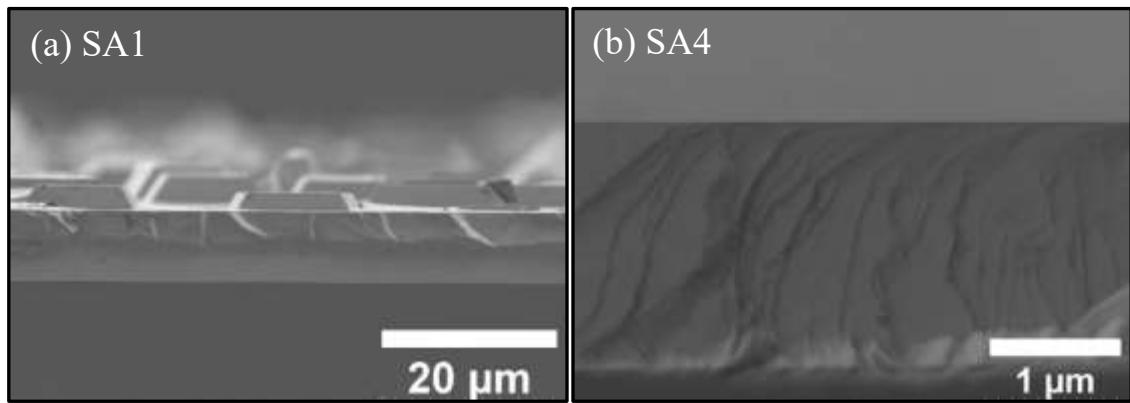


Figure 4.12: Cross-section feSEM images of sample (a)SA1 and (b) SA4.

are $(20\bar{2}0)$ *m*-plane GaN islands while $(11\bar{2}2)$ semi-polar GaN island is rarely seen whereas Figure 4.12(b) shows sample SA4 consisting of a flat surface. The islands are attributed to Volmer-Weber (VW) growth mode in initial stage of the growth, but the islands did not manage to coalesce in time as there is insufficient time for adatoms to arrange themselves.

4.2.5 Atomic force microscope (AFM)

Figure 4.13 (a) – (d) show the $5 \times 5 \mu\text{m}$ AFM scan size of all samples from highest to lowest flow rate along with their corresponding FESEM images. AFM is scanned only on the flat surface to study the arrowhead feature. Based on the results above, samples SA1, SA2, SA3 and SA4 have RMS roughness of $2.58 \pm 0.05 \text{ nm}$, $3.72 \pm 0.08 \text{ nm}$, $5.11 \pm 0.1 \text{ nm}$ and $10.31 \pm 0.2 \text{ nm}$ respectively. The RMS roughness agrees with the arrowhead concentration as rougher RMS value represents higher arrowhead concentration. As observed, samples with higher flow rate produces less arrowhead with lower surface roughness while lower flow rate produce more arrowhead with higher surface roughness. The elongation of arrowhead in $[\bar{1}\bar{1}23]$ direction can be explained from Ploch et al. (Ploch et al., 2012) calculation of anisotropic diffusion barrier at different direction as explained in the first experimental series. As the flow rate varies from low to high, reduction in quantity of arrowhead can be explained via growth rate. Higher growth rate will result in

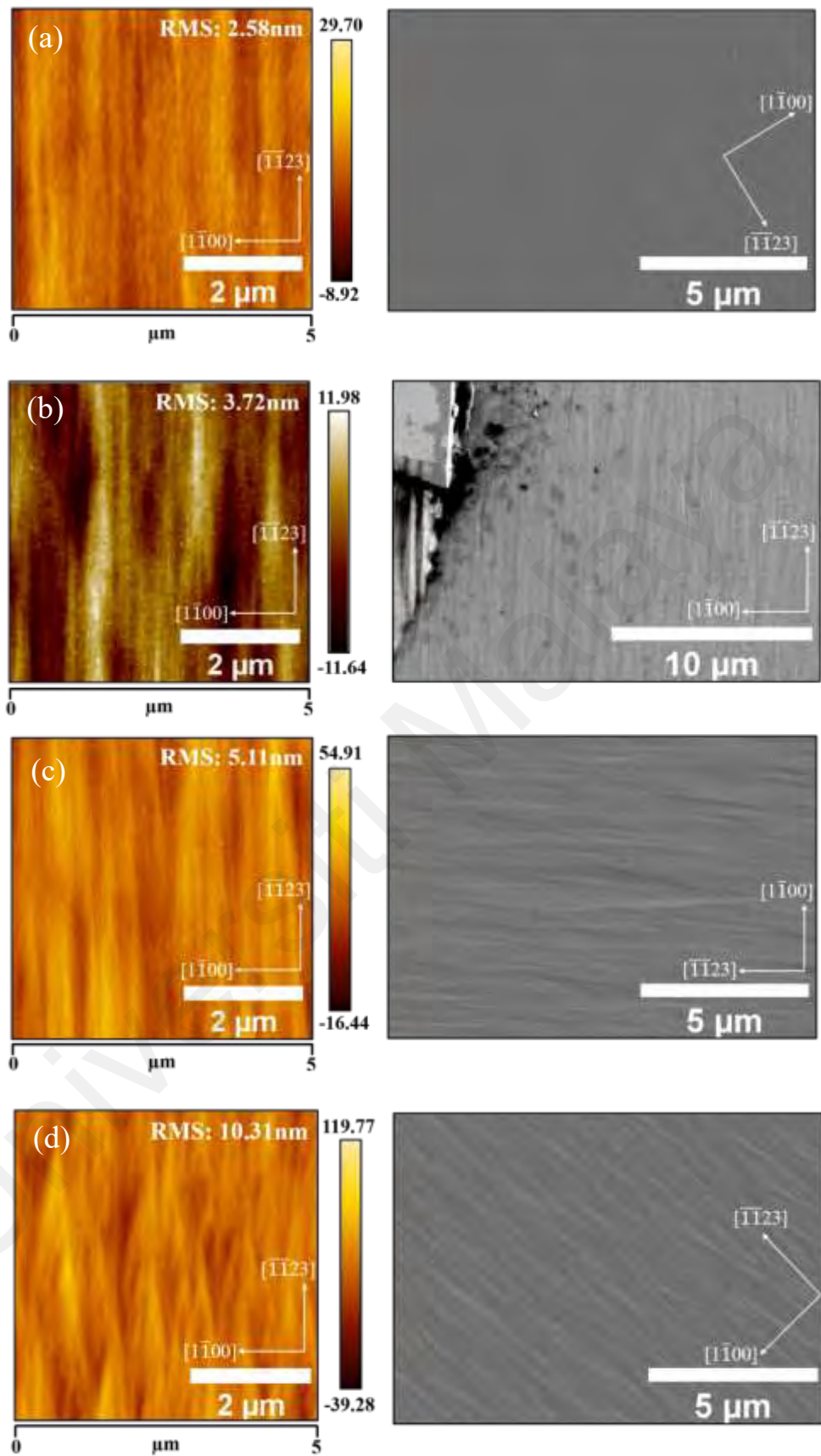


Figure 4.13: 5 x 5 μm AFM and FESEM micrograph of the flat surface area of (a) SA1, (b) SA2, (c) SA3 and (d) SA4.

coalescence of several arrowheads into a larger one or small arrowhead is buried by larger arrowhead which has caused the surface roughness to decrease.

The AFM results in this series is so far consistent with the first series where higher gas flow rate produce surface with less arrowheads and hence lower RMS roughness while lower gas flow rate produce surface with more arrowheads and higher RMS roughness. However, comparing to S1, the AFM for sample SA1 with same TMG flow of 100 sccm can be measured due to less 3D islands produced on the sample surface.

4.3 Discussion

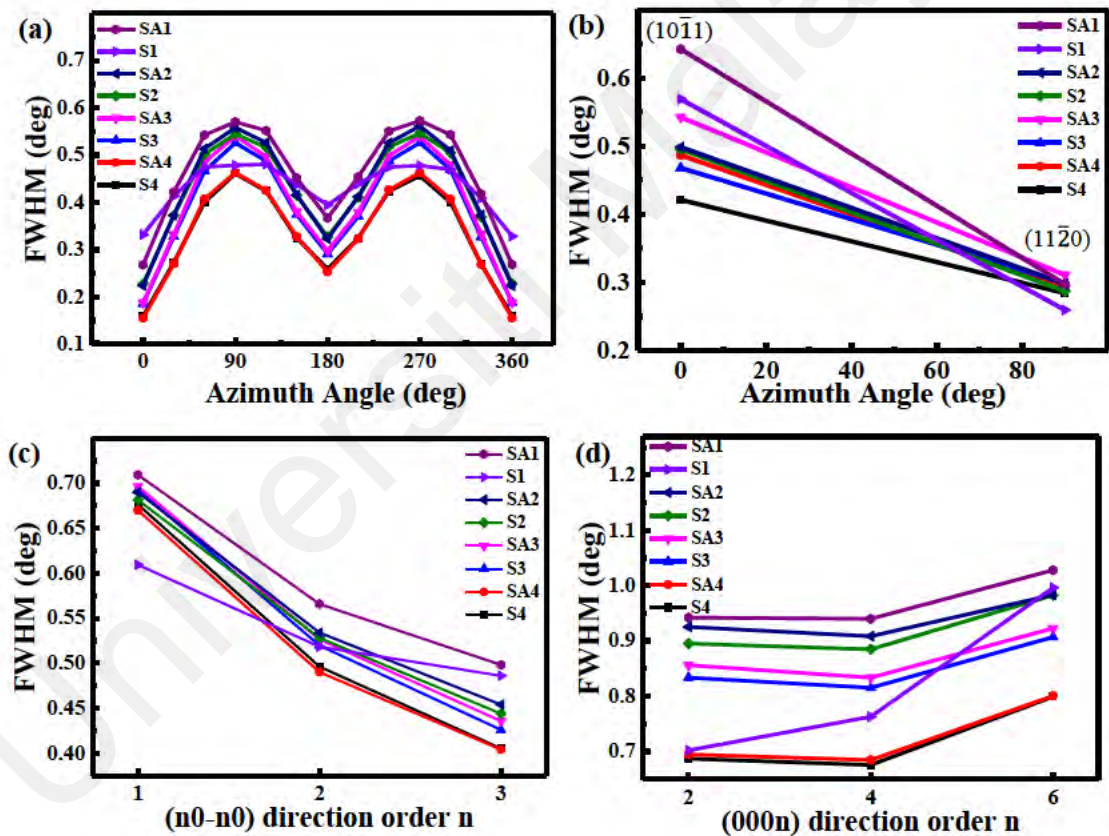


Figure 4.14: (a) On-axis XRC FWHM of GaN ω -scan as a function of azimuthal angle for all samples. The off-axis XRC FWHM of all samples, (b) $(10\bar{1}1)$ and $(11\bar{2}0)$ diffraction planes, (c) $(n0\bar{n}0)$ and (d) $(000n)$ diffraction planes.

Figure 4.14 shows the XRD results for all samples. Based on Figure 4.14(a), both experimental series showed that the lower the gas flow rate, the better the crystal quality.

However, there were no different in crystal quality for each of the TMG gas flow: 100 sccm, 84.3 sccm, 59 sccm and 33.6 sccm grown on different TMA gas flow nucleation layer. The off-axis XRC analysis from Figure 4.14(b) which is related to PD and PSF shows that PD can be reduced by lowering the TMA gas flow while Figure 4.14(c) which is sensitive to BSF and Figure 4.14(d) which is responsible for partial dislocation show not much difference when comparing both experimental series 1 and series 2 on each TMG gas flow rates (exclude sample S1). Hence, it can be concluded that the change in TMA gas flow nucleation layer has minimum effect on the crystal quality of $(11\bar{2}2)$ semi-polar GaN epitaxial layer grown.

Based on the FESEM results in Figure 4.5 and Figure 4.11, in the first and second experimental series respectively, there are some noticeable differences. There are less 3D islands found on AlN nucleation layer grown at lower TMA gas flow as compared to the higher one. When the TMG gas flow is lowered to 84.3 sccm, sample SA2 shows that $(11\bar{2}2)$ semi-polar GaN 3D islands are completely suppressed and only $(20\bar{2}0)$ *m*-plane 3D islands are found. The phenomenon might be explained from the $(11\bar{2}2)$ semi-polar GaN 3D islands present in Figure 4.15.

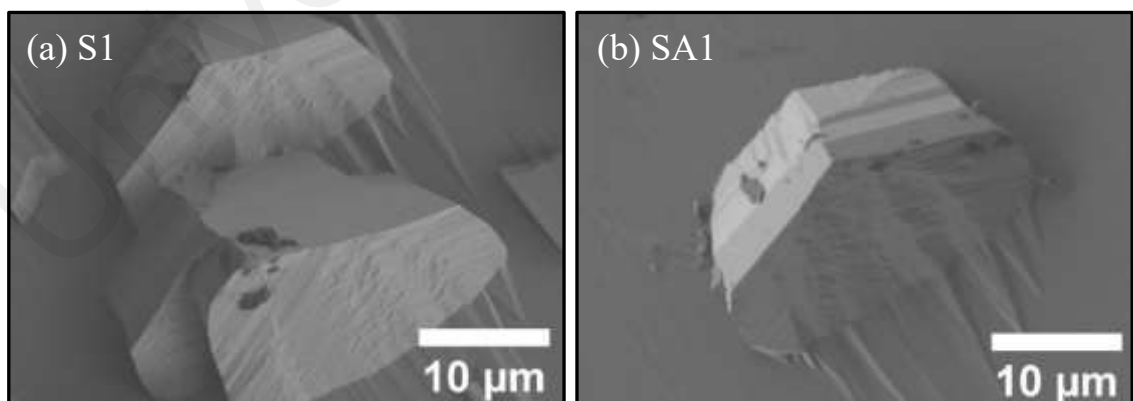


Figure 4.15: FESEM images of $(11\bar{2}2)$ semi-polar GaN islands growth at TMG flow of 100 sccm for (a) S1 and (b) SA1.

As shown in Figure 4.15(a), the 3D islands in sample S1 did not show any sign of coalescence while in Figure 4.15(b), the 3D islands in sample SA1 shows that the

coalescence process has already started. It can be observed that there are stacks of pentagonal planes formed on the c -facet of $(11\bar{2}2)$ semi-polar GaN 3D islands as a process to coalesce the 3D island where similar process will be shown in schematic diagram of Figure 4.16 below. The full coalescence process can also be viewed from the transformation of $(11\bar{2}2)$ semi-polar GaN 3D islands in the first experimental series when TMG gas flow varies from 100 sccm to 59 sccm which will be further discuss in Figure 4.16. From here, it can be summarized that nucleation layer grown with lower TMA flow rate helps in reducing the $(11\bar{2}2)$ semi-polar GaN 3D islands and have better coalescence than nucleation layer grown with higher TMA flow rate.

Figure 4.16(a) shows 3D islands of $(11\bar{2}2)$ GaN formed on sample S1 with a schematic diagram on the inset. At a high gas flow rate, 3D islands did not manage to coalesce. As the rate was reduced, coalescence started to occur. The islands coalesced with the formation of pentagonal planes on the c -facet of $(11\bar{2}2)$ GaN as shown in Figure 4.16(b) (most obvious highlighted in the white circle). The pentagonal planes continue to form and elongate along $[\bar{1}\bar{1}23]$ direction. This condition is explained as the adatom activation energy along $[\bar{1}\bar{1}23]$ being lower than $[1\bar{1}00]$ (Fang et al., 2008; Ploch et al., 2012), indicating the adatom diffusion along $[\bar{1}\bar{1}23]$ is more favorable. Similar case was reported on non-polar $(11\bar{2}0)$ GaN where activation energy along $[0001]$ and $[1\bar{1}00]$ are 0.21 and 0.93 eV respectively (Lymperakis & Neugebauer, 2009). Similar coalescence mechanism from non-polar GaN has also been reported (Sun et al., 2008). The islands coalescence can be further interpreted or speculated from the gradual formation of arrowhead as observed in Figure 4.17.

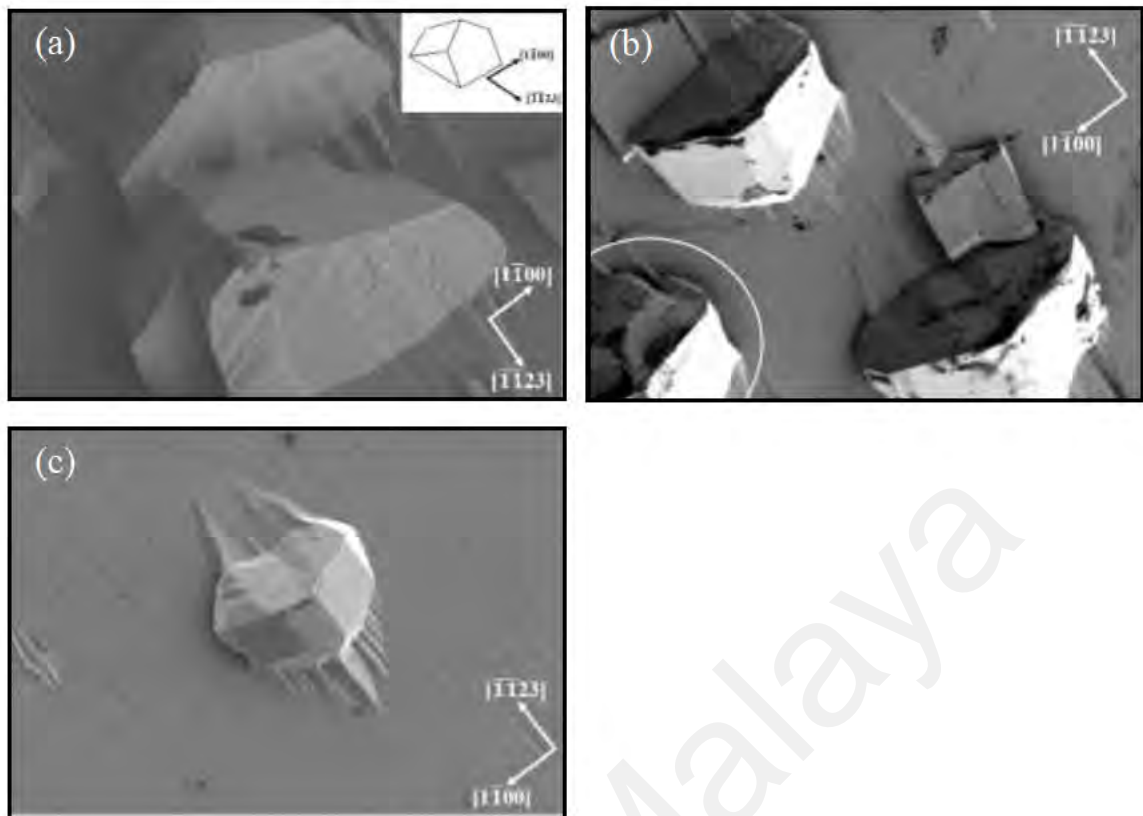


Figure 4.16: FESEM image of 3D islands on the sample (a) S1, (b) S2 and (c) S3.

Figure 4.17 depicts a progression of arrowhead which outset from $(11\bar{2}2)$ GaN micro-facets. Initially, pentagonal planes formed on the c-facet of the $(11\bar{2}2)$ GaN. Then, the planes slowly elongated in $[\bar{1}123]$ direction, which later formed the arrowheads. Based on Ploch et al. calculation, the adatom activation energy along $[\bar{1}123]$ and $[1\bar{1}00]$ are 0.8 and 1.3 eV respectively due to the surface atomic atom spacing of 3.04 Å along $[\bar{1}123]$ and 5.52 Å along $[1\bar{1}00]$ (Ploch et al., 2012). From geometrical aspect, the diffusion length along $[1\bar{1}00]$ might be geometrically limited by the width of the first pentagonal planes (indicated by blue arrow) formed on the c-facet of $(11\bar{2}2)$ GaN and the width of micro-facet itself (indicated by green arrow). It is prudent to say that, the behavior of arrowhead growth is depending on the size of initial $(11\bar{2}2)$ GaN micro-facets.

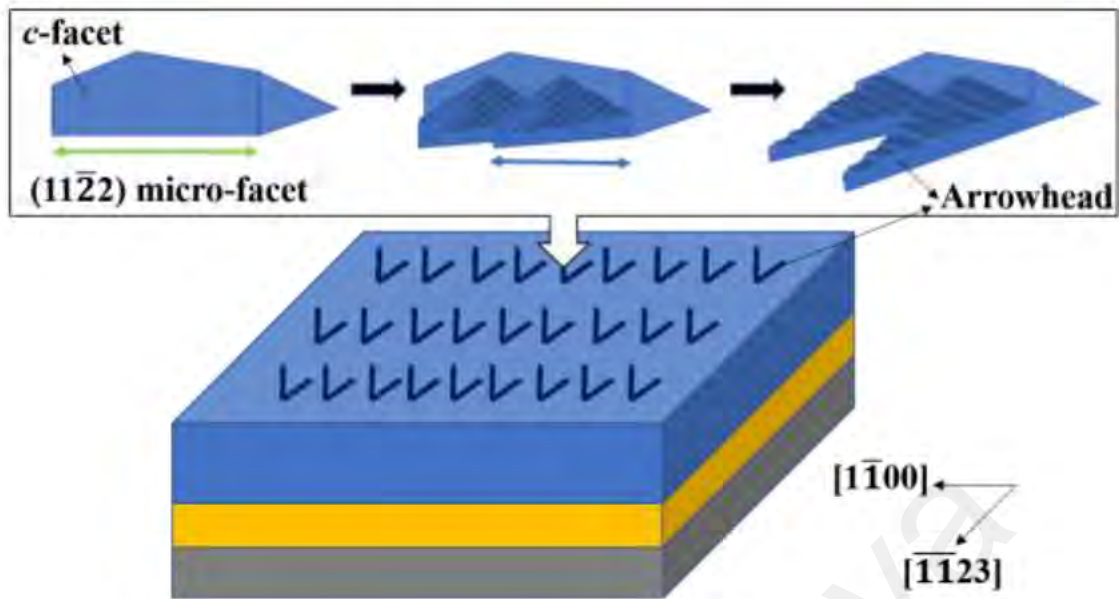


Figure 4.17: Illustration of semi-polar GaN surface coalescence towards the formation of an arrowhead.

Besides that, there is also little difference in term of growth rate for flat surface of the two experimental series. The growth rate of both series is tabulated in Table 4.4.

Table 4.4: Growth rate for both series.

TMG flow rate	GaN flat layer growth rate of the first series ($\mu\text{m}/\text{min}$)	GaN flat layer growth rate of the second series ($\mu\text{m}/\text{min}$)
100 sccm	0.26 ± 0.01	0.28 ± 0.01
84.3 sccm	0.22 ± 0.01	0.24 ± 0.01
59 sccm	0.15 ± 0.006	0.15 ± 0.006
33.6 sccm	0.08 ± 0.003	0.06 ± 0.002

The growth rate for each of the series increase linearly with the increase of TMG flow rate. The difference at higher TMG flow rate is due to more adatoms used to produce 3D islands than the flat surface in the first series, which is more than in the second series. Hence, the first experimental series with more 3D island has a lower flat surface growth rate than the second experimental series. However, at the lowest flow rate, the first experimental series has a higher growth rate than the second series. This might be due to a change in the thermodynamics properties due to different TMA flow rate adapted on the AlN nucleation layer though the actual explanations is yet to be confirmed.

Finally, the flat surface roughness of the two series is compared. The values of surface roughness in term of RMS are tabulated in Table 4.5.

Table 4.5: Flat surface roughness (RMS value) for both series.

TMG flow rate	GaN flat layer surface roughness of first series (nm)	GaN flat layer surface roughness of second series (nm)
100 sccm	nil	2.58 ±0.05
84.3 sccm	3.71 ±0.08	3.72 ±0.08
59 sccm	5.16 ±0.1	5.11 ±0.1
33.6 sccm	12.49 ±0.3	10.31 ±0.2

The surface roughness of GaN flat surface decreases as the TMG flow rate increases for both of the series. This might be due to coalescence of several arrowheads into one as the growth rate increases which has been explained above. Although several TMA flow rate were adapted on the AlN nucleation layer, the RMS roughness of flat GaN epitaxial surface for each TMG flow rate of 100 sccm, 84.3 sccm, 59 sccm and 33.6 sccm is almost similar. Hence, there is no difference in term of surface roughness on the flat surface with different growth condition of AlN nucleation layer.

The increase in surface roughness of GaN flat surface is attributed to larger arrowhead size formed when comparing different TMG flow rate at same GaN layer thickness as in (Ooi et al., 2022). Larger arrowhead indicates a longer undulation period along $[\bar{1}1\bar{2}3]$ and $[1\bar{1}00]$ directions which can be related to the adatom surface diffusion relation:

$$L \sim \sqrt{D\tau} \quad (4.1)$$

where L is the diffusion length, τ is the adatom lifetime on the surface and D is the diffusion constant. The only affecting factor left is τ since other parameters is fixed. At lower flow rate, growth rate is also low and there are less incoming adatoms to the surface causing surface adatoms have a higher τ . Hence, the diffusion length is longer which lead

to longer undulation period and larger arrowhead formed. While at higher flow rate, the effect is vice versa.

4.4 Summary

The effect of TMG gas flow on GaN epitaxial layer and the effect of TMA gas flow on AlN nucleation layer have been discussed in this chapter. The mechanism for the formation of arrowhead has been proposed. Furthermore, the surface roughening due to lower flow rate is also well explained using relation $L \sim \sqrt{D\tau}$. It is found out that the optimum gas flow rate is sample SA3 when considering both aspects of crystal quality and surface roughness. Hence, sample SA3 will be used in chapter 5 to investigate the effect of pressure on GaN epitaxial layer.

CHAPTER 5: THE EFFECT OF PRESSURE ON SEMI-POLAR (11 $\bar{2}$ 2) GAN EPITAXIAL LAYER

In this work, the effect of pressure on semi-polar (11 $\bar{2}$ 2) gallium nitride epitaxial layer on *m*-plane sapphire substrate is studied. Sample SA3 was selected from the previous experimental series and the respective gas flow rate is utilized to grow semi-polar (11 $\bar{2}$ 2) GaN epitaxial layer at varied reactor pressure of 40kPa, 70kPa and 100kPa. All samples are characterized by HRXRD inclusive of 2θ - ω scan, x-ray rocking curve (XRC) measurement and reciprocal space maps (RSM) to study the anisotropy and crystallinity. Additionally, AFM measurement is used to study the impact of GaN growth pressure on the surface morphology. The results are then compared to sample SA3 which is grown at the pressure of 13.3kPa. The name of all samples with their respective parameters is shown in the table below where sample SA3 is renamed as P1 in this experimental series. The schematic diagram of the sample in this experiment is also depicted in Figure 5.1.

Table 5.1: Pressure adapted in this experiment.

PRESSURE (KPA)	SAMPLE
13.3	P1
40	P2
70	P3
100	P4

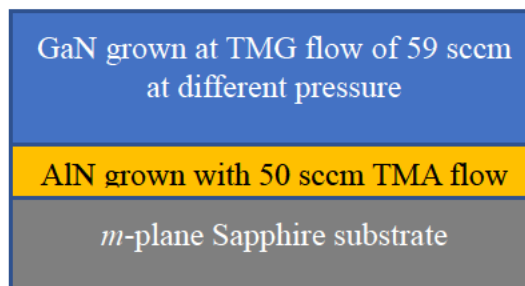


Figure 5.1: Schematic diagram for this experiment.

5.1 Phase Analysis

2θ - ω scans are carried out to study the effect of GaN epilayer grown at several pressures. The results of HR-XRD 2θ - ω scans for GaN grown at pressure of 13.3 kPa (S1), 40 kPa (S2), 70 kPa (S3) and 100 kPa (S4) are shown in Figure 5.2. All samples have the same peaks at 68.2° , 69° and 71.4° which represents the diffraction of m -plane $(30\bar{3}0)$ sapphire substrate, $(11\bar{2}2)$ GaN and $(11\bar{2}2)$ AlN, respectively. All samples display a single crystalline $(11\bar{2}2)$ GaN and there is no polycrystalline found in this experiment implying that pressure did not affect the crystallographic phase of the semi-polar GaN epitaxy.

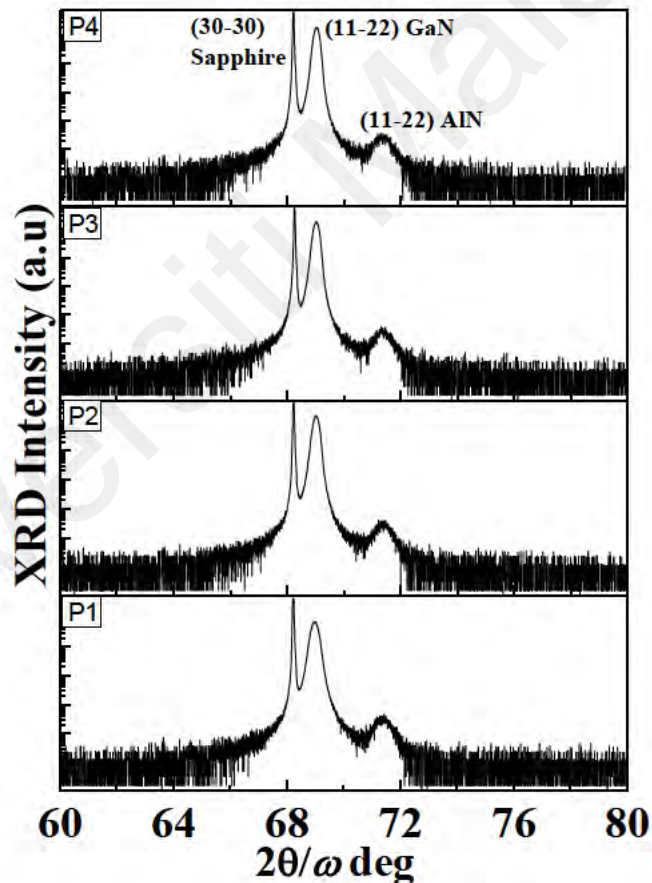


Figure 5.2: HR-XRD 2θ - ω scans of GaN grown on m -plane sapphire with AlN nucleation layer growth with pressure from 13.3 kPa (P1) to 100 kPa (P4).

5.2 On- and Off-axis XRC

Figure 5.3. (a) depicts the on-axis XRC measurements as a function of azimuth angle (φ) from 0° to 360° carried out to study the anisotropic of the GaN samples. The result is thus far consistent with the other results of $(11\bar{2}2)$ GaN where the FWHM on the $[1\bar{1}00]$ direction at $\varphi = 90^\circ$ is broader than $[\bar{1}123]$ direction at $\varphi = 0^\circ$ and hence *M*-shaped FWHM value results is obtained (Kriouche et al., 2010). As observed, the FWHM values shrink as the pressure increases from 13.3 kPa to 100 kPa from sample P1 to P4. For example, by comparing sample P1 and P4, FWHM values reduced by 38.9% along $[\bar{1}123]$ direction and 54.7% along $[1\bar{1}00]$ direction indicating that the decrease of dislocation density and

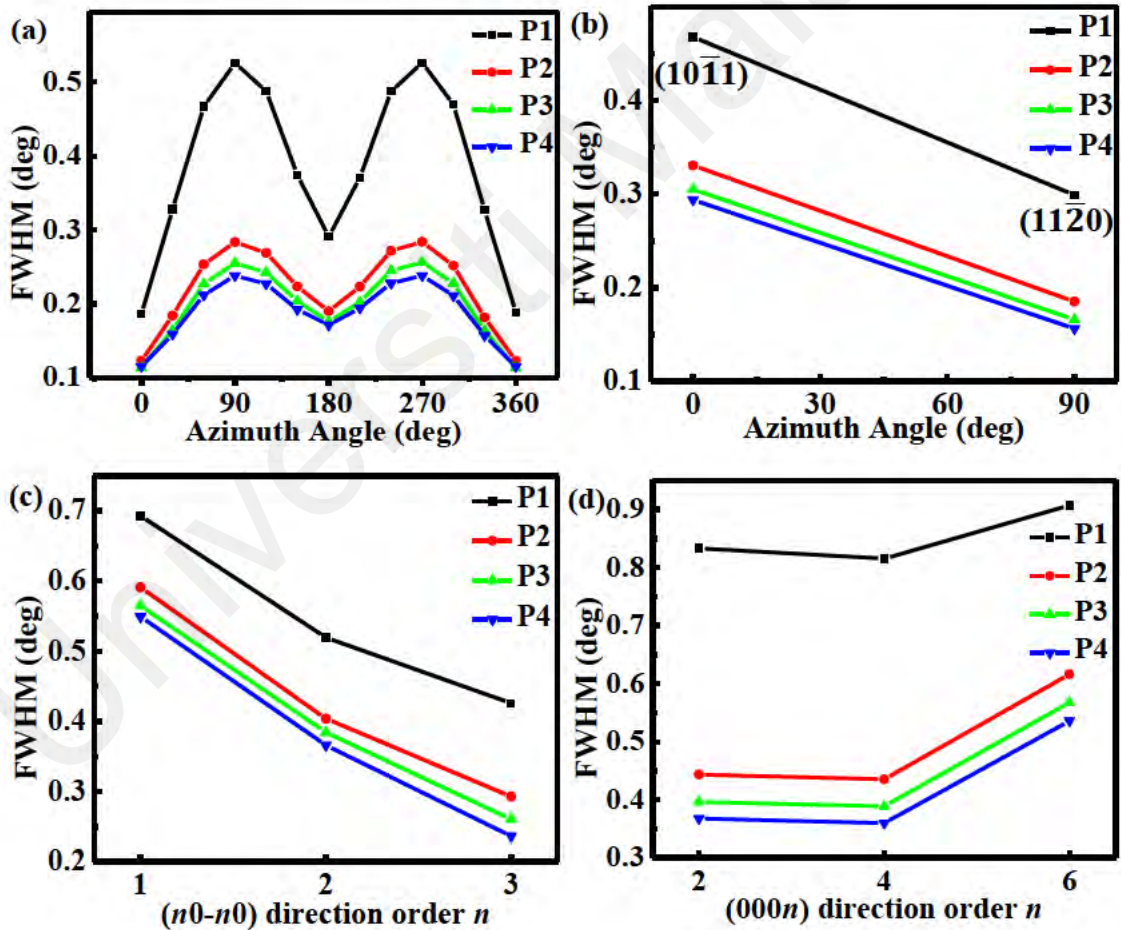


Figure 5.3: (a) On-axis XRC FWHM of GaN ω -scan as a function of azimuthal angle for sample P1, P2, P3 and P4. The off-axis XRC FWHM of sample P1, P2, P3 and P4, (b) $(10\bar{1}1)$ and $(11\bar{2}0)$ diffraction planes, (c) $(n0\bar{n}0)$ and (d) $(000n)$ diffraction planes.

improvement in the quality of the crystal.

On the off-axis XRC scans, Figure 5.3. (b) shows that sample P4 has the lowest FWHM in both $(10\bar{1}1)$ and $(11\bar{2}0)$ diffraction planes implying reduction in perfect dislocation and prismatic stacking fault, respectively, as the pressure is increased. The $(n0\bar{n}0)$ result also consistently shows a decrease in BSF as the pressure increased and it should be noted that $n=3$ is insensitive to BSF (Moram et al., 2009). Finally, the $(000n)$ result proves that increase in pressure will significantly improve the crystal quality as the partial dislocations and/or perfect dislocations decrease.

All the XRC results are consistent, showing that the increase in pressure has significantly reduced the dislocations and enhanced the crystal quality. The results are agreeable with the report by Sun et al. (Sun et al., 2009) which stated that the increase in pressure improved crystal quality. He has also speculated that the pressure helps to bend the dislocations at an inclined growth direction and annihilate with each other (Ni et al., 2007). Whereas Wu et al. (Wu et al., 2016) reported that the increase in pressure helps in the formation of islands. When the growth continues, the $+c$ regions growth will bury the BSFs that usually appear at the $-c$ regions. The mechanism is shown in Figure 5.4 below.

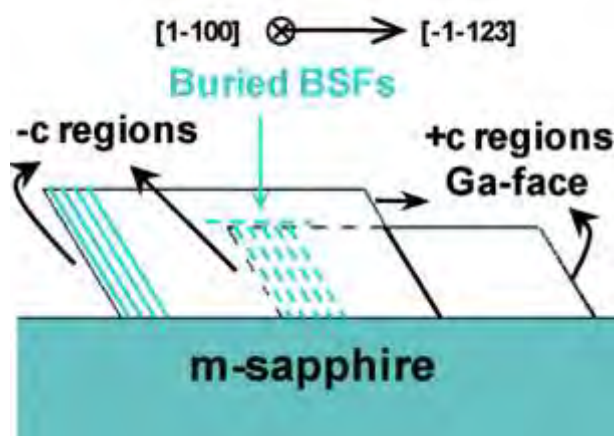


Figure 5.4: Growth mechanism proposed by Wu et al. (Wu et al., 2016), obtained from CrystEngComm.

5.3 Reciprocal Space Maps (RSM)

Figure 5.5 presents the RSM of all $(11\bar{2}2)$ GaN samples reflected along $[\bar{1}123]$, with their respective DS streak and tilt tabulated in Table 5.2. As observed, the DS streak narrowed down as the pressure increases from P1 to P4 elucidating the decrease of prismatic stacking fault which is consistent with the results shown in Figure 5.3. (b). The misfit dislocation also decreases as the tilt between GaN layer and substrate reduces when the pressure increases (Young et al., 2010). The tilt was calculated from the offset in Q_x of the epitaxial layer and substrate.

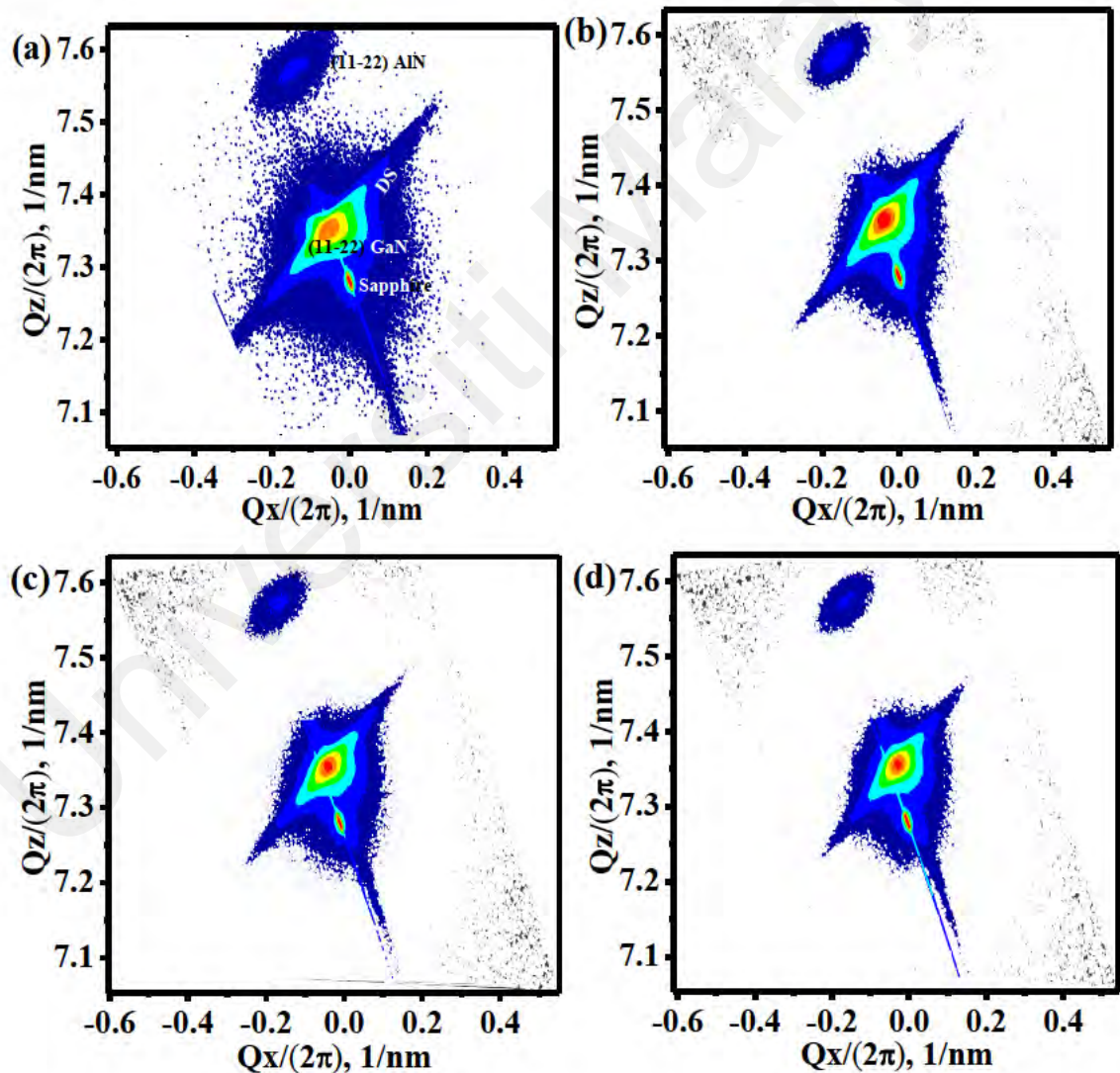


Figure 5.5: X-ray reciprocal space maps (RSM) of semi-polar $(11\bar{2}2)$ GaN on m -plane sapphire along $[\bar{1}123]$ for (a) P1, (b) P2, (c) P3 and (d) P4.

Table 5.2: Diffuse scattering (DS) streaks and tilt value of sample SA1 to SA4 based on x-ray RSM.

<i>Sample</i>	<i>DS streak (nm^{-1})</i>	<i>Tilt (deg)</i>
<i>P1</i>	0.29	0.42
<i>P2</i>	0.29	0.28
<i>P3</i>	0.25	0.25
<i>P4</i>	0.23	0.18

5.4 Atomic force microscope (AFM)

Figure 5.6 shows the 25 x 25 μm AFM images for all samples from P1 to P4. The results is consistent with the other semi-polar GaN surface as arrowhead like features with longer undulation along $[\bar{1}\bar{1}23]$ are detected. Based on the results, the RMS roughness of

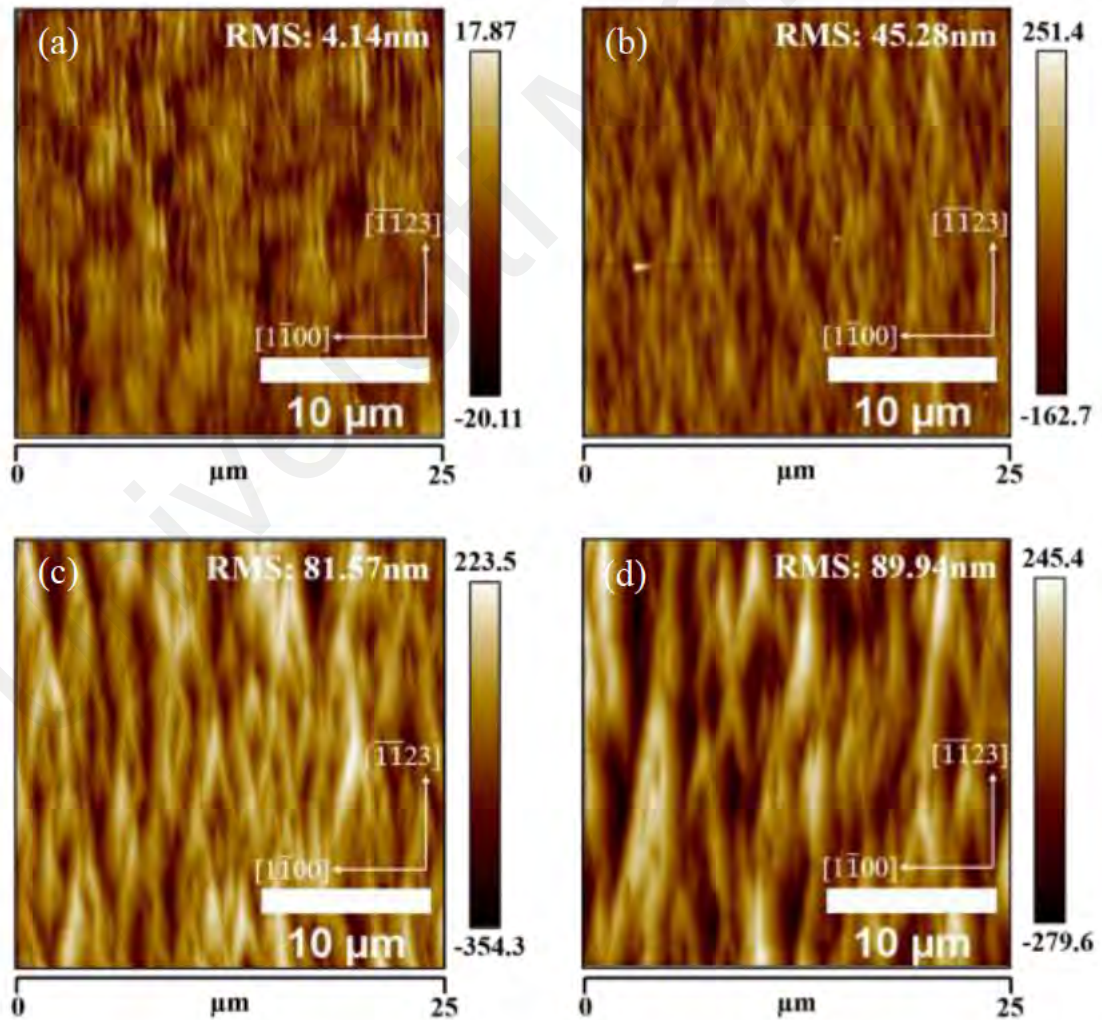


Figure 5.6: 25 x 25 μm AFM images of the flat surface area of (a) P1, (b) P2, (c) P3 and (d) P4.

the sample increased from 4.14 ± 0.09 nm to 89.94 ± 2 nm from sample P1 to P4 indicating the roughening of the sample as the pressure rises. The arrowhead is also becoming larger and wider along $[1\bar{1}00]$ direction indicating the increase in the grain size of $(11\bar{2}2)$ GaN as the pressure rises. Similar observation has been reported by (Ploch et al., 2012) where the increase in the arrowhead size is attributed to the increase in the undulation length. The increase in the undulation length as the pressure increases is partially due to the increase in surface temperature (Hoffmann et al., 2011) and reduction in the growth rate (Daudin & Widmann, 1997). Similar explanation in Chapter 4 on reduction in growth rate causing surface roughening can also be applied here. Besides that, higher pressure will cause NH_3 to decompose more. This will increase the surface V/III ratio and cause the surface to be more N-rich which lead to surface roughening (Leung et al., 2012).

Hence, it can be concluded that the grain size of the sample surface become larger when the growth pressure increases which leads to 3D growth mode. At 3D growth mode, the grains have larger surface, so dislocations can be easily bend out of the crystal. This agrees with what has been reported by Sun et al. (Sun et al., 2009) which stated that the increase in pressure will decrease the dislocations, as bigger grain size will help to bend the dislocations in other direction and force them to dissociate or be annihilate.

5.5 Summary

The effect of pressure has been presented in this chapter. It is found out that the increase in pressure will reduce the dislocations but will lead to 3D growth and cause surface roughening.

CHAPTER 6: CONCLUSION AND FUTURE WORK

The importance and problems in semi-polar GaN have been discussed in this dissertation. So far, the effect of gas flow rate variation at fixed V/III ratio have not been discussed. Thus, the effects of gas flow rate variation at fixed V/III ratio and growth pressure are presented in this research.

While varying the gas flow rate of TMG and ammonia at V/III ratio of 118, it was found that the lowest TMG flow rate of 33.6 sccm produces the best GaN crystal quality while the highest TMG flow rate of 100 sccm produces the worst GaN crystal quality. 3D islands were also produced for GaN grown at higher TMG gas flow rate of 59, 83.6 and 100 sccm. However, AFM scan on the flat surface showed that the lower TMG flow rate has a rougher surface and vice versa for the higher TMG flow rate. As the experiment is repeated with AlN nucleation layer grown with lower TMA flow rate of 50 sccm, the XRD and AFM shows results with the similar trend. However, it is found that the samples in this experimental series have less 3D islands and GaN epitaxial layer grown with TMG gas flow of 59 and 33.6 sccm show no 3D islands. Finally, it can be concluded that lowering the TMG flow rate can enhance the crystal quality with lowest FWHM value of 576 and 1656 arcsecs at $[\bar{1}\bar{1}23]$ and $[1\bar{1}00]$, respectively. While lowering the TMA flow rate can reduce the formation of 3D islands and help flatten the GaN surface. The mechanism for the formation of arrowhead from the transformation of 3D islands coalescence while varying the gas flow from high to low has been proposed in this work. Most importantly, the surface roughening mechanism at lower growth rate is well explained using the adatom surface diffusion relation $L \sim \sqrt{D\tau}$.

From the results of pressure variation, it can be concluded that at high pressure produced higher crystal quality GaN epitaxial layer with rougher surface morphology and bigger grain size which lead to 3D growth. The results also agreed with findings reported

by Sun et al. and Wu et al. which concluded that high pressure helps reduce the dislocations. Similar explanation mechanism proposed in gas flow variation series for the surface roughening can also be applied in this series.

In the future, TMG and TMA flow rate adapted from this experiment can be utilized to produce high crystal quality GaN without 3D islands while high pressure growth needs to be optimized or combine with other growth methods such as AlN or SiN_x interlayer to obtain GaN with high crystal quality and low surface roughness.

Universiti Malaya

REFERENCES

- Ahmad Makinudin, A. H., Omar, A. Z., Anuar, A., Bakar, A. S. A., Denbaars, S. P., & Supangat, A. (2019). Impact of a strained periodic multilayer on the surface and crystal quality of a semipolar (11-22) GaN template. *Crystal Growth and Design*, 19(11), 6092–6099.
- Akasaki, I., & Amano, H. (1997). Crystal growth and conductivity control of group III nitride semiconductors and their application to short wavelength light emitters. *Japanese Journal of Applied Physics, Part 1: Regular Papers & Short Notes & Review Papers*, 36(9 A), 5393–5408.
- Almond, M. J., Drew, M. G. B., Jenkins, C. E., & Rice, D. A. (1992). Organometallic precursors for the formation of GaN by metal-organic chemical vapour deposition: A study of $[(\text{CH}_3)_2\text{GaNH}_2]_3$. *Journal of the Chemical Society, Dalton Transactions*, 1, 5–9.
- Amano, H., Sawaki, N., Akasaki, I., & Toyoda, Y. (1986). Metalorganic vapor phase epitaxial growth of a high quality GaN film using an AlN buffer layer. *Applied Physics Letters*, 48(5), 353–355.
- Arroyo Rojas Dasilva, Y., Zhu, T., Martin, D., Grandjean, N., & Stadelmann, P. (2008). Characterization of a-plane GaN films grown on r-plane sapphire substrate by electron microscopy. In *EMC 2008 14th European Microscopy Congress 1–5 September 2008, Aachen, Germany* (pp. 637–638). Springer Berlin Heidelberg.
- Bernardini, F., Fiorentini, V., & Vanderbilt, D. (1997). Spontaneous polarization and piezoelectric constants of III-V nitrides. *Physical Review B - Condensed Matter and Materials Physics*, 56(16), R10024–R10027.
- Brasser, C., Bruckbauer, J., Gong, Y., Jiu, L., Bai, J., Warzecha, M., Edwards, P. R., Wang, T., & Martin, R. W. (2018). Cathodoluminescence studies of chevron features in semi-polar (11 $\bar{2}$ 2) InGaN/GaN multiple quantum well structures. *Journal of Applied Physics*, 123(17), Article#174502.
- Dasilva, Y. A.-R., Ruterana, P., Lahourcade, L., Monroy, E., & Nataf, G. (2010). Extended defects in semipolar (1122) gallium nitride. *Gallium Nitride Materials and Devices V*, 7602, Article#76020G.
- Dasilva, Y. A. R., Chauvat, M. P., Ruterana, P., Lahourcade, L., Monroy, E., & Nataf, G. (2010). Defect structure in heteroepitaxial semipolar (1122) (Ga, Al)N. *Journal of Physics Condensed Matter*, 22(35), Article#355802.
- Daudin, B., & Widmann, F. (1997). Layer-by-layer growth of AlN and GaN by molecular beam epitaxy. *Journal of Crystal Growth*, 182(1–2), 1–5.
- Deguchi, T., Sekiguchi, K., Nakamura, A., Sota, T., Matsuo, R., Chichibu, S., & Nakamura, S. (1999). Quantum-confined stark effect in an AlGaIn/GaN/AlGaIn single quantum well structure. *Japanese Journal of Applied Physics, Part 2: Letters*, 38(8 B), Article#L914.
- Ehrlich, G., & Hudda, F. G. (1966). Atomic view of surface self-diffusion: Tungsten on tungsten. *The Journal of Chemical Physics*, 44(3), 1039–1049.
- Ernst, F., & Pirouz, P. (1989). The formation mechanism of planar defects in compound semiconductors grown epitaxially on {100} silicon substrates. *Journal of Materials Research*, 4(4), 834–842.

- Fadhil, O. A. (2019). *Crystal quality enhancement of semi-polar (11-22) InGaN/GaN-based LED grown on m-plane sapphire substrate via MOCVD*. (Doctoral dissertation, Universiti Malaya). Retrieved on 10 September 2021 from <http://studentsrepo.um.edu.my/11628>
- Fang, H., Yang, Z. J., Wang, Y., Dai, T., Sang, L. W., Zhao, L. B., Yu, T. J., & Zhang, G. Y. (2008). Analysis of mass transport mechanism in InGaN epitaxy on ridge shaped selective area growth GaN by metal organic chemical vapor deposition. *Journal of Applied Physics*, *103*(1), Article#014908.
- Farrell, R. M., Haeger, D. A., Chen, X., Gallinat, C. S., Davis, R. W., Cornish, M., Fujito, K., Keller, S., Denbaars, S. P., Nakamura, S., & Speck, J. S. (2010). Origin of pyramidal hillocks on GaN thin films grown on free-standing m-plane GaN substrates. *Applied Physics Letters*, *96*(23), Article#231907.
- Fiorentini, V., Bernardini, F., Sala, F. Della, Di Carlo, A., & Lugli, P. (1999). Effects of macroscopic polarization in III-V nitride multiple quantum wells. *Physical Review B - Condensed Matter and Materials Physics*, *60*(12), 8849–8858.
- Gao, Z., Hao, Y., Li, P., & Zhang, J. (2009). Role of lateral growth on the structural properties of high temperature GaN layer. *Science in China, Series E: Technological Sciences*, *52*(5), 1242–1247.
- Gil, B. (1998). *Group III Nitride Semiconductor Compounds - Oxford University Press*. (n.d.). Retrieved May 25, 2021, from <https://global.oup.com/academic/product/group-iii-nitride-semiconductor-compounds-9780198501596?cc=us&lang=en&>
- Grinys, T., Drunga, T., Badokas, K., Dargis, R., Clark, A., & Malinauskas, T. (2017). Growth conditions of semi and non-polar GaN on Si with Er₂O₃ buffer layer. *Journal of Alloys and Compounds*, *725*, 739–743.
- Han, Y., Caliebe, M., Kappers, M., Scholz, F., Pristovsek, M., & Humphreys, C. (2015). Origin of faceted surface hillocks on semi-polar (11 $\bar{2}$ 2) GaN templates grown on pre-structured sapphire. *Journal of Crystal Growth*, *415*, 170–175.
- Hoffmann, V., Knauer, A., Brunner, C., Einfeldt, S., Weyers, M., Trnkle, G., Haberland, K., Zettler, J. T., & Kneissl, M. (2011). Uniformity of the wafer surface temperature during MOVPE growth of GaN-based laser diode structures on GaN and sapphire substrate. *Journal of Crystal Growth*, *315*(1), 5–9.
- Holt, D. B., & Yacobi, B. G. (2007). Extended defects in semiconductors: Electronic properties, device effects and structures. *Extended Defects in Semiconductors: Electronic Properties, Device Effects and Structures* (Vol. 9780521819343). Cambridge University Press.
- Jacko, M. G., & Price, S. J. W. (1963). The pyrolysis of trimethyl gallium. *Canadian Journal of Chemistry*, *41*(6), 1560–1567.
- Johnson, W. C., Parson, J. B., & Crew, M. C. (1932). Nitrogen compounds of gallium. III. *The Journal of Physical Chemistry*, *36*(10), 2651–2654.
- Johnston, C. F., Moram, M. A., Kappers, M. J., & Humphreys, C. J. (2009). Defect reduction in (11 2- 2) semipolar GaN grown on m -plane sapphire using ScN interlayers. *Applied Physics Letters*, *94*(16), Article#161109.
- Jung, C., Jang, J., Hwang, J., Jeong, J., Kim, J., Lee, K., & Nam, O. (2013). Defect reduction in (11-22) semipolar GaN with embedded InN islands on m-plane sapphire.

- Kehagias, T., Delimitis, A., Komninou, P., Iliopoulos, E., Dimakis, E., Georgakilas, A., & Nouet, G. (2005). Misfit accommodation of compact and columnar InN epilayers grown on Ga-face GaN (0001) by molecular-beam epitaxy. *Applied Physics Letters*, 86(15), 1–3.
- Khan, M. A., Van Hove, J. M., Kuznia, J. N., & Olson, D. T. (1991). High electron mobility GaN/Al_xGa_{1-x}N heterostructures grown by low-pressure metalorganic chemical vapor deposition. *Applied Physics Letters*, 58(21), 2408–2410.
- Kim, M. H., Schubert, M. F., Dai, Q., Kim, J. K., Schubert, E. F., Piprek, J., & Park, Y. (2007). Origin of efficiency droop in GaN-based light-emitting diodes. *Applied Physics Letters*, 91(18), Article#183507.
- Kioupakis, E., Rinke, P., Delaney, K. T., & Van De Walle, C. G. (2011). Indirect Auger recombination as a cause of efficiency droop in nitride light-emitting diodes. *Applied Physics Letters*, 98(16), Article#161107.
- Kneissl, M., & Wernicke, T. (2014). Optical and structural properties of InGaN light-emitters on non-polar and semipolar GaN. *III-Nitride Semiconductors and Their Modern Devices*, 244–288.
- Komninou, P., Kioseoglou, J., Dimitrakopoulos, G. P., Kehagias, T., & Karakostas, T. (2005). Partial dislocations in wurtzite GaN. *Physica Status Solidi (A) Applications and Materials Science*, 202(15), 2888–2899.
- Koukitu, A., Takahashi, N., Taki, T., & Seki, H. (1996). Thermodynamic analysis of In_xGa_{1-x}N alloy composition grown by metalorganic vapor phase epitaxy. *Japanese Journal of Applied Physics, Part 2: Letters*, 35(6 A), Article#L673.
- Koukitu, Akinori, Takahashi, N., & Seki, H. (1997). Thermodynamic study on metalorganic vapor-phase epitaxial growth of group III nitrides. *Japanese Journal of Applied Physics, Part 2: Letters*, 36(9 A/B), Article#L1136.
- Kriouche, N., Venéguès, P., Nemoz, M., Nataf, G., & De Mierry, P. (2010). Stacking faults blocking process in (1 1 -2 2) semipolar GaN growth on sapphire using asymmetric lateral epitaxy. *Journal of Crystal Growth*, 312(19), 2625–2630.
- Larsen, C. A., Buchan, N. I., Li, S. H., & Stringfellow, G. B. (1990). Decomposition mechanisms of trimethylgallium. *Journal of Crystal Growth*, 102(1–2), 103–116.
- Lazarev, S., Bauer, S., Meisch, T., Bauer, M., Tischer, I., Barchuk, M., Thonke, K., Holy, V., Scholz, F., & Baumbach, T. (2013). Three-dimensional reciprocal space mapping of diffuse scattering for the study of stacking faults in semipolar (11 $\bar{2}$) GaN layers grown from the sidewall of an r-patterned sapphire substrate. *Journal of Applied Crystallography*, 46(5), 1425–1433.
- Leung, B., Sun, Q., Yerino, C. D., Han, J., & Coltrin, M. E. (2012). Using the kinetic Wulff plot to design and control nonpolar and semipolar GaN heteroepitaxy. *Semiconductor Science and Technology*, 27(2), Article#024005.
- Li, Z., Jiu, L., Gong, Y., Wang, L., Zhang, Y., Bai, J., & Wang, T. (2017). Semi-polar (11-22) AlGa_N on overgrown GaN on micro-rod templates: Simultaneous management of crystal quality improvement and cracking issue. *Applied Physics Letters*, 110(8), Article#082103.
- Ling, S. C., Lu, T. C., Chang, S. P., Chen, J. R., Kuo, H. C., & Wang, S. C. (2010). Low

- efficiency droop in blue-green m-plane InGaN/GaN light emitting diodes. *Applied Physics Letters*, 96(23), Article#231101.
- Liu, J. M., Zhang, J., Lin, W. Y., Ye, M. X., Feng, X. X., Zhang, D. Y., Steve, D., Xu, C. K., & Liu, B. L. (2015). Effect of pressure on the semipolar GaN (10-11) growth mode on patterned Si substrates. *Chinese Physics B*, 24(5), Article#057801.
- Lowndes, D. H., Zheng, X. Y., Zhu, S., Budai, J. D., & Warmack, R. J. (1992). Suppression of the spiral-growth mechanism in epitaxial YBa₂Cu₃O_{7-x} films grown on miscut substrates. *Applied Physics Letters*, 61(7), 852–854.
- Lymperakis, L., & Neugebauer, J. (2009). Large anisotropic adatom kinetics on nonpolar GaN surfaces: Consequences for surface morphologies and nanowire growth. *Physical Review B - Condensed Matter and Materials Physics*, 79(24), Article#241308.
- Manasevit, H. M. (1972). The use of metalorganics in the preparation of semiconductor materials: Growth on insulating substrates. *Journal of Crystal Growth*, 13–14(C), 306–314.
- Manasevit, H. M., Erdmann, F. M., & Simpson, W. I. (1971). The Use of Metalorganics in the Preparation of Semiconductor Materials. *Journal of The Electrochemical Society*, 118(11), Article#1864.
- Martin, G., Botchkarev, A., Rockett, A., & Morkoç, H. (1995). Valence-band discontinuities of wurtzite GaN, AlN, and InN heterojunctions measured by x-ray photoemission spectroscopy. *Applied Physics Letters*, 68(18), Article#2541.
- Maruska, H. P., & Tietjen, J. J. (1969). The preparation and properties of vapor-deposited single-crystal-line GaN. *Applied Physics Letters*, 15(10), 327–329.
- Masi, M., & Kommu, S. (2001). Chapter 6 Epitaxial growth modeling. *Semiconductors and Semimetals*, 72(C), 185–224.
- Masui, H., Nakamura, S., DenBaars, S. P., & Mishra, U. K. (2010). Nonpolar and semipolar III-nitride light-emitting diodes: Achievements and challenges. *IEEE Transactions on Electron Devices*, 57(1), 88–100.
- McLaurin, M. B., Hirai, A., Young, E., Wu, F., & Speck, J. S. (2008). Basal plane stacking-fault related anisotropy in X-ray rocking curve widths of m-plane GaN. *Japanese Journal of Applied Physics*, 47(7 PART 1), 5429–5431.
- Meyaard, D. S., Lin, G. B., Cho, J., & Schubert, E. F. (2013). Efficiency droop in gallium indium nitride (GaInN)/gallium nitride (GaN) LEDs. *Nitride Semiconductor Light-Emitting Diodes (LEDs): Materials, Technologies and Applications* (pp. 279–300). Elsevier Ltd.
- Mion, C. (2006). *Investigation of the Thermal Properties of Gallium Nitride using the Three Omega Technique*. <https://repository.lib.ncsu.edu/handle/1840.16/5418>
- Moram, M. A., Johnston, C. F., Hollander, J. L., Kappers, M. J., & Humphreys, C. J. (2009). Understanding x-ray diffraction of nonpolar gallium nitride films. *Journal of Applied Physics*, 105(11), Article#113501.
- Nakamura, K., Makino, O., Tachibana, A., & Matsumoto, K. (2000). Quantum chemical study of parasitic reaction in III-V nitride semiconductor crystal growth. *Journal of Organometallic Chemistry*, 611(1–2), 514–524.
- Nakamura, S., Mukai, T., & Senoh, M. (1991). High-power gan p-n junction blue-light-

- emitting diodes. *Japanese Journal of Applied Physics*, 30(12A), L1998–L2001.
- Nakamura, S., Mukai, T., & Senoh, M. (1994). Candela-class high-brightness InGaN/AlGaIn double-heterostructure blue-light-emitting diodes. *Applied Physics Letters*, 64(13), 1687–1689.
- Nakamura, S., Mukai, T., Senoh, M., & Iwasa, N. (1992). Thermal annealing effects on P-type Mg-doped GaN films. *Japanese Journal of Applied Physics*, 31(2), 139–142.
- Nakamura, S., Pearton, S., & Fasol, G. (2000). Physics of gallium nitride and related compounds. *The Blue Laser Diode*, 29–45.
- Nakamura, S., Senoh, M., Nagahama, S. ichi, Iwasa, N., Yamada, T., Matsushita, T., Kiyoku, H., & Sugimoto, Y. (1996). InGaN-based multi-quantum-well-structure laser diodes. *Japanese Journal of Applied Physics, Part 2: Letters*, 35(1 B), Article#L74.
- Newman, N., & Vahidi, M. (2015). Kinetic processes in vapor phase epitaxy. *Handbook of Crystal Growth: Thin Films and Epitaxy: Second Edition* (Vol. 3, pp. 835–868). Elsevier Inc.
- Ni, X., Fu, Y., Moon, Y. T., Biyikli, N., & Morkoç, H. (2006). Optimization of (1120) a-plane GaN growth by MOCVD on (1102) r-plane sapphire. *Journal of Crystal Growth*, 290(1), 166–170.
- Ni, X., Özgür, Ü., Baski, A. A., Morkoç, H., Zhou, L., Smith, D. J., & Tran, C. A. (2007). Epitaxial lateral overgrowth of (112-2) semipolar GaN on (1100) m-plane sapphire by metalorganic chemical vapor deposition. *Applied Physics Letters*, 90(18), Article#182109.
- Northrup, J. E. (2009). GaN and InGaN (1122) surfaces: Group-III adlayers and indium incorporation. *Applied Physics Letters*, 95(13), Article#133107.
- Okamoto, K., Ohta, H., Nakagawa, D., Sonobe, M., Ichihara, J., & Takasu, H. (2006). Dislocation-free m-Plane InGaN/GaN light-emitting diodes on m-Plane GaN single crystals. *Japanese Journal of Applied Physics, Part 2: Letters*, 45(42–45), Article#L1197.
- Oliver, R. A., Kappers, M. J., Humphreys, C. J., & Briggs, G. A. D. (2005). Growth modes in heteroepitaxy of InGaN on GaN. *Journal of Applied Physics*, 97(1), Article#013707.
- Omar, A. Z., Shuhaimi Bin Abu Bakar, A., Makinudin, A. H. A., Khudus, M. I. M. A., Azman, A., Kamarundzaman, A., & Supangat, A. (2018). Effect of low NH₃ flux towards high quality semi-polar (11-22) GaN on m-plane sapphire via MOCVD. *Superlattices and Microstructures*, 117, 207–214.
- Ooi, C. S., Shuhaimi, A., Tan, G., Al-Zuhairi, O., & Majid, W. H. A. (2022). Effect of flux rate variation at fixed V/III ratio on semi-polar (1122) GaN: crystal quality and surface morphology study. *Crystals 2022, Vol. 12, Page 247, 12(2)*, 247.
- Oura, K., Katayama, M., Zotov, A. V., Lifshits, V. G., & Saranin, A. A. (2003). *Growth of Thin Films* (pp. 357–387). Springer, Berlin, Heidelberg.
- Pastrňák, J., & Součková, L. (1963). Herstellung dünner Schichten von Aluminium-, Gallium- sowie Indiumnitrid unter einer Gasentladung. *Physica Status Solidi (B)*, 3(2), K71–K74.
- Ploch, S., Frentrup, M., Wernicke, T., Pristovsek, M., Weyers, M., & Kneissl, M. (2010).

- Orientation control of GaN {1122} and {1013} grown on (1010) sapphire by metal-organic vapor phase epitaxy. *Journal of Crystal Growth*, 312(15), 2171–2174.
- Ploch, S., Wernicke, T., Dinh, D. V., Pristovsek, M., & Kneissl, M. (2012). Surface diffusion and layer morphology of (11 $\bar{2}$ 2) GaN grown by metal-organic vapor phase epitaxy. *Journal of Applied Physics*, 111(3), Article#033526.
- Posternak, M., Baldereschi, A., Catellani, A., & Resta, R. (1990). Ab initio study of the spontaneous polarization of pyroelectric BeO. *Physical Review Letters*, 64(15), 1777–1780.
- Romanov, A. E., Baker, T. J., Nakamura, S., & Speck, J. S. (2006). Strain-induced polarization in wurtzite III-nitride semipolar layers. *Journal of Applied Physics*, 100(2), Article#023522.
- Romanov, Alexey E., Young, E. C., Wu, F., Tyagi, A., Gallinat, C. S., Nakamura, S., Denbaars, S. P., & Speck, J. S. (2011). Basal plane misfit dislocations and stress relaxation in III-nitride semipolar heteroepitaxy. *Journal of Applied Physics*, 109(10), Article#103522.
- Rosenfeld, G., Comsa, G., & Poelsema, B. (1999). The concept of two mobilities for growth manipulation (pp. 349–366).
- Rosenfeld, G., Poelsema, B., & Comsa, G. (1995). The concept of two mobilities in homoepitaxial growth. *Journal of Crystal Growth*, 151(1–2), 230–233.
- Ruterana, P., Chauvat, M. P., Arroyo Rojas Dasilva, Y., Lei, H., Lahourcade, L., & Monroy, E. (2010). Extended defects in nitride layers, influence on the quantum wells and quantum dots. *Gallium Nitride Materials and Devices V*, 7602, Article#760212.
- Sato, H., Chung, R. B., Hirasawa, H., Fellows, N., Masui, H., Wu, F., Saito, M., Fujito, K., Speck, J. S., Denbaars, S. P., & Nakamura, S. (2008). Optical properties of yellow light-emitting diodes grown on semipolar (11 $\bar{2}$ 2) bulk GaN substrates. *Applied Physics Letters*, 92(22), Article#221110.
- Scheel, H. J. (2004). Control of epitaxial growth modes for high-performance devices. *Crystal Growth Technology* (pp. 621–644).
- Schwoebel, R. L., & Shipsey, E. J. (1966). Step motion on crystal surfaces. *Journal of Applied Physics*, 37(10), 3682–3686.
- Shen, Y. C., Mueller, G. O., Watanabe, S., Gardner, N. F., Munkholm, A., & Krames, M. R. (2007). Auger recombination in InGaN measured by photoluminescence. *Applied Physics Letters*, 91(14), Article#141101.
- Song, K. M., Kim, J. M., Kang, B. K., Yoon, D. H., Kang, S., Lee, S. W., & Lee, S. N. (2012). Characteristics of indium incorporation in InGaN/GaN multiple quantum wells grown on a-plane and c-plane GaN. *Applied Physics Letters*, 100(21), Article#212103.
- Song, K. R., Cho, C. Y., & Lee, S. N. (2020). Effect of a patterned sapphire substrate on indium localization in semipolar (11-22) GaN-based light-emitting diodes. *Thin Solid Films*, 707, Article#138077.
- Southern-Holland, R., Halsall, M., Wang, T., & Gong, Y. (2016). Power density dependent photoluminescence spectroscopy and Raman mapping of semi-polar and polar InGaN/GaN multiple quantum well samples. *Physica Status Solidi (C) Current*

- Speck, J. S., & Chichibu, S. F. (2009). Nonpolar and semipolar Group III nitride-based materials. *MRS Bulletin*, 34(5), 304–309.
- Stringfellow, G. B. (1974). Calculation of ternary and quaternary III–V phase diagrams. *Journal of Crystal Growth*, 27, 21–34.
- Strydom, J., Rooij, M. de, Reusch, D., & Lidow, A. (2015). *GaN Transistors for efficient power conversion* (2nd ed.). Wiley.
- Sun, C. J., Kung, P., Saxler, A., Ohsato, H., Haritos, K., & Razeghi, M. (1994). A crystallographic model of (00·1) aluminum nitride epitaxial thin film growth on (00·1) sapphire substrate. *Journal of Applied Physics*, 75(8), 3964–3967.
- Sun, Q., Leung, B., Yerino, C. D., Zhang, Y., & Han, J. (2009). Improving microstructural quality of semipolar (11 2-2) GaN on m-plane sapphire by a two-step growth process. *Applied Physics Letters*, 95(23), Article#231904.
- Sun, Q., Yerino, C. D., Ko, T. S., Cho, Y. S., Lee, I. H., Han, J., & Coltrin, M. E. (2008). Understanding nonpolar GaN growth through kinetic Wulff plots. *Journal of Applied Physics*, 104(9), Article#093523.
- Takeuchi, T., Amano, H., & Akasaki, I. (2000). Theoretical study of orientation dependence of piezoelectric effects in wurtzite strained GaInN/GaN heterostructures and quantum wells. *Japanese Journal of Applied Physics, Part 1: Regular Papers and Short Notes and Review Papers*, 39(2 A), 413–416.
- Tendille, F., De Mierry, P., Vennéguès, P., Chenot, S., & Teisseire, M. (2014). Defect reduction method in (11-22) semipolar GaN grown on patterned sapphire substrate by MOCVD: Toward heteroepitaxial semipolar GaN free of basal stacking faults. *Journal of Crystal Growth*, 404, 177–183.
- Thon, A., & Kuech, T. F. (1996). High temperature adduct formation of trimethylgallium and ammonia. *Applied Physics Letters*, 69(1), 55–57.
- Tyagi, A., Wu, F., Young, E. C., Chakraborty, A., Ohta, H., Bhat, R., Fujito, K., Denbaars, S. P., Nakamura, S., & Speck, J. S. (2009). Partial strain relaxation via misfit dislocation generation at heterointerfaces in (Al,In)GaN epitaxial layers grown on semipolar (11 $\bar{2}$ 2) GaN free standing substrates. *Applied Physics Letters*, 95(25), Article#251905.
- Van Der Merwe, J. H. (1963). Crystal interfaces. Part II. Finite overgrowths. *Journal of Applied Physics*, 34(1), 123–127.
- Vennéguès, P., Bougrioua, Z., & Guehne, T. (2007). Microstructural characterization of semipolar GaN templates and epitaxial-lateral-overgrown films deposited on m-plane sapphire by metalorganic vapor phase epitaxy. *Japanese Journal of Applied Physics, Part 1: Regular Papers and Short Notes and Review Papers*, 46(7 A), 4089–4095.
- Vurgaftman, I., & Meyer, J. R. (2003). Band parameters for nitrogen-containing semiconductors. In *Journal of Applied Physics* (Vol. 94, Issue 6, pp. 3675–3696).
- Vurgaftman, I., Meyer, J. R., & Ram-Mohan, L. R. (2001). Band parameters for III-V compound semiconductors and their alloys. *Journal of Applied Physics*, 89(11 I), 5815–5875.
- Waltereit, P., Brandt, O., Trampert, A., Grahn, H. T., Monniger, J., Ramsteiner, M.,

- Relche, M., & Ploog, K. H. (2000). Nitride semiconductors free of electrostatic fields for efficient white light-emitting diodes. *Nature*, 406(6798), 865–868.
- Wang, L., Zhao, G., Meng, Y., Li, H., Yang, S., & Wang, Z. (2018). Comparative Investigation of Semipolar (11-22) GaN Layers on m-Plane Sapphire with Different Nucleation Layers. *Journal of Nanoscience and Nanotechnology*, 18(11), 7446–7450.
- Wang, T. (2016). Topical Review: Development of overgrown semi-polar GaN for high efficiency green/yellow emission. In *Semiconductor Science and Technology* (Vol. 31, Issue 9, p. 093003). Institute of Physics Publishing.
- Wernicke, T., & Kneissl, M. (2014). III-Nitride semiconductors and their modern devices. In B. Gil (Ed.), *III-Nitride Semiconductors and their Modern Devices* (p. 253).
- Wernicke, T., Netzel, C., Weyers, M., & Kneissl, M. (2008). Semipolar GaN grown on m-plane sapphire using MOVPE. *Physica Status Solidi (C) Current Topics in Solid State Physics*, 5(6), 1815–1817.
- Wernicke, T., Ploch, S., Hoffmann, V., Knauer, A., Weyers, M., & Kneissl, M. (2011). Surface morphology of homoepitaxial GaN grown on non- and semipolar GaN substrates. *Physica Status Solidi (B) Basic Research*, 248(3), 574–577.
- Wernicke, T., Schade, L., Netzel, C., Rass, J., Hoffmann, V., Ploch, S., Knauer, A., Weyers, M., Schwarz, U., & Kneissl, M. (2012). Indium incorporation and emission wavelength of polar, nonpolar and semipolar InGaN quantum wells. *Semiconductor Science and Technology*, 27(2), Article# 024014.
- Wu, Z., Shen, X., Liu, C., Li, K., Shen, W., Kang, J., & Fang, Z. (2016). In situ asymmetric island sidewall growth of high-quality semipolar (11 $\bar{2}$ 2) GaN on m-plane sapphire. *CrystEngComm*, 18(29), 5440–5447.
- Xing, K., Tseng, C., Wang, L., Chi, P., Wang, J., Chen, P., & Liang, H. (2019). Semipolar (11-22) GaN epitaxial films with significantly reduced defect densities grown on m-plane sapphire using a sequence of two in situ SiN_x interlayers. *Applied Physics Letters*, 114(13), Article#131105.
- Xu, S. R., Zhang, J. C., Cao, Y. R., Zhou, X. W., Xue, J. S., Lin, Z. Y., Ma, J. C., Bao, F., & Hao, Y. (2012). Improvements in (11 $\bar{2}$ 2) semipolar GaN crystal quality by graded superlattices. *Thin Solid Films*, 520(6), 1909–1912.
- Young, E. C., Wu, F., Romanov, A. E., Tyagi, A., Gallinat, C. S., DenBaars, S. P., Nakamura, S., & Speck, J. S. (2010). Lattice tilt and misfit dislocations in (1122) semipolar GaN heteroepitaxy. *Applied Physics Express*, 3(1), Article# 011004.
- Zhang, Z., Kushimoto, M., Sakai, T., Sugiyama, N., Schowalter, L. J., Sasaoka, C., & Amano, H. (2019). A 271.8 nm deep-ultraviolet laser diode for room temperature operation. *Applied Physics Express*, 12(12), Article#124003.
- Zhao, G., Wang, L., Yang, S., Li, H., Wei, H., Han, D., & Wang, Z. (2016). Anisotropic structural and optical properties of semi-polar (11-22) GaN grown on m-plane sapphire using double AlN buffer layers. *Scientific Reports*, 6, Article# 20787.
- Zhao, Y., Yan, Q., Huang, C. Y., Huang, S. C., Shan Hsu, P., Tanaka, S., Pan, C. C., Kawaguchi, Y., Fujito, K., Van De Walle, C. G., Speck, J. S., Denbaars, S. P., Nakamura, S., & Feezell, D. (2012). Indium incorporation and emission properties of nonpolar and semipolar InGaN quantum wells. *Applied Physics Letters*, 100(20), Article#201108.

- Zhu, S., Lin, S., Li, J., Yu, Z., Cao, H., Yang, C., Li, J., & Zhao, L. (2017). Influence of quantum confined Stark effect and carrier localization effect on modulation bandwidth for GaN-based LEDs. *Applied Physics Letters*, *111*(17), Article# 171105.
- Zhu, T., Johnston, C. F., Kappers, M. J., & Oliver, R. A. (2010). Microstructural, optical, and electrical characterization of semipolar $(11\bar{2}2)$ gallium nitride grown by epitaxial lateral overgrowth. *Journal of Applied Physics*, *108*(8), Article# 083521.

Universiti Malaya